November 8, 2021

Finite element models to interpret and improve ECoG signals

Fun with FEMfuns

Meron Vermaas

meronvermaas@gmail.com

Radboud University Nijmegen

Donders Institute for Brain, Cognition and Behaviour

Supervisors:

prof. dr. Paul H.E. Tiesinga
prof. dr. Nick F. Ramsey

Co-supervisors:

dr. Maria Carla Piastra
dr. Thom F. Oostendorp

Doctoral Thesis Committee:

prof. dr. Richard J.A. van Wezel
prof. dr. Carsten H. Wolters
dr. Tjitske Heida

Contents

1 Introduction

The earliest recorded reference to the brain dates back to the 17th century B.C.E. [99]. The hieroglyph for brain can be found in the Edwin Smith papyrus with descriptions of patients with head injuries. Indeed, the origins of our thoughts have been of great interest to humans since ancient times, although our understanding has progressed slowly: for example, until the 4th century B.C.E. our intelligence was attributed to the heart [8]. At present age, neuronal networks in the brain and their dynamics are understood to underlie behavior and cognition [99]. Interest in linking cognition, behavior and the brain has particularly surged in the late 20th century, when neuroimaging techniques quickly developed. However, the actual emergence of human cognition as the result of the brain activity remains a major scientific and philosophical question[36, 2]. The activity in the brain can be inferred using a variety of methods, for example, by measuring metabolic changes which indirectly reflect the underlying neural activity [36]. To study the workings of the brain, other techniques are used to study the electrical signals produced in the brain.

Since bioelectric signals can be found in practically every organ in the body [137], it comes as no surprise that the brain has been studied extensively by recording the cortical electrical currents. As early as 1875, electric currents at the surface of the brain (electrocorticography, ECoG) have been recorded in rabbits [30]. A few decades later, electric potentials on top of the scalp (electroencephalography, EEG) were recorded in animals [156] and humans [14].

Here we will delve into common electrophysiological measures and the type of neuronal signals that they can pick up. Next, practical applications of these measures and necessary steps for improved recording performance will be discussed. Finally, a simulating approach to study electrophysiological recordings using mathematical models will be covered.

1.1 Recording neuronal activity

Excitable neural cells are called neurons. An activated neuron produces a transient and small electrical current which is called an action potential (or spike) and forms the basis of communication between neurons. The currents generate potential differences along the cell membrane that can

be recorded by electrodes. However, these potential differences fall off with the square of the distance to the source. Consequently, at distances within $\sim$ 200 μm the potentials of individual neurons are below noise level and cannot be discerned from the noise [28].

When recording from a larger distance (e.g., the surface of the brain or scalp), the electrical signals can only be measured when large groups of neurons are active synchronously [72, 141]. Therefore individual action potentials are not expected to be picked up in these types of measurements, because generally too few neurons fire in synchrony (the duration of the membrane potential depolarization and repolarization of an action potential is only $\sim$1-2 ms) [183]. Rather, postsynaptic activity is regarded as the main generator of extracellular potentials recorded at further distances [26], because of its longer time scale (10-20 ms), which makes synchronous activity more likely.

The electric current in neural tissue causes potential differences within the human head, which can be measured with electrodes [123, 139]. Electrophysiological recordings can coarsely be divided in three categories of detail: microscopic (recording from areas up to $\sim$ 200 μm), mesoscopic (up to several mm) and macroscopic (up to several cm), where each one samples from an increasingly larger number of neurons (Fig.1.1).

EEG and magnetoencephalography (MEG) measure at a macroscopic scale (i.e., the recorded signals has contributions from neuronal populations at distances up to several centimeters) [183].

At a mesoscopic scale, it is possible to record neuronal activity at a distance of several millimeters from the electrode (e.g., ECoG) [44]. However, no clear consensus has been established yet on the spatial reach of the recorded signals (i.e., the size of the region contributing to the recorded signal) [115, 13, 119, 42]; estimates range from 200 μm (cat) [101] to 5 mm (macaque) [98]. Comparing these different estimates is complicated since they depend on several factors, such as the animal species, brain region, electrode type, the stimulus that was used or the frequency band that is being considered [113].

There is minimal spatial averaging of the neuronal activity for microscopic electrophysiological experiments, where signals are picked up from areas similar in size compared to that of a neural cell body (i.e., 50 μm - 200 μm). Indeed, microelectrodes are perfectly suitable to accurately

record single unit activity (SUA, i.e., action potential waveforms of single neurons) or multi-unit activity (MUA, i.e., spikes of a local population of neurons). The biophysical basis underlying spiking dynamics has been uncovered especially thoroughly using microelectrodes and forms the basis of much of our understanding of neural dynamics (for an overview, see [104]).

The bandwidth of EEG (up to 70 Hz), ECoG (10 - 200 Hz) and microelectrode (up to 6 kHz) recordings [176] is mostly limited by the frequency dependent attenuation of the signal-to-noise ratio. For each type of recording, measuring bioelectric signals requires the conversion of ionic currents (the charge carriers in the body) into electric currents (electrons are the charge carriers in metals) [137]. The interaction between the metal electrode and the tissue that is being recorded from, results in changes in the ion concentrations near the electrode. A perfectly polarizable electrode alters the distribution of the ions (a displacement current flows), while no current flows into the electrode (no charge transfer occurs between the ion solution and the metal). Conversely, in a non-polarizable electrode, Faradaic current (charge transfer between the ion solution and the metal) passes into the electrode.

The biophysical mechanisms underlying the genesis of mesoscopic signals are difficult to interpret due to the complex configuration of the currents generated by neuronal processes in the highly inhomogeneous extracellular space [183]. The recorded signals are mainly the result of summated synaptic currents emerging during synchronized cortical excitation [130, 43, 183] at the scale of neuronal networks. Thus, in mesoscopic recordings, the activity of individual neurons can not be resolved as in microscopic recordings, but instead allows for assessing the coherence of local circuit activation, which has functional relevance for decoding [194, 19, 148]. Studying the neuronal circuit activity is of great value considering the highly interconnected structure of the brain [27, 51]. For example, cortical pyramidal cells are covered by approximately 10^4 to 10^5 synapses, with a typical balance between local interactions and long distance projections [177, 56].

ECoG is a useful and widely used methodology to monitor neuronal activity at a mesoscopic level with limited neuronal invasiveness (compared with intracortical recordings), making it especially suitable for clin-

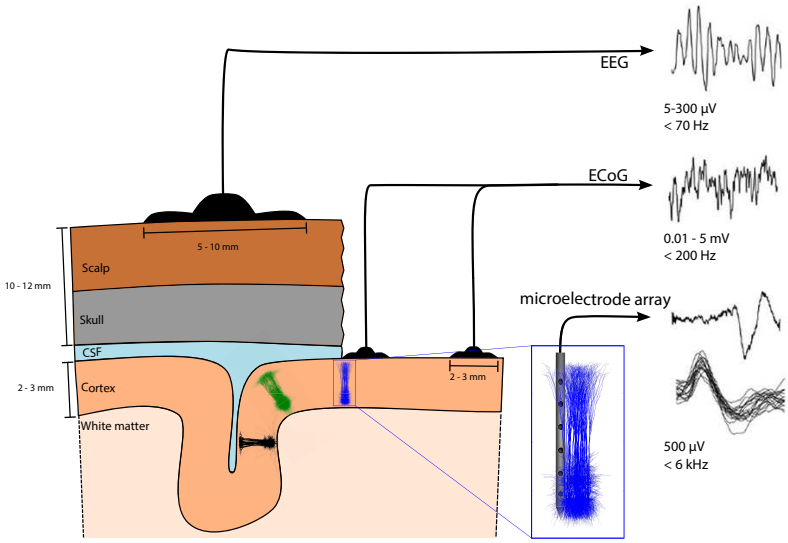

Fig. 1.1: Representation of recording electrodes at different spatial scales. At a macroscopic scale, EEG signals contain information from neuronal populations at several centimeters from the recording contact. The mesoscopic ECoG signals have contributions from neurons at several millimeters from the recording contact. Finally, the microelectrodes can record neuronal action potentials within $\sim$ 200 μm from the recording contact [25, 150]. Adapted from [70].

ical studies involving humans. The ECoG signal samples from a larger region than other mesoscopic recordings as it typically uses electrodes with a smaller impedance and a larger surface area [186]. Furthermore, the spatial resolution and signal quality (i.e., signal-to-noise ratio, SNR) of ECoG recordings is better than macroscopic EEG recordings [6]. Under experimental conditions, for instance, certain low frequencies fluctuate with location in ECoG recordings but seem to be uniform in EEG measurements [37]. Despite the advantages of ECoG, it is not as well studied as other electrophysiological measurements. For example, search results on EEG and microelectrodes in the past 4 years yield more than 20,000 publications, with only around 8,000 for ECoG. The main reason is given by

the invasiveness of ECoG when compared to EEG. ECoG is indeed used, for example, in the pre-surgical evaluation of drug-resistant focal epilepsy, but also, in brain computer interfaces as described in the next section.

1.2 Applications: BCIs and neuroprosthetics

Electrophysiological recordings can be utilized in neuroprosthetic technologies to realize direct communication between the nervous system and a device [1]. Additionally, information from the neuroprosthetic interface can be fed back to the user for closed-loop control. In this way, patients with physiological impairments (e.g., loss of motor function, hearing or vision) can control a neuroprosthesis which replaces, restores or improves [205] the natural nervous system output [1].

A large number of neuroprosthetic devices is used to apply electrical stimulation for the treatment of diseases such as Parkinson's disease, depression, epilepsy, cardiovascular disorders, auditory disorders [83, 85]. Another type of neuroprosthesis allows the user to control devices such as prosthetic limbs, wheel chairs or computer programs. This can restore movement, for example, by using the interface to exert control over a robot arm [32, 176]. Neuroprostheses that are controlled by activity in the central nervous system are also called brain-computer interfaces (BCIs).

BCIs are essential for people with severe paralysis, in particular for cases where a loss of voluntary muscular control is caused by neurodegenerative diseases or stroke. Recent developments in BCIs have shown great promise, where the device can be used in an unsupervised fashion at home to control a communication system by decoding motor intention [194, 148]. A schematic representation of this type of BCI paradigm is shown in figure 1.2.

In general, a BCI system requires recording of neural activity, real-time interpretation of the activity, controlling a device in order to perform the desired action and providing feedback to the user. Consistently and accurately recording neural activity for a BCI is an important challenge [206].

Specific and discrete mental processes (which characteristics are extracted out of the recorded signals) can be translated into commands for the device. For this purpose, a variety of event-related neuronal activity patterns have been examined, for example a discrete imagined hand grasp-

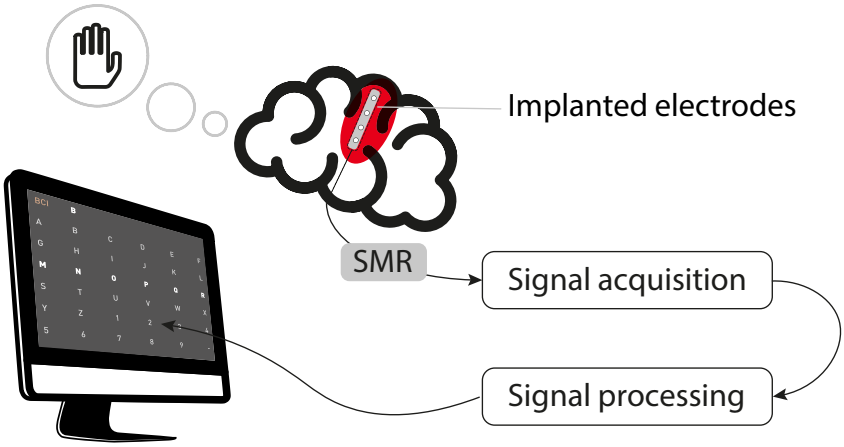

Fig. 1.2: A schematic representation of a BCI paradigm centered around an imagined hand movement. The electrode strip is placed over sensorimotor cortex to record a sensorimotor response (SMR) due to the imagined movement. Next, neural signal acquisition hardware, such as amplifiers and A/D converters, processes and digitizes the response. Real-time feature extraction is performed to decode if an imagined hand movement was made after which a letter is selected in a typing application. Adapted from [163].

ing movement [194]. Traditionally a single discrete signal was used, which limits the speed at which the BCI can be controlled. Indeed, an important challenge is to realize fast control over a device using a BCI. This could be accomplished by decoding multiple populations across brain areas to steer the BCI, for example by decoding hand gestures [19, 18]. Such an approach requires an electrode spacing that is optimized to distinguish between the activity patterns of interest.

Generally, for a successful BCI set-up, it is imperative to accurately discriminate the electrical activity of a region of interest from background activity of the surrounding neuronal tissue (as well as other types of noise). Choosing the desired recording electrode type is essential for long-term BCI systems.

Microelectrodes can be used to record neuronal spikes from individual neurons to control a BCI with high SNR [103, 73]. However, for long-term

usage of a BCI, recording from populations of neurons, rather than single neurons, provides more reliable electrical activity to control a BCI [125]. A small number of neurons is likely to be less stable over time due to, for example, neuroplasticity, since changes occur in the neuron morphology and network connectivity of the brain [52]. As a further complication, invasive microelectrodes have been correlated with neurodegeneration at the electrode contact due to localized hemorrhage and inflammation [155, 96].

An EEG-based BCI is controlled by recording from a large aggregate of neuronal population activity [67]. While EEG headsets can be used for BCIs at home [47], there are limitations to the spatial resolution that can be achieved, and thus the options for increasing the speed and versatility of the BCI is limited.

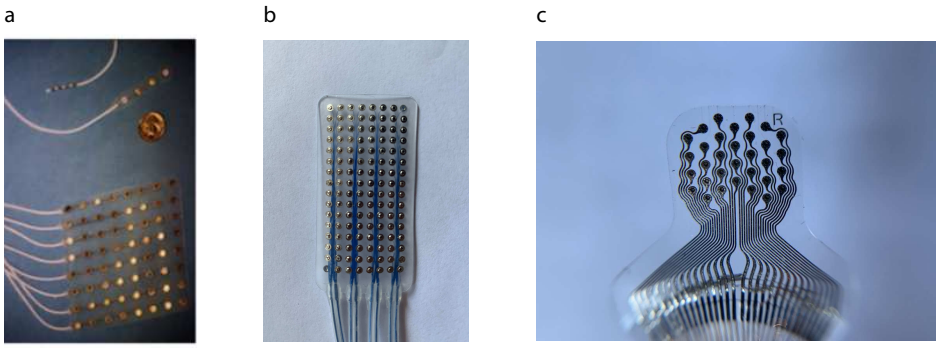

Fig. 1.3: Three examples of ECoG grids with decreasing spacing. a) A clinical Medtronic grid, b) a high density grid, and c) an (experimental) ultra high density grid by Cortec.

ECoG is a promising candidate for stable and long-term use of a BCI for at home usage, since it has a spatial resolution in between EEG and microelectrodes [194, 148]. ECoG was introduced only recently as a signal to control neuroprosthetic devices [114, 161]. These electrodes can be implanted for long-term use because the risk of damaging the cortical tis-

sue is limited (the cortical surface is usually not penetrated), resulting in durable and stable recordings [31]. Furthermore, the high signal fidelity renders ECoG well suited to decode motor- or sensory information used for efficient BCIs [19].

1.3 Improving recording electrode performance

Despite the successful use of electrodes in neural prostheses, therapies, diagnostics and surgical mapping, recent developments in electrode design allow for improvements in these applications [198, 84]. Typically, a trade-off needs to be made between many factors, such as electrode size, spacing, and noise. Rather than assuming there exists a "universally" optimal electrode for extracellular electrophysiological recordings, the electrode design needs to be adapted for specific activity patterns of interest, as well as the geometry and electrical characteristics of the region [198]. Generally, it is assumed that larger electrodes can only record synchronous activity of a large number of neurons (e.g., a typical EEG electrode diameter is 10 mm) [120], medium sized electrodes detect neuron population-level activity (e.g., ECoG electrode diameters ranging from 50 μm to 2 mm) [26], and small electrodes record the activity from a few nearby neurons (e.g., microelectrode diameters smaller than 20 μm) [166]. In addition, the distance to the neuronal source largely determines the optimal size of the electrode.

Biopotentials generated by neuronal activity in a particular area of the brain are distinguishable using their spatial and temporal characteristics. Spatial discrimination is influenced by parameters such as the electrode grid position, geometry, and material. Feature extraction using temporal characteristics involves various analysis methods of the recorded potentials (e.g., event-related potentials or power spectral density features) [109]. The algorithms used for feature extraction do not depend on the electrode design. Here, we will mainly focus on the effects of electrode grid properties (i.e., the electrode-tissue interface and electrode configurations) on the resulting recordings.

There is always a loss in the amplitude of a signal generated within a small source region as it passes through any conductive medium. Thus, in extracellular recordings the neuronal electrical signal of interest is inherently reduced with the distance between the neuron and the recording

site. Many components in the recording set-up influence the signal attenuation, for example the impedance of the electrode and (in the case of microelectrodes) the amplifier [135]. Additionally, practical factors centered around mechanical properties are of importance, for example the flexibility and transparency of the silicon sheet in which the electrodes are embedded. Here we will discuss three major challenges in achieving efficient performance of recording electrodes:

1. Discriminate the neuronal activity of interest from other neural signals;
2. Minimize the intrinsic and extrinsic electrical noise;
3. Minimize tissue damage due to placement of the electrode grid.

Source discrimination An approach to improve the discriminability of activity involves increasing the spatial resolution of electrode grids. This is an emerging trend [166, 209] which allows researchers to detect fine-grained details, such as interactions within neural networks. Recent improvements in the electrode design allow for more accurate signals with increased decodable features, resulting in improved diagnoses and mapping for surgery [182]. An intuitive approach to achieve a high spatial resolution is to increase the electrode density (ECoG grids with decreasing spacing are displayed in Fig. 1.3).

Alternatively, using electrodes with a large surface area increases the probability of recording close to neural activity of interest as well, since a larger brain area will be covered. Additionally, larger electrodes record from a larger population of neurons [202]. However, this has the downside of averaging along the electrode surface, which decreases the signal-to-noise ratio and some spatial detail of the neuronal activity will be lost [28, 169].

On the other hand, high density grids (i.e., the spatial resolution of the electrode grid) with small electrodes can be used to ensure a high probability that an electrode contact is physically close to the neural activity without spatial averaging [198]. However, it is not easy to increase the number of electrodes, since, for example, it requires the development of small electrodes, readout circuitry and wiring [181], which may in turn negatively affect the noise level and quality of the signal classification [16].

Considering that large electrodes reflect the aggregate activity of many neurons and small electrodes only record the signal of nearby neurons, an

optimal trade-off of the electrode size can be found [28]. Due to the larger area that large electrodes sample from, the SNR of the region of interest can either decrease (since more neuronal background activity is picked up), or increase (since neuronal noise gets averaged out) [76]. For example, to accomplish spike sorting in the hippocampus an electrode diameter of 40 μm was estimated to be optimal (in a range between 10 μm and 200 μm). This means that decreasing electrode size does not necessarily improve the recording quality) [28].

An easy way to map the sensitivity of electrodes to source activity at different locations in the brain is to use the Helmholz theorem of reciprocity [86, 79, 152]. The reciprocity theorem states that the potential difference V_{AB} between two surface electrodes A and B that is generated by a monopole current source of strength I_0 at location $\vec{r}$ (Fig. 1.4A), is equal to the potential at location $\vec{r}$ generated by current I_0 passing between electrodes A and B (Fig. 1.4B). This holds for electrodes of any size. We define the *lead field* of electrode pair AB, $L_{AB,mono}(\vec{r})$, as the potential distribution throughout the volume generated by passing a unit current between electrodes A and B. The reciprocity theorem implies that the potential difference generated between A and B by any monopole of strength m at location $\vec{r}$ is equal to $L_{AB,mono}(\vec{r}) \cdot m$. Consequently, $L_{AB,mono}(\vec{r})$ can be interpreted as the sensitivity of electrode pair AB to a monopole source at location $\vec{r}$: the smaller the lead field at location $\vec{r}$, the smaller the recorded potential for a source at that location. Notice that passing a current between two electrodes defines the potentials within the volume up unto a constant; the reciprocity theorem only holds when the lead field is computed if the potentials at the electrodes are set equal but opposite in sign ($\pm\frac{1}{2}V_{AB}$).

The lead field interpretation can easily be extended to the more useful case of dipole sources (if only because single current monopoles within a bounded volume conductor cannot exist). We define the dipole lead field as $\vec{L}_{AB,dip}(\vec{r}) = \nabla L_{AB,mono}(\vec{r})$. Then the potential difference between electrodes A and B resulting from a dipole of moment $\vec{d}$ at location $\vec{r}$ is equal to $\vec{L}_{AB,dip}(\vec{r}) \cdot \vec{d}$. Before it became possible to calculate lead fields by means of computer models in complex geometries where no analytical solution is available, lead fields were actually measured in phantoms by reciprocally energizing electrodes fixed to a tank model [123].

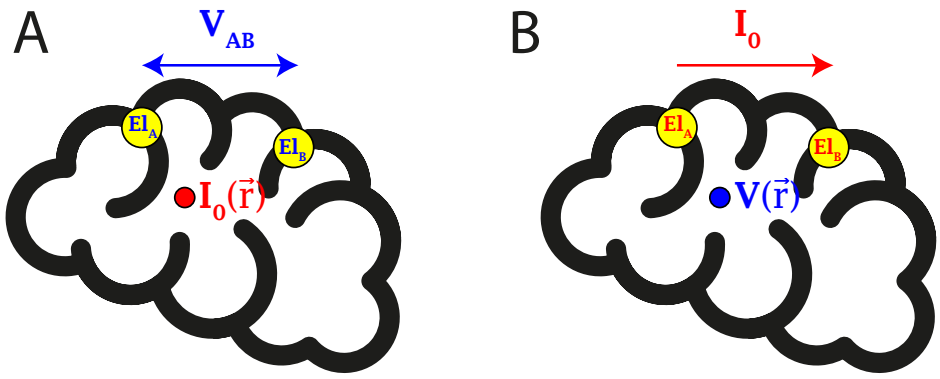

Fig. 1.4: Schematic representation of the reciprocity theorem. A) The potential difference V_{AB} between two surface electrodes El_A and El_B that is generated by a monopole current source of strength I_0 at location $\vec{r}$ is shown. This is equivalent to B), where the potential at location $\vec{r}$ is generated by passing current I_0 between electrodes El_A and El_B.

The reciprocity theorem implies that for a point electrode the sensitivity to a dipole source decreases with the square of the distance between electrode and source, which is completely consistent with the well known potential distribution generated by a dipole source. Actual electrodes are not points. If the electrode size is small compared to the distance toward to source, it can reasonably be approximated as a point electrode. Close to the electrode, however, the potential generated by the electrode as one of a pair of current injecting electrodes drops linearly with the distance, and consequently the lead field for dipoles as well. This demonstrates that the electrode size cannot be ignored when sources are so close to the electrodes that the electrode size is not much larger than the distance to the source. We will show in this thesis that a good rule of thumb is that electrode size must be taken into account when the distance to the source is equal to or smaller than the electrode size.

Noise The characteristics of the electrode affect the level and type of noise that is expected, as well as the SNR. Intrinsic noise is generated in the signal for each recording electrode by the circuit itself. The most common type of intrinsic noise is thermal noise, which emerges in a con-

ducting material by random thermal motion [154]. According to Johnson [94] the noise is proportional to the impedance, whereas the impedance is inversely proportional to the surface area. Indeed, the size of the electrode determines the contribution of thermal noise to the recorded signal [165]. Thus, as electrodes become smaller, the intrinsic thermal noise increases. Another characteristic with a large influence on the electrode impedance is the electrode-electrolyte interface [165]. This interface consists of an electrical double layer with a layer of electrons, a layer of adsorbed ions, and a diffuse double layer [61].

Much modeling research has focused on characterizing and improving the performance of electrodes by the careful selection of the materials and surface chemistry [90, 78, 102]. With a decreasing electrode size, the electrode impedance increases. This results in signal attenuation due to the voltage divider circuit, which is a common passive attenuator that distributes the input voltage over the impedances of the divider. It typically consists of the electrode impedance, the routing capacitances and the amplifier impedance [135]. Therefore, amplifiers with a high input impedance are necessary for small electrodes (diameters < 10 μm). As electrodes become smaller it becomes increasingly difficult to provide an amplifier impedance that is high enough, since a ratio between the impedance of the electrode, Z_e, and the amplifier, Z_a, of less than 0.1 ($Z_e/Z_a < 0.1$) is required for sufficient SNR [135, 198].

Carefully choosing the amplifier configuration can help to achieve sufficient gain. For example, a closed-loop amplifier achieves a low effective input impedance of the recording configuration by using a large input capacitance and a small feedback capacitance [77, 197]. Alternatively, an open-loop amplifier could be used (which depends on a low input transistor gate capacitance [197]).

Extrinsic noise gets introduced by external sources, a common example is 60 Hz line noise. Generally, extrinsic noise is decreased by using a referential, bipolar or multipolar configuration and subtracting one channel from the other. Each configuration has its own requirements, for example, a bipolar pair needs to be sufficiently close to ensure that the same noise is recorded on both contacts, but far enough such that the neural activity of interest is not recorded at both channels (and subsequently removed as well) [86].

Tissue damage Damage to the tissue or the electrode (e.g., due to corrosion) is generally a concern in stimulating electrode neuroprosthetics. Due to the high potentials, toxic electrochemical reactions and tissue hyperexcitability (both leading to damage) may occur [127].

While the implantation of recording ECoG electrodes is not prone to these issues, there is a risk of infection [147], since a craniotomy needs to be performed. Furthermore, generally the grid is large and relatively stiff (e.g., metal contacts do not bend along the brain surface), which may result in mechanical damage [203]. Biocompatible grid material, improved implantation procedures or smaller grids could circumvent these issues [159].

1.4 Simulating recording electrodes

Despite the prevalence of extracellular recordings in neuroscience, our understanding of the manufacturing of electrodes and interpretation of the potentials they record can still be improved upon. A modeling approach is an effective way to investigate and develop electrode designs, especially considering current advances in high-density electrode grids [165, 134, 41, 169, 86]. Using various models, researchers can predict the volume of activated tissue during stimulation [23], quantify the effect of tissue and electrode types [29, 97, 65, 157, 196], and estimate the optimal electrode spacing [181, 28].

Two of the approaches that can be used for mathematical models of electrophysiological recordings are: models of the dynamical activity of neurons phenomenologically translated into local field potentials (e.g., NEURON [82], The Virtual Brain [112] or NEST [46]) and volume conductor models with source distributions [141, 71]. Volume conduction will be the focus in this thesis.

Volume conduction modeling

Volume conduction can be described as the spread of electrical fields from a current source (e.g., neuronal activity) through a volume (e.g., biological tissue) to the location of a sensor (e.g., electrodes) [168]. This means that the sensor is separated from the electric source by a medium. In neuroscience, volume conduction theory can help with addressing practical

problems encountered when recording and interpreting electrophysiological signals. It gives a detailed description of the transmission of currents and potentials through the brain, skull, scalp, and electrodes.

While the fundamental laws governing a volume conductor (centered around charge conservation and Ohm's law) are well established, applying them to electrophysiology is not trivial because of the large differences in conductivities of the different tissues in the head [141, 71]. Volume conduction models also provide a basis for source localization algorithms, which involves solving the so-called forward and inverse problem.

In the forward problem the potentials in the volume due to sources with a known location, orientation and magnitude are calculated. The inverse problem uses a set of repeated solutions (i.e., the lead field matrix) of the forward problem to estimate the current sources underlying an electrophysiological recording. Constrained with a no-flux boundary condition (no current flows out of the head into the air) and some additional constraint, for example, fixing one electrode to zero potential, the forward problem has a unique solution. On the other hand, the inverse problem is ill-posed and requires additional assumptions to find a unique solution.

While forward solutions can be found analytically for simple geometries, a numerical approach is needed for more complex geometries, with compartments with different tissue types (with different conductivities) and more extensive boundary conditions [29, 97, 65, 157, 196]. The forward problem consists of a Poisson equation. It relates an applied (neuronal) current source to the distribution of currents and potentials in the brain. The Poisson equation is derived using Maxwell's equations and has been described extensively in literature [123, 69, 141, 92].

In the forward problem, developing a realistic model of the head can be challenging: it requires a combination of experimental and theoretical methods. The head is inhomogeneous and to ensure an accurate forward model, creating an accurate segmentation and finding the correct conductivities of each material is essential. Although there are conductivity values that are commonly used [153, 141, 145], choosing an accurate value is not straightforward since there is no consensus in the literature [124, 23, 128, 118, 211] as well as significant inter-subject variability [126, 5].

Another factor that influences how currents spread (non-uniformly) within the volume conductor is tissue anisotropy. This means that the conductivity is direction dependent, which is represented by a non-isotropic conductivity tensor, and can, for example, be observed in the white matter (directions parallel vs orthogonal to the axon) [68], across the lamina in the cortex (layer-dependent orientations of axons) [63] and in the skull [124].

When simulating bio-electricity with volume conductor models at a macroscopic scale, generally only resistive (Ohmic) currents are considered. Thus the volume conduction is considered linear [153, 141] and instantaneous, despite the inhomogeneous and anisotropic tissue. This is consistent with the so-called quasi-static approximation of Maxwell's equations. It means that phase shifts due to capacitive and inductive tissue properties are negligible for the considered volume of tissue at a low frequency range (<1kHz). More concretely, at a macroscopic scale, no charge "builds up" in the medium and the electric potentials generated by a source can be considered without any time delay (i.e., as if stationary).

Whether, and at what spatial scale, the extracellular medium can be regarded as purely ohmic remains a topic of discussion [60, 10, 128, 118]. Especially at the scale of individual cells, recording close to the membrane, describing capacitive currents cannot be omitted [66].

While capacitive effects are generally small at a macroscopic scale, they can be more noticeable at the electrode-electrolyte interface. In fact, the contact impedance, shape and size of the electrode can substantially affect the forward solution [157, 29]. There are Faradaic and non-Faradaic currents at the contact surface between the tissue and the electrode. Several studies have addressed the effect of the presence of electrodes on the forward solution [97, 24, 29, 65, 22, 196]. The overall conclusion of these studies is that it is, for some stimulating electrodes and microelectrodes set-ups, necessary to include electrode effects (both capacitive and resistive) in volume conductor models.

Besides the tissue and electrode in the volume conduction model, an approximation of the underlying sources, their location and orientation must be chosen. The most common approach is to apply a source at a mesoscale, such as a cortical dipole or dipole layer [141]. More realistic sources and activity patterns can be generated by, for example, us-

ing multi-compartment models of the laminar structure of the neocortex for MEG [178] or microelectrode [136] recordings. In our models, dipole sources were applied and approximated by two monopoles (i.e., a bipole, Fig.1.5).

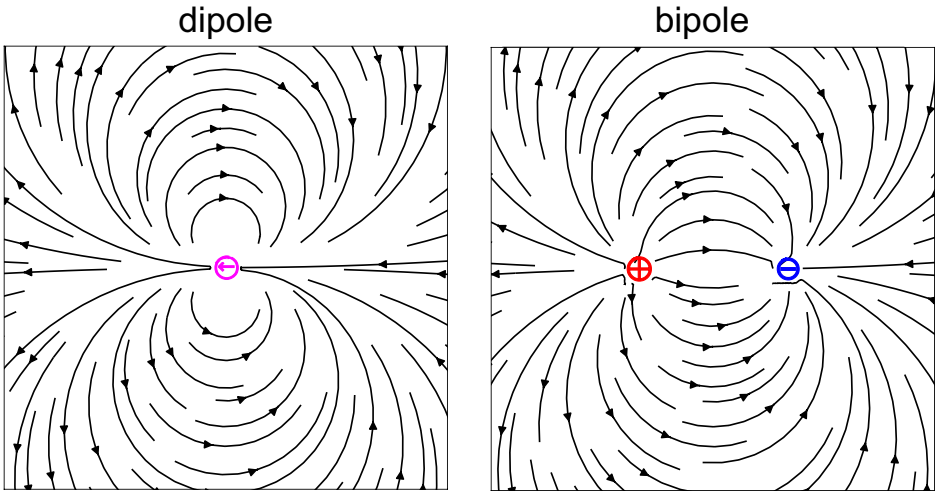

Fig. 1.5: The electric field due to a point dipole (left), a physical dipole approximated by two electric charges (right).

Despite the assumptions that need to be made regarding the volume conductor model, forward computations are a valuable tool to make quantitative estimations of the relation between sources, electric parameters of the tissue and recording equipment [141].

FEM There are many numerical approaches that can be used to solve the forward problem, such as the boundary element method, the finite difference method, the finite element method (FEM), or the finite volume method [106]. The FEM was used in this thesis and here a short description of the general concepts will be given. For more details, see, for example, [107].

The FEM creates computational schemes for solving any partial differential equation (PDE) on any domain [106]. It is particularly suitable

for complex, anisotropic geometries and irregular shapes consisting of different types of materials. These geometries typically are not easy to deal with in other numerical approaches. Furthermore, a variety of boundary conditions can easily be implemented. The name "finite element method" stems from the process called discretization, where a domain is divided into a finite number of regularly shaped elements (i.e., finite elements). A triangulated domain (i.e., when using triangles, 2D, or tetrahedra, 3D, as the element) is a mesh containing cells that are connected in terms of their vertices. Creating a mesh representing the domain of interest is a necessary first step for a numerical implementation.

The underlying idea of FEM is to calculate a "stencil" on a general element and use it on each element in the mesh [106]. This is where the strength of the FEM comes out and it requires two steps: 1) on each element the solution is represented by a polynomial expression; 2) integration over each individual element as part of a variational formulation of the PDE, resulting in a stencil of the PDE. In Step 1, an approximation of the solution is represented by a linear combination of basis functions. The variational formulation in step 2 is found by multiplying the PDE by a so-called test function (which is also a linear combination of basis functions). Next the terms in the equation are rewritten to only contain first derivatives (the so-called "weak" form), such that the polynomial space of the solution, the so-called trial function, only needs to be differentiable once.

Finally, the element equations can be assembled into a global equation in matrix form, which is solved at the nodes (when using Lagrangian FEM) of the mesh. The resulting linear system of equations typically is solved using Gaussian elimination. However, such a sparse LU (lower-upper) decomposition can become memory demanding and slow (especially in some of the cases in this thesis), in which case an iterative solver is necessary (e.g., Krylov solvers). There are several packages (e.g. FEniCS [3]) that provide a pipeline for assembling as well as offering different solver options, which makes it possible for the user to focus on the physical formulation of the problem at hand.

1.5 Thesis outline

Brain recordings with high signal fidelity are essential for diagnosis, building neuroprosthesis and other fundamental scientific experiments. ECoG has proven to be well suited to realize recordings that have both excellent signal quality and long-term stability. While EEG and microelectrodes have been extensively studied [141, 26] and are (relatively) well understood, the interpretation and improvement of ECoG electrodes has a lot of potential to be developed further. In this thesis, we focused on how to better understand and improve ECoG recordings in terms of electrode properties and their spatial configuration.

In Chapter 2, we develop an open-source, easy-to-use and flexible volume conduction modeling pipeline named FEMfuns. Since volume conduction has not been used abundantly to study ECoG measurements, a versatile tool needed to be created to investigate what degree of detail ECoG simulations require to be useful and accurate. The pipeline allows for the simulation of multiple material compartments in volume conductor models with as many compartments as needed (e.g., an arbitrary amount of realistically shaped electrode can be used). Resistive, capacitive and dispersive tissue properties can be used and different types of electrode models are implemented. Furthermore, the `Python` code can be easily adjusted and extended to meet user needs.

Next, in Chapter 3 we use the FEMfuns pipeline to study how much detail should be included in ECoG volume conduction models. In particular, the importance of explicitly including electrode properties in volume conduction models for accurately interpreting ECoG measurements is shown. As a simple rule of thumb, we recommend that when the distance between an electrode and the source is equal to or smaller than the size of the electrode, electrode effects cannot be disregarded.

In Chapter 4 we study how sensitive ECoG electrodes in a particular configuration are to the relative position of the underlying sources. Somatotopic activity of the fingers was simulated in the sensorimotor cortex and we investigated whether movements of individual fingers can be separated from each other when recording with a high-density ECoG grid. More generally, we provide an approach to estimate whether a particular activity pattern is distinguishable with the electrode grid that is being used.

Finally, a discussion with limitations, possible improvements and future research is described.

2 FEMfuns: a volume conduction modeling pipeline that includes resistive, capacitive or dispersive tissue and electrodes

M Vermaas, MC Piastra, TF Oostendorp, NF Ramsey, and PHE Tiesinga.
This Chapter consists of a paper that has been published in Neuroinformatics (2020).
https://doi.org/10.1007/s12021-020-09458-8

Abstract

Applications such as brain computer interfaces require recordings of relevant neuronal population activity with high precision, for example, with electrocorticography (ECoG) grids. In order to achieve this, both the placement of the electrode grid on the cortex and the electrode properties, such as the electrode size and material, need to be optimized. For this purpose, it is essential to have a reliable tool that is able to simulate the extracellular potential, i.e., to solve the so-called ECoG forward problem, and to incorporate the properties of the electrodes explicitly in the model.

In this study, this need is addressed by introducing the first open-source pipeline, FEMfuns (finite element method for useful neuroscience simulations), that allows neuroscientists to solve the forward problem in a variety of different geometrical domains, including different types of source models and electrode properties, such as resistive and capacitive materials. FEMfuns is based on the finite element method (FEM) implemented in FEniCS and includes the geometry tessellation, several electrode-electrolyte implementations and adaptive refinement options. The `Python` code of the pipeline is available under the GNU General Public License version 3 at https://github.com/meronvermaas/FEMfuns.

We tested our pipeline with several geometries and source configurations such as a dipolar source in a multi-layer sphere model and a five-compartment realistically-shaped head model. Furthermore, we describe the main scripts in the pipeline, illustrating its flexible and versatile use. Provided with a sufficiently fine tessellation, the numerical solution of the forward problem approximates the analytical solution. Furthermore, we show dispersive material and interface effects in line with previous literature. Our results indicate substantial capacitive and dispersive effects due to the electrode-electrolyte interface when using stimulating electrodes.

The results demonstrate that the pipeline presented in this paper is an accurate and flexible tool to simulate signals generated on electrode grids by the spatiotemporal electrical activity patterns produced by sources and thereby allows the user to optimize grids for brain computer interfaces including exploration of alternative electrode materials/properties.

Keywords: Computational modeling, Finite element method, Electrical double layer, Dispersive tissue, Complete electrode model

2.1 Introduction

Stimulating and recording the brain by means of electrodes provides a versatile method to deepen our understanding of neural networks and their role in cognitive processes. Reconstructing the spatio-temporal distribution of neural current sources underlying electrophysiological data, such as electroencephalography (EEG) and electrocorticography (ECoG), assists in studying neural processes. Estimating the sources corresponds to solving the forward- and inverse problem.

The forward problem assumes a known source and solves for the electric potential in the brain. The inverse problem consists of estimating the source configuration underlying the recorded potential. The inverse problem requires solving the forward problem first and consequently the accuracy of the estimated sources will depend on the accuracy of the solution of the forward problem.

The Finite Element Method (FEM) is a suitable numerical method to solve the forward problem; it can incorporate the complex geometry of the head and allows for anisotropic conductivities, for example, to account for the laminar structure of cortex [63]. FEM has been used to quantify various volume conduction effects, such as the influence of skull anisotropy [124], tissue inhomogeneities and anisotropies [23], and dispersive tissue properties [65].

A realistic description of the geometry and correct values of the electrical parameters of the biological tissues are essential to ensure an accurate forward model. The electrical conductivity and relative permittivity of biological tissues vary with frequency (i.e., they are dispersive, [55, 128]). However, volume conductor models used in bio-electricity generally consider only resistive currents, which is consistent with the so-called quasi-static approximation of Maxwell's equations [153, 141], and capacitive, inductive and propagation effects are assumed to be negligible [128]. Whether the extracellular medium can be regarded as purely ohmic remains a topic of discussion [60, 10, 128, 118].

A limited number of studies have addressed the effect of the presence of electrodes on the forward solution [97, 24, 29, 65]. The electric properties of

electrodes are typically non-linear because of the properties of the current density distribution along its surface [137]. In particular, when an electrode is immersed in an electrolyte, the charge carrier between the two materials changes from electronic in the metal to ionic in the electrolyte. As a result an electrical double layer forms on the external surface of the electrode where, in recording electrodes, a mix of faradaic (ohmic) and non-faradaic (capacitive) currents occurs depending on the magnitude of the potential difference across the interface [164].

These ohmic and capacitive currents across the electrode have been implemented in FEM studies in a variety of set-ups, e.g., imposing faradaic currents [97], non-faradaic currents [24] or a parallel combination of the two [29, 65]. Models of recording electrodes, such as EEG, generally assume a simple point electrode model, while only a handful studies considers EEG forward models including the effect of electrode size and shunting [143, 158].

In this study, we describe the workflow and capabilities of a volume conduction modeling pipeline FEMfuns (FEM for useful neuroscience simulations). The goal of this pipeline is to provide a `Python`-based framework centered around a general FEM toolbox, i.e., FEniCS [3, 117], to make forward models available, easily exploitable and adjustable for the neuroscience community. The volume conductor in FEMfuns can be described by resistive, capacitive and dispersive material properties. Furthermore, electrode interface effects can be flexibly added and the accuracy of the forward solution is described.

2.2 Methods

In this work we conducted three different studies with the goal of demonstrating the capabilities of our FEMfuns pipeline. In all the studies Lagrangian FEM [200] was applied to simulate the electric potential generated in a volume conductor by a known source. Both an internal dipolar source and an externally induced stimulating electrode are implemented. This can be useful considering the fact that the sensitivity of detecting bioelectric signals and the distribution in electrical stimulation are interchangeable [123], due to the reciprocity theorem [79, 167, 87].

Forward model

The electric potential φ generated in the brain can be computed through the quasistatic approximation of Maxwell's equations [153]. In our work, we considered two representations of the volume conductor, namely a purely resistive model and one that includes capacitive tissue properties. In the resistive version with primary current density $\mathbf{J}_p$ (current produced by neuronal activity, e.g. a dipole, or from stimulating electrodes), ohmic currents are described in medium Ω with conductivity σ through the following equation:

$$-\nabla \cdot (\sigma \nabla \varphi) = \nabla \cdot \mathbf{J}_p, \quad \text{in } \Omega. \tag{2.1}$$

When taking into account the capacitive tissue properties, the quasistatic approximation of Maxwell's equations does not hold anymore and the following frequency-dependent Poisson equation [153] has to be considered instead:

$$-\nabla \cdot ([\sigma(\omega) + j\omega\varepsilon_0\varepsilon_r(\omega)]\nabla\varphi) = \nabla \cdot \mathbf{J}_p, \quad \text{in } \Omega, \tag{2.2}$$

where j is the imaginary unit, $\omega = 2\pi f$ is the angular frequency of the source, ε_0 is the permittivity in vacuum ($8.85 \times 10^{-12} F/m$) and ε_r is the relative permittivity. In case of a stimulating pulse or periodic currents generated by synchronous oscillations of neuronal circuits, a fast Fourier transform (FFT) is performed on the time series of the source. Then, the FEM is solved for each frequency separately and the signal in the tissue is reconstituted using the inverse FFT. This FEM-Fourier approach is comparable to several previous FEM studies [24, 65, 188]. It is essential to ensure the correct relationship between the real and imaginary part of an immittance, which is given by the Kramers-Kronig transforms [191, 9, 128, 11]. Both the medium [191, 55] and the electrode interface impedance [192, 121, 164] values we use satisfy the Kramers-Kronig relationship.

In both the resistive (2.1) and capacitive (2.2) scenario, a homogeneous Neumann boundary condition (BC) is applied on the exterior boundary $\partial\Omega$,

$$\sigma \nabla \varphi \cdot \boldsymbol{n} = 0, \text{ on } \partial\Omega, \tag{2.3}$$

where $\boldsymbol{n}$ is the unit outer normal vector on $\partial\Omega$.

The finite element method for solving the forward problem

Lagrangian FEM was used to solve the Poisson equation (2.1) [116, 107, 106]. The first step consists of deriving the so-called weak formulation of the elliptic partial differential equation (2.1) [106]:

$$a(u, v) = L(v), \forall u, v \text{ in } V \in H^1(\Omega), \tag{2.4}$$

$$\text{where } a(u, v) = \int_\Omega \sigma \nabla u \cdot \nabla v \, \mathrm{d}x \tag{2.5}$$

$$\text{and } L(v) = \int_\Omega f v \, \mathrm{d}x, \tag{2.6}$$

where H^1 is the first-order Sobolev space. The weak form can be heuristically derived by multiplication with a test function $v \in V$ and subsequent partial integration. Reorganization of some terms and applying the homogeneous Neumann BC leads to (2.5) and (2.6).

In the second step, equation (2.4) is discretized yielding the following linear system:

$$Au = b, \tag{2.7}$$

with $A_{ij} = \int_\Omega \sigma \nabla \varphi_i \cdot \nabla \varphi_j \, \mathrm{d}x$ and $b_i = \int_\Omega f \varphi_i \, \mathrm{d}x$, and $\{\varphi_i\}_i$ a set of basis functions.

Next, the linear system (2.7) is solved and the finite dimensional solution $u = \sum_j u_j \varphi_j$ is found.

In order to solve (2.2) with FEM, we had to deal with complex numbers (i.e., admittivity y), whose direct use was not yet implemented in FEniCS. In particular, we assembled complex numbers in a representation using real-valued coupled-PDEs. Starting from the strong formulation in the complex function space, i.e.,

$$-\nabla \cdot ((y_r + j y_j) \nabla (\varphi_r + j \varphi_j)) = f_r + j f_j \quad \text{in } \Omega, \tag{2.8}$$

we split trial functions, test functions and the admittivity tensor into a real and imaginary part, $u = u_r + j u_j$, $v = v_r + j v_j$ and $y = y_r + j y_j$, respectively, therefore considering the mixed space $W = V \times V$. This

results in a matrix doubled in linear size, composed of four blocks of the matrix created for the real version.

The weak form can again be derived by multiplying with the test function followed by partial integration, which for the left hand side gives a real part:

$$a_r(u,v) = \int_\Omega (y_r \nabla v_r \cdot \nabla u_r) - (y_r \nabla v_j \cdot \nabla u_j) - (y_j \nabla v_r \cdot \nabla u_j) - (y_j \nabla v_j \cdot \nabla u_r)\ \mathrm{d}x$$

and an imaginary part:

$$a_j(u,v) = \int_\Omega (-y_i \nabla v_j \cdot \nabla u_j) + (y_r \nabla v_j \cdot \nabla u_r) + (y_j \nabla v_r \cdot \nabla u_r) + (y_r \nabla v_r \cdot \nabla u_j)\ \mathrm{d}x$$

Without an imaginary source, the right hand side weak form contains real part $L_r(v) = \int_\Omega f_r v_r\ \mathrm{d}x$ and imaginary part $L_j(v) = \int_\Omega f_r v_j\ \mathrm{d}x$.

Electrode-electrolyte interface There are several ways to approximate the impedance that results from the electrode-electrolyte interface [29, 97]. When recording or stimulating with an electrode, ideally no electrochemical reactions occur and hence all currents are capacitive. This regime can be modeled with a capacitance and an infinite transfer resistance at the (non-faradaic) interface of a stimulating or recording electrode. [164] empirically find that a standard capacitor does not describe the non-faradaic impedance accurately. This requires a pseudocapacitive constant phase angle impedance Z_{CPA}:

$$Z_{CPA} = K(j\omega)^{-\beta}, \tag{2.9}$$

where $K = 1.57\ \Omega m^2 s^{-\beta}$ and $\beta = 0.91$ are physical constants [29, 164].

[97] estimated the electrode-electrolyte interface impedance by fitting their FEM solutions to experimental data. In their model, the interface currents are described with faradaic reactions using a thin-layer approximation with a real valued surface admittance y_k (S/m^2) expressed by the so-called Robin BC applied at the k-th electrode:

$$-\sigma \frac{\partial \varphi}{\partial \mathrm{n}} = y_k(\varphi - \varphi_{\mathrm{metal}_k}),\ \text{on}\ \Gamma_{\mathrm{R}}^k, \quad k = 0, 1, \ldots \tag{2.10}$$

where φ_{metal_k} is the electrical potential of the k-th electrode, Γ_{R}^k is its boundary.

[29] and [65] considered a constant phase angle impedance (2.9) and a charge transfer resistance set up in parallel. The double layer [80] is assumed to be 1 nm thick and the overpotential-independent charge transfer resistance can be described with the gas constant R, temperature T, number of electrons per molecule n, Faraday's constant F and the exchange current I_0. The appropriate values for these parameters are discussed in detail in [29]. The charge transfer resistance R_{CT} (Ohm) is defined in terms of these variables:

$$R_{CT} = \frac{RT}{nFI_0}. \tag{2.11}$$

In our approach, we used Robin boundary conditions (2.10) to describe the interface, with its surface admittance y_k described by the pseudocapacitance (2.9) and charge transfer resistance (2.11) set up in parallel. Depending on the chosen y_k, the interface processes can be described as faradaic, non-faradaic or a combination of the two.

In the case of recording electrodes, equation (2.10) needs to be used self-consistently, since for each electrode the value of φ_{metal} is unknown. We use the Lagrange multiplier method [75, 74, 4] to impose φ_{metal} as the surface integral over the electrode in Eq. (2.10):

$$\varphi_{\text{metal}} = \frac{1}{S}\int_S \varphi \, \mathrm{d}S. \tag{2.12}$$

Interface weak form The weak form of the Robin BCs (2.10) is found multiplying trial function u by the test function v and integrating over the boundary:

$$-\int_{\partial\Omega} \sigma \frac{\partial\varphi}{\partial n} v \, \mathrm{d}s = \sum_k \int_{\Gamma_R^k} y_k(\varphi - \varphi_{\text{metal}_k}) \, \mathrm{d}s. \tag{2.13}$$

To allow for complex numbers, similarly to the capacitive Poisson equation (2.2), the test and trial functions are split in real and imaginary parts. The surface admittance y_k is split into interface conductivity g and inter-

face susceptivity b, i.e. $y_k = g + ib$. Now the Robin BC can be written as:

$$\int_{\Gamma_R^k} y_k(u - \varphi_{\text{metal}_k})v \, \mathrm{d}s = \int_{\Gamma_R^k} (g + jb)((u_r + ju_i) - \varphi_{\text{metal}_k})(v_r + jv_i) \, \mathrm{d}s \tag{2.14}$$

Expanding this equation yield to the real part and imaginary parts:

$$\text{Real: } \int_{\Gamma_R^k} (gu_rv_r - gu_iv_i - bu_iv_r - bu_rv_i) \, \mathrm{d}s + \int_{\Gamma_R^k} (b\varphi_{\text{metal}_k}v_i - g\varphi_{\text{metal}_k}v_r) \, \mathrm{d}s \tag{2.15}$$

$$\text{Imaginary: } \begin{aligned} &\int_{\Gamma_R^k} (gu_iv_r + gu_rv_i + bu_rv_r - bu_iv_i) \, \mathrm{ds} - \\ &\int_{\Gamma_R^k} (g\varphi_{\text{metal}_k}v_i + b\varphi_{\text{metal}_k}v_r) \, \mathrm{ds} \end{aligned} \tag{2.16}$$

The variational formulation $a(u, v) = L(v)$ needs all integrals depending on the trial function u on the left hand side ($a(u, v)$) and the remaining integrals on the right hand side ($L(v)$). Thus, the real and imaginary integrals from the Robin BC are split into two parts, with subscripts i and r indicating the imaginary and real parts, respectively:

$$a_r(u, v) = \sum_k \int_{\Gamma_R^k} (gu_rv_r - gu_iv_i - bu_iv_r - bu_rv_i) \, \mathrm{d}s, \tag{2.17}$$

$$a_i(u, v) = \sum_k \int_{\Gamma_R^k} (gu_iv_r + gu_rv_i + bu_rv_r - bu_iv_i) \, \mathrm{d}s, \tag{2.18}$$

$$L_r(v) = \sum_k \int_{\Gamma_R^k} (g\varphi_{\text{metal}_k}v_r - b\varphi_{\text{metal}_k}v_i) \, \mathrm{d}s, \tag{2.19}$$

$$L_i(v) = \sum_k \int_{\Gamma_R^k} (g\varphi_{\text{metal}_k}v_i + b\varphi_{\text{metal}_k}v_r) \, \mathrm{d}s. \tag{2.20}$$

Geometrical models

In this study, three different geometries were used.

A four-layered sphere model (M1, Fig.2.1A) representing the human head containing brain, cerebrospinal fluid (CSF), skull and scalp. The radii of the spheres are 9.0 cm, 8.5 cm, 8.0 cm and 7.9 cm, respectively [39, 7, 132]. The mesh consists of about 12 million tetrahedra with a smallest inradius of 26 μm and a largest of 0.5 cm. The script to generate the mesh used in this paper has been described in [132].

The second geometric model (M2, Fig. 2.1B) corresponds to a multi-electrode array (MEA) set-up used in [97]. The volume consists of a cylinder (diameter: 19mm, height: 5mm) filled with Ringer's solution and a rectangular slab of neuronal tissue with dimensions similar to an embryonic mouse hindbrain-spinal cord. The MEA was positioned at the bottom of the tissue, with 60 conical recording electrodes (base diameter: 80 μm, height: 80 μm). The stimulating electrode was modeled as a rectangular surface (width: 60 μm, length: 250 μm) on the same MEA (Fig. 2.1B, inset in upper panel). An external cylindrical ground electrode (diameter: 2 mm, height: 4.3 mm) was represented by a cavity in the Ringer's solution subdomain (Fig. 2.1B, purple cylinder positioned in the lower right region). We used the mesh that was generated by [97] using FEMLAB 3.1a (COMSOL AB, Stockholm, Sweden). It consists of 63,214 tetrahedra.

The third geometry is a realistic head model (M3, Fig.2.1C) segmented in scalp, skull, CSF, grey and white matter (Ernie, provided in SimNIBS, [185]). For the grey and white matter, anisotropic conductivities estimated in SimNIBS [185] were used during the FEM calculations. The mesh contains approximately 4.2×10^6 tetrahedra, where the inradius of each tetrahedra is below 1 mm.

Simulation set-ups

The FEM simulations are performed using the open-source program FEniCS [3, 117]. All simulations were done with Lagrange finite elements using the PETSc Krylov Solver with either the Conjugate Gradient method or generalized minimal residual method (GMRES) to solve the linear systems. Note however that a variety of other solvers is available.

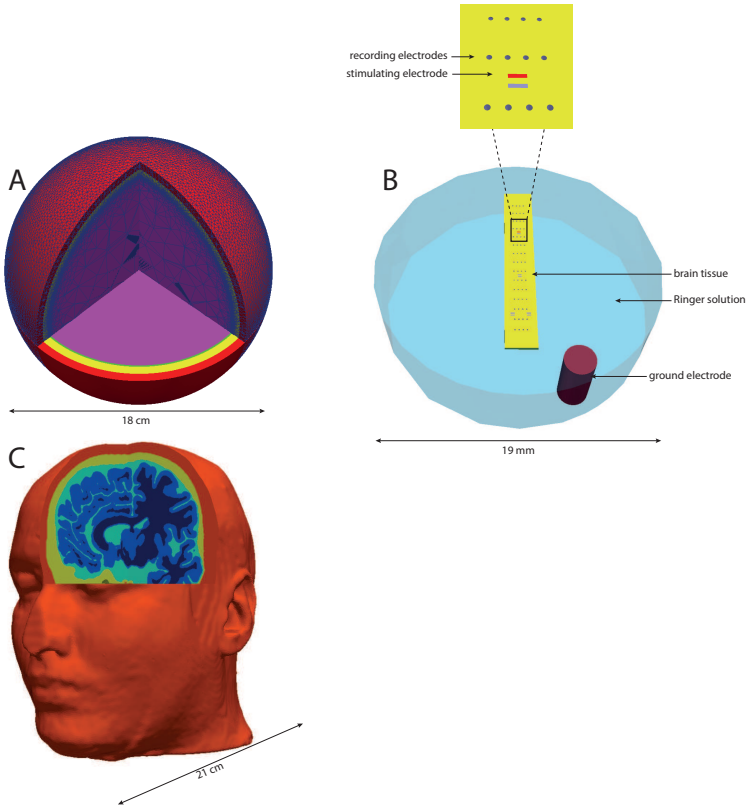

Fig. 2.1: Geometrical models M1-M3. A) Four-sphere head model [132], where the layers represent the different conductivities of the brain, CSF, skull and scalp compartments. B) Bottom view of an experimental MEA set-up [97] with a 200 μm thick square slab of brain in the middle. The remainder of the cylinder is filled with Ringer's solution (in blue). In the bottom right corner of the cylinder, the external cylindrical ground electrode (in purple) is positioned. On the tissue surface (in yellow) 60 distributed conical recording electrodes (in grey) and one square stimulating electrode (in red) are placed. Other square electrodes were not used for stimulation. The top panel displays a magnified region containing 8 recording and the stimulating electrode. C) Realistic head model [185], segmented in scalp (red), skull (yellow), CSF (green), grey (light blue) and white matter (blue).

Table 1: Isotropic conductivities and mean conductivities of the anisotropic white and grey matter (left column) [145]. Dielectric properties for tissues at 10 MHz calculated using the four-term Cole-Cole expression [55]. This frequency serves as an example and other frequencies yield comparable results. The frequency of biopotentials and stimulating electrodes is generally below 10 kHz.

Name	σ (S/m)	σ (S/m) 10 MHz	ε_r 10 MHz
Grey	0.276	.29	320
White	0.126	.16	176
CSF	1.654	2	109
Skull	0.010	.04	36.8
Scalp	0.465	.2	362

Study 1: The linear system was numerically solved in the four-sphere head model (M1) using an average zero reference and compared to the analytical solution [132]. The dielectric parameters σ and ε_r of the four layers were calculated using the four-term Cole-Cole expression [55] at 10 MHz (Table 1). This frequency serves as an example and other frequencies yield comparable results. Furthermore, since there is no agreement on the correct dispersive dielectric parameters [55, 128, 201], the values in this paper serve as an example. We solved the capacitive Poisson equation (2.2) with the homogeneous Neumann BC (2.3) on the outer surface. Dipoles were positioned at depths from 1 mm to 5 mm under the grey matter surface and oriented radially, tangentially or at a 45-degree angle. Dipoles were approximated with a positive and negative monopole of magnitude 100 μA, at 1 mm distance from each other. Relative Differences ($RD = \frac{1}{N}\sum_{i=1}^{N}\frac{|\phi_i-\psi_i|}{\max|\psi|}$), where ϕ_i is the numerical solution at location i, ψ_i the analytical solution and N the number of locations, were calculated on the surface between brain tissue and CSF at 32,400 evenly

distributed locations to compare the analytical and numerical solutions. These locations on the brain surface represent ECoG point-electrodes.

Study 2: The capacitive Poisson equation (2.2) was solved in M2, taking into account four combinations of capacitive dispersive material effects: a) capacitive tissue and a capacitive electrode interface surface admittance, b) capacitive tissue and a pseudocapacitance electrode interface surface admittance, c) dispersive tissue and a capacitive electrode interface surface admittance, d) dispersive tissue and a pseudocapacitance electrode interface surface admittance. A 200 μs rectangular pulse was applied by the stimulating electrodes and decomposed in 50,001 frequencies (between 0 and $1/(2\ \mathrm{dt})$ Hz, where dt is 10 μs). In the dispersive case, the conductivity and permittivity values of the tissue and Ringer's solution were calculated for each frequency using the four-term Cole-Cole equation (Eq (8), [55]). For the capacitive case, the conductivity and permittivity values were calculated using the four-term Cole-Cole equation at the average frequency of the pulse FFT. The ground and stimulating electrode surface admittance was implemented as a Robin BC (2.10). The pseudocapacitive case consisted of an equivalent impedance of a pseudocapacitance (Eq. (2.9)) and a charge transfer resistance (Eq. (2.11)) set up in parallel [29]. The capacitive electrode case used the capacitance and resistance of the parallel pseudocapacitive circuit at the average frequency of the pulse FFT. Note that the capacitive reactance of the electrode remains dependent on frequency.

Study 3: As a proof of principle, Eq. (2.1) with BC (2.3) was solved in a realistic head model (M3). Tissue properties (Table 1 first column) were resistive and anisotropic. The dipole was tangentially and radially oriented with regard to the average normal of one of the electrodes at a distance of 1 mm.

Implementation

The workflow of the simulation pipeline FEMfuns for the potential is visualized in a schematic overview (Fig. 2.2) and has the following steps:

1. Create the mesh (top yellow boxes in Fig. 2.2)
   (a) Define the different materials into separate subdomains and mark interfacial regions as boundaries

   (b) Convert geometry to FEniCS format
2. Choose simulation parameters for the (`Parameters` module in Fig. 2.2):
   (a) Type and location of source (e.g. electrode, monopole, dipole)
   (b) Capacitive/resistive/dispersive tissue (Table 1)
   (c) Electrode-tissue interface (Eq (2.10))
3. Create FEM simulation class instance (`FEM_simulation` in Fig. 2.2)
4. Run simulation (`main` in Fig. 2.2)
5. Visualize
6. Compare to analytical solutions (when possible)

Since only simple geometries can be created within FEniCS, other tools like `gmsh` [57] or integrated realistic head models [185] should be considered for the generation of a tetrahedral mesh. The steps performed outside `Python`/FEniCS environment are indicated in yellow in Fig. 2.2. In this study we used both `gmsh` [57] and SimNIBS [185]. After creating the mesh, parameters regarding the materials, sources and electrodes need to be set (Fig. 2.2, in red are the `Python` classes and their use and in green the main output is shown). A subsection of the mesh can be cut out, creating a new smaller mesh. This is useful when solving for the potential in a whole head is not necessary (e.g. when using microelectrodes close to the source). The `FEM_simulation` class contains functions (indicated in pink, in blue is its main output) which set-up and solve the linear system. Dipole locations can be calculated (`source_locations`) based on distance and orientation with respect to an electrode, as well as inter-dipole distances. A procedure for mesh refinement in a region of interest is implemented, for example to study convergence, where a minimum cell inradius can be set. The stiffness matrix A_{ij} is computed in FEniCS with the `main` function. Based on the parameters that are chosen, resistive, dispersive or capacitive properties are used in the FEM calculation when calling `main`. In the frequency dependent analysis, a square pulse, alpha function or sine wave can be used as the activity waveform (e.g., `make_pulse`). Alternatively, a custom combination of frequencies can be given as input as well.

The `Python` code to obtain potentials from stimulating or recording electrodes, with three examples comparable to study 1-3, is available under the GNU General Public License version 3 at https://github.com/meronvermaas/FEMfuns.

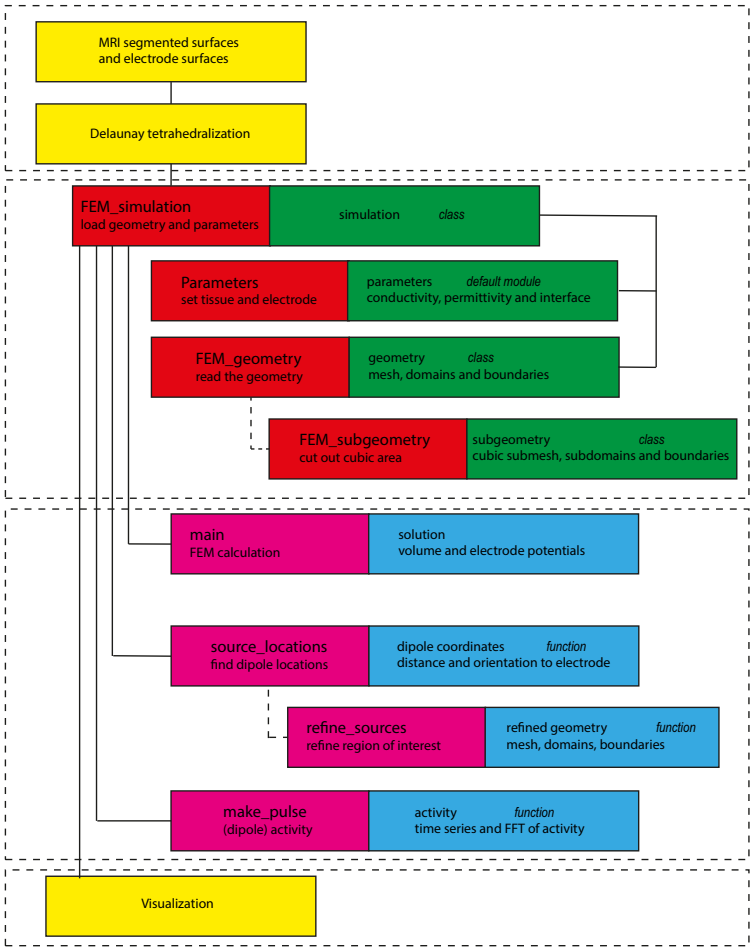

Fig. 2.2: Sketch of the FEniCS pipeline (workflow goes from top to bottom). Red background indicates `Python` classes, green background the (main) output of respective the class. Purple background indicates functions in a class, blue the (main) output of the function and yellow indicates steps outside `Python`/FEniCS.

2.3 Results

Study 1: Validation

In study 1 we validated the accuracy of the numerical simulation in a four-sphere model with resistive and capacitive material properties (2.2) by comparing it with the analytical solution. Numerical and analytical potentials were compared on the outer surface of the sphere representing the cortical surface, which is comparable to an ECoG grid location. These observation points are close to the dipolar source (human cortical thickness is at most 5 mm), with the distances between the dipole and the surface ranging from 1 mm to 5 mm. The analytical solution adopted in this comparison consists of a series expansion [132] with 1000 terms. Only the conductivity in the analytical solution was changed into the admittivity, containing a real (conductance) and imaginary (susceptance) part. We computed the relative difference (RD) in the frequency domain at 10 MHz and visualized the results in Fig. 2.3. The RD values are typically small (below 0.04), whereas dipoles very close to the brain surface display the largest RDs. This is visible for the radial dipole in particular.

Study 2: Dispersive Electrode and Tissue Implementation

The effect of capacitive and dispersive materials under voltage-controlled stimulation was investigated in this study and the results are visualized in Figure 2.4. The applied square pulse is shown in blue. The line in red shows the voltage waveform at a vertex on the inside of the interface when the dielectric properties of the tissue are dispersive (conductivity $\sigma(\omega)$ and relative permittivity $\epsilon_r(\omega)$) and the electrode interface is pseudocapacitive (a parallel pseudo-capacitance and charge transfer resistance). Dispersive tissue and a parallel RC electrode interface are shown in green, capacitive tissue and pseudocapacitive electrode interface in purple and capacitive tissue and RC electrode interface in light blue.

From Fig. 2.4 we notice that the voltage waveform at a vertex on the inside of the interface is deformed due to capacitive effects. The deformation of the potential at the vertex on the inside of the interface can mainly be explained by the time constant of the circuit representing the electrode interface. The two curves with a pseudocapacitive interface are overlapping (green and light blue curves), as well as the curves with an RC electrode

interface (red and purple curves). Thus, in this geometry, the effect of the dispersive compared to capacitive tissue properties is negligible. Note the oscillations due to the Gibbs phenomenon which are minimized by increasing the padding around the pulse and the sampling frequency [58]. These results indicate substantial capacitive and dispersive effects due to the electrode-electrolyte interface when using stimulating electrodes.

Study 3: Realistic Head Model

As a proof of concept, in the last example we solved Eq. (2.1) in a realistic head model with anisotropic resistive material properties. A radial dipole was positioned at 1 mm below the surface of one of the electrodes and the resulting potential distribution is shown in Fig. 2.5. In Fig. 2.5A the potential distribution resulting from a tangential dipole is displayed on the cortical surface. The transition from the positive to the negative potential can be observed clearly on the cortical surface. Figure 2.5B illustrates the potential distribution of a radial dipole on the cortical surface. The different polarity of the gyrus and the sulcus due to the relative angle of the surface with the dipole can be observed.

2.4 Discussion

The purpose of this paper is to describe and introduce a `Python`-based framework centered around FEniCS for FEM forward calculations in electrophysiological recordings. We developed FEM scripts which allow neuroscientists to compute both resistive and frequency dependent capacitive material properties. Using three geometries, we show examples of the use of the FEMfuns pipeline. The main novelty that is presented here is the possibility to easily include electrode and capacitive material effects.

In study 1, we looked at dipole positions at several depths in a four-sphere head model and visualized the error at the surface directly on top of the brain, where ECoG grids are positioned (results in Fig. 2.3). The accuracy of the *capacitive* Poisson equation (2.2) was calculated, which expands on the original approach where the *resistive* Poisson equation (2.1) is solved on top of the scalp [132]. With a tetrahedron inradius of 26 μm at the region of interest, accurate numerical estimates were achieved with relative error values below 0.04. The RDs for dipoles very close to

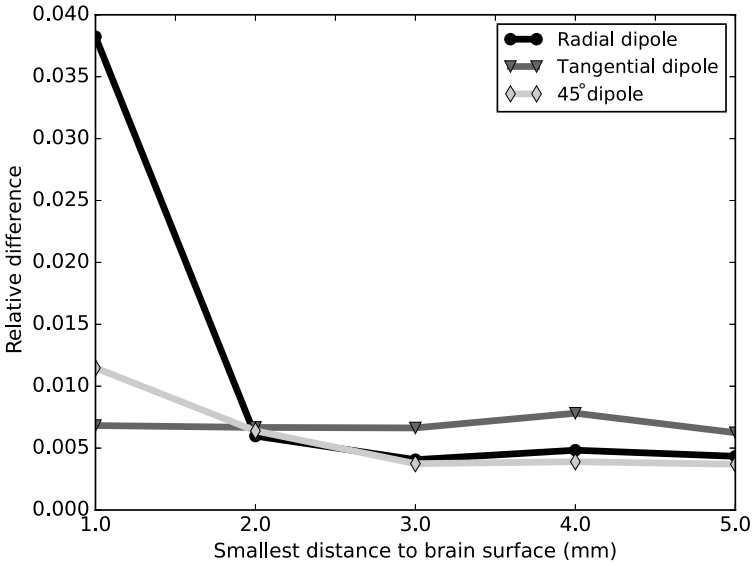

Fig. 2.3: Relative difference (RD) of ECoG potentials calculated with the four-sphere model for a radial, tangential, and 45-degree dipole. Both capacitive and resisitive electrical properties of the tissue are taken into account via Eq. (2.2). The depth of the dipole below the cortical surface is varied (x-axis), error values are calculated at the surface of the grey matter.

the brain surface are the highest. The two monopoles that were used to approximate a dipole need to be sufficiently close to each other. If the distance between the dipole and the recording location is much larger than the distance between the monopoles, the dipole will be more accurately approximated. Overall, these results demonstrate that dispersion effects can be accurately modeled.

Electrode effects have been studied extensively in stimulation studies [165, 24, 29, 65]. Because of the reciprocity theorem, stimulating electrodes are useful models for recording electrodes as well. Non-linear behavior of the electrode-electrolyte interface is expected at high frequencies and at low frequencies provided that the applied signal amplitude is high [164]. Recording electrodes are unlikely to show major non-linear effects be-

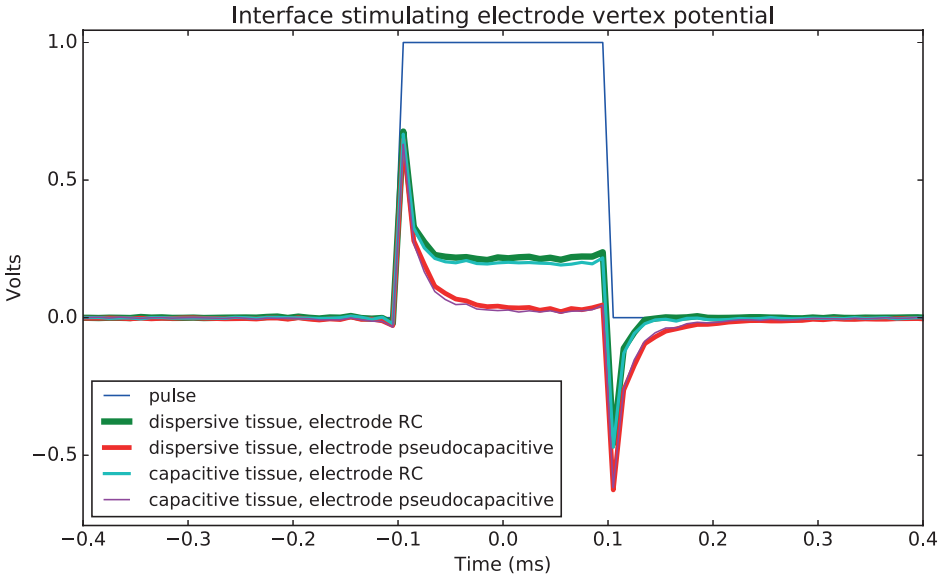

Fig. 2.4: Waveform potential at a stimulating electrode vertex. Frequency decomposition of a stimulating square pulse allows to infer the effect of dispersive material [55]. The dielectric properties of the electrode-electrolyte interface are calculated with a parallel pseudocapacitive component and resistance [29] or a capacitive component and resistance at the average frequency of the FFT. The original pulse and pulses at a vertex at the interface of the stimulating electrode are plotted and the combinations of electrode interface and tissue properties are indicated in the legend.

cause the charge transfer resistance, Eq. (2.11), dominates the interface impedance.

In study 2, dispersion effects of the electrode interface [29] and the tissue properties [55] were examined in the stimulating electrode configuration (Fig. 2.4). The shape of the simulated voltage waveforms is comparable with dispersion effects reported in the literature [24, 65]. As the driving potential amplitude and frequency increase, the dispersion effect becomes more noticeable [29]. The interface impedance acts as a high-pass filter in study 2 (i.e., the interface time constant is short compared to the

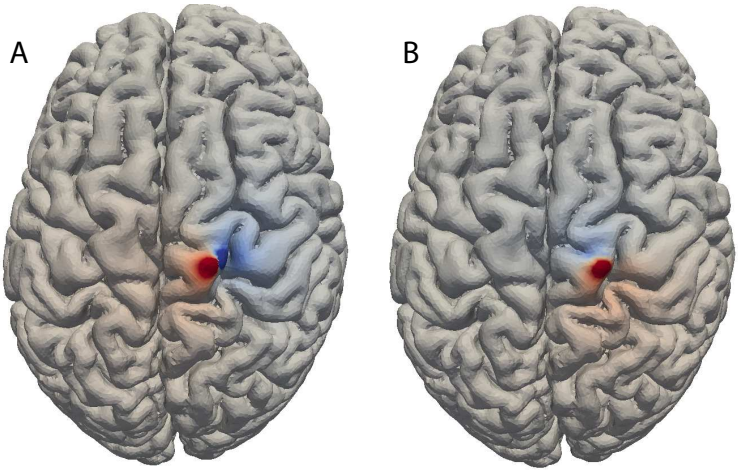

Fig. 2.5: Grey matter region of potentials calculated in a realistic head model, with a tangential dipole left and radial dipole right. The dipole is placed 1 mm below the grey matter surface and the colormap is normalized.

time period of the input waveform) [91]. Thus, the charging and discharging of the capacitance is faster than the change of the input waveform.

In our example, due to the small surface area of the recording electrodes, the interface impedance is high (e.g., 400 kΩ at 100 Hz and 6 kΩ at 10000 Hz, using the pseudocapacitive interface impedance). This resulted in negligible interface (capacitive or dispersive) effects of the recording electrodes and it is in line with previous literature which shows minimal effect of the recording electrode [131, 97, 134]. However, if larger electrodes are used, interface effects due to the recording electrode can be observed [143, 158].

As a proof of principle (study 3), the forward solution was computed in a realistic head model with radial and tangential dipoles. The four-sphere model simulations demonstrated that numerical errors are negligible if tessellation is sufficiently fine. With no analytical solution available in the realistic head-model, convergence can be checked using adaptive refinement while monitoring percent change between the solutions.

Other open-source pipelines for solving the EEG and/or the magnetoencephalography (MEG) forward problems with FEM, or simulating electric stimulations are available [70, 138]. Fieldtrip [144], for example, is a MATLAB software toolbox for MEG, EEG, iEEG and NIRS analysis, that includes functions aiming at solving the EEG forward problem with FEM. Fieldtrip internally calls the C++ open source library called SIMBIO ([200], https://www.mrt.uni-jena.de/simbio/). To the best of our knowledge, in Fieldtrip it is not possible to simulate electrical stimulation and neither is it possible to easily change the properties of the electrodes. Another open-access tool dealing with solving partial differential equations in neuroscience is duneuro [142]. Duneuro is an open-source C++ software library based on the DUNE library and its main features include solving the EEG [45] and MEG [151] forward problem and providing simulations for brain stimulation. There are `Python` and `MATLAB` wrappers which extend the usability of the software to a broader audience. In the present implementation of duneuro, neither the capacitive model nor the electric properties of the electrodes are incorporated in the workflow. A further example of open-source tools dealing with simulations in neuroscience is SimNIBS [204], whose aim is to provide an easy-to-use pipeline for conducting brain simulations with FEM in realistically shaped head models. SimNIBS is limited to brain simulations and it is not flexible for adjusting the type of electrode or adding capacitive material properties.

The main limitations of the pipeline concern mesh generation, which currently needs to be done in external software such as FSL [93] or gmsh. Segmentation of the different head materials was not addressed in the current study. Furthermore, currently only tetrahedral mesh elements can be used in FEniCS. While they can fit the complex geometry of the brain better, it requires several non-trivial steps to convert the hexahedral voxels of an anatomical MRI.

A further limitation concerns the time needed for running the simulations. Depending on the geometry, tissue type and electrode implementation, the linear system that needs to be solved can become very large. In this study, the calculation time was around 1.5 hours per simulation for the four-sphere model (M1), 6 s per simulation in the FEM-Fourier example (M2), and under 2 minutes in the realistic head model with anisotropic tissue properties (M3) running on a Intel(R) Xeon(R) CPU E5-2640 v3

@ 2.60GHz processor. Furthermore, to achieve the desired convergence rate and accuracy, the solver, preconditioner, number of iterations and/or convergence tolerance need to be adjusted. For example, when using capacitive tissue, the Conjugate Gradient method will not converge, while GMRES will.

A further advantage of the FEMfuns pipeline, is that it is easy to control factors affecting the convergence. Furthermore, a variety of families (e.g., Discontinuous Lagrange, Nedelec, Raviart-Thomas) and degrees (linear, quadratic or higher) of elements are supported in FEniCS. This means that the pipeline can also be used in combination with neuron simulation software to provide extracellular potentials.

The results of this study have shown the first open-source, easy-to-use and flexible pipeline, allowing for the simulation of multiple material compartments in volume conductor models with as many compartments as needed (e.g., an arbitrary amount of electrode volumes can be used). Resistive, capacitive and dispersive tissue properties can be used and different types of electrode are implemented. Furthermore, the `Python` code can be easily adjusted and extended to meet the users needs.

Information Sharing Statement

The FEMfuns code for using the new methods is publicly available at https://github.com/meronvermaas/FEMfuns and is licensed under the General Public License (GPL) v3. Documentation is provided at github, for support please contact the first author.

3 When to include ECoG electrode properties in volume conduction models

M Vermaas, MC Piastra, TF Oostendorp, NF Ramsey, and PHE Tiesinga. This Chapter consists of a paper that has been published in Journal of neural engineering (2020).
https://doi.org/10.1088/1741-2552/abb11d

Abstract

Objective

Implantable electrodes, such as electrocorticography (ECoG) grids, are used to record brain activity in applications like brain computer interfaces. To improve the spatial sensitivity of ECoG grid recordings, electrode properties need to be better understood. Therefore, the goal of this study is to analyze the importance of including electrodes explicitly in volume conduction calculations.

Approach

We investigated the influence of ECoG electrode properties on potentials in three geometries with three different electrode models. We performed our simulations with FEMfuns, a volume conduction modeling software toolbox based on the finite element method.

Main results

The presence of the electrode alters the potential distribution by an amount that depends on its surface impedance, its distance from the source and the strength of the source. Our modeling results show that when ECoG electrodes are near the sources the potentials in the underlying tissue are more uniform than without electrodes. We show that the recorded potential can change up to a factor of 3, if no extended electrode model is used.

In conclusion, when the distance between an electrode and the source is equal to or smaller than the size of the electrode, electrode effects cannot be disregarded. Furthermore, the potential distribution of the tissue under the electrode is affected up to depths equal to the radius of the electrode.

Significance

This paper shows the importance of explicitly including electrode properties in volume conduction models for accurately interpreting ECoG measurements.

Keywords: Finite element method, ECoG, Electrode properties, Forward problem

3.1 Introduction

Brain-computer interfaces (BCIs) translate recorded neuronal signals into input for a computer system, e.g., to control communication software [194]. To improve upon BCIs, recordings of relevant neuronal population activity need to be acquired with high resolution, to capture the detail of the cortical topography. In order to achieve that, both the precise placement of the electrode grid on the cortex and the electrode properties, such as the electrode size and material, need to be optimized, for instance, with regard to the subject's head anatomy [181]. Designing an optimal electrode configuration in a sophisticated manner requires a description of the relation between the spatial distribution of neural current sources and the recorded electrophysiological data, such as electroencephalography (EEG) and electrocorticography (ECoG). In addition, accurate electrode models might increase the accuracy of source localization results [157, 158].

Volume conduction models are used to solve the forward problem, i.e., compute the electric potential in the brain given by a known source. Many factors can be included in the forward computations, such as skull anisotropy [124], tissue inhomogeneities and anisotropies [23], and dispersive tissue and electrode properties [65]. Modeling of recording electrodes is commonly approached by incorporating the electrodes as voltage measurement devices with infinite input impedance and a surface area of zero, i.e., the so-called point electrode model [171, 143, 207, 158].

However, if the electrodes are relatively large or the contact impedance is relatively low (e.g. in EEG [100]), shunting effects due to the electrode-electrolyte interface occur [143, 158]. The potential within the electrode is homogeneous and thus the potential under the interface becomes more similar to the one of the electrode. In a multi-electrode array (MEA) simulation [136], it was found that the effects of not including the electrode in the model are negligible when the distance between the electrode and the source is at least 2 times the electrode radius. The effects of the electrodes are negligible for most MEAs, considering their small surface area. However, these effects are expected to be especially relevant in ECoG because of the large electrode surfaces close to the current source covering

a relative large area. Since a low contact impedance is desired to achieve a high signal-to-noise ratio [110], not including electrode shunting in the model can lead to erroneous results of forward simulations.

In this work, we investigated the influence that ECoG electrode properties have on the simulated recorded potentials in volume conduction models, as well as on the distribution of the extracellular potential under the electrode surface. The Finite Element Method for useful neuroscience simulations [195] (FEMfuns[1]) was used as the forward simulation method, because of its flexibility in including sub-domains and interior and exterior boundary conditions representing the electrodes. This study aims to discover what type of electrode model should be used when recording from large electrodes relatively close to the source. Several parts of the recording device were explicitly modeled, for example, the metal part of the electrode, which generally is neglected because of the high input impedance of the amplifier. The importance of a detailed electrode model was tested using various source configurations and geometries and a general recommendation is provided of when an electrode model should be used.

3.2 Methods

Forward model

The electric potential φ generated in the brain can be computed through the quasistatic approximation of Maxwell's equations [153]:

$$-\nabla \cdot (\sigma \nabla \varphi) = \nabla \cdot \mathbf{J}_p, \quad \text{in } \Omega, \tag{3.1}$$

with a given primary current density $\mathbf{J}_p$ (current produced by neuronal activity or from stimulating electrodes) in a medium Ω with conductivity σ.

A homogeneous Neumann boundary condition (BC) is applied on the exterior (non-electrode) boundary $\partial\Omega$,

$$\sigma \nabla \varphi \cdot \boldsymbol{n} = 0, \text{ on } \partial\Omega, \tag{3.2}$$

where $\boldsymbol{n}$ is the unit outer normal vector on $\partial\Omega$. The insulating condition (3.2) ensures that no currents flow out of the boundary.

[1] https://github.com/meronvermaas/FEMfuns

Electrode-electrolyte interface In this work we focused on modeling the recording electrodes as surfaces or volumes and incorporated a real-valued contact impedance representing the interface. The interface currents are described as Faradaic reactions in a thin-layer approximation with a real-valued surface admittivity y_k (S/m^2) expressed by the Robin BC applied at the k-th electrode:

$$-\sigma\frac{\partial\varphi}{\partial n} = y_k(\varphi - \varphi_{\mathrm{metal_k}}) \text{ on } \Gamma_{\mathrm{R}}^k, \quad k = 0, 1, \ldots \tag{3.3}$$

where $\varphi_{\mathrm{metal_k}}$ is the voltage of the k-th electrode and Γ_{R}^k is the boundary of the k-th electrode. In the case of recording electrodes, equation (3.3) needs to be used self-consistently, since for each electrode $\varphi_{\mathrm{metal}_k}$ is unknown. Using a Lagrange multiplier, $\varphi_{\mathrm{metal}_k}$ with electrode surface S can be found in a standard saddle-point problem by requiring:

$$\varphi_{\mathrm{metal}_k} = \frac{1}{S}\int_S \varphi \, \mathrm{d}S. \tag{3.4}$$

Three geometries and model parametrizations

Three studies were performed to investigate the effect of the presence of the electrode surface on the recorded potential and in the tissue under the electrode. In all the studies Lagrangian FEM [200] was applied to simulate the electric potential generated in a volume conductor by a known source. The FEM simulations were performed using the open-source forward modeling implementation in FEMfuns[2], which is built upon the open-source software FEniCS [3, 117].

Validation with in-vitro data

In the first study, a validation was performed on an in-vitro MEA set-up [97]. The geometric model (M1, Fig. 3.1A) that corresponds to the MEA set-up consists of a cylinder (diameter: 19 mm, height: 5 mm) filled with Ringer's solution (Fig. 3.1A, blue). The MEA was positioned at the bottom

[2] Code from FEMfuns allows neuroscientists to solve the forward problem in a variety of different geometrical domains, including various types of source models and electrode properties, such as resistive and capacitive materials, and can be found at https://github.com/meronvermaas/FEMfuns

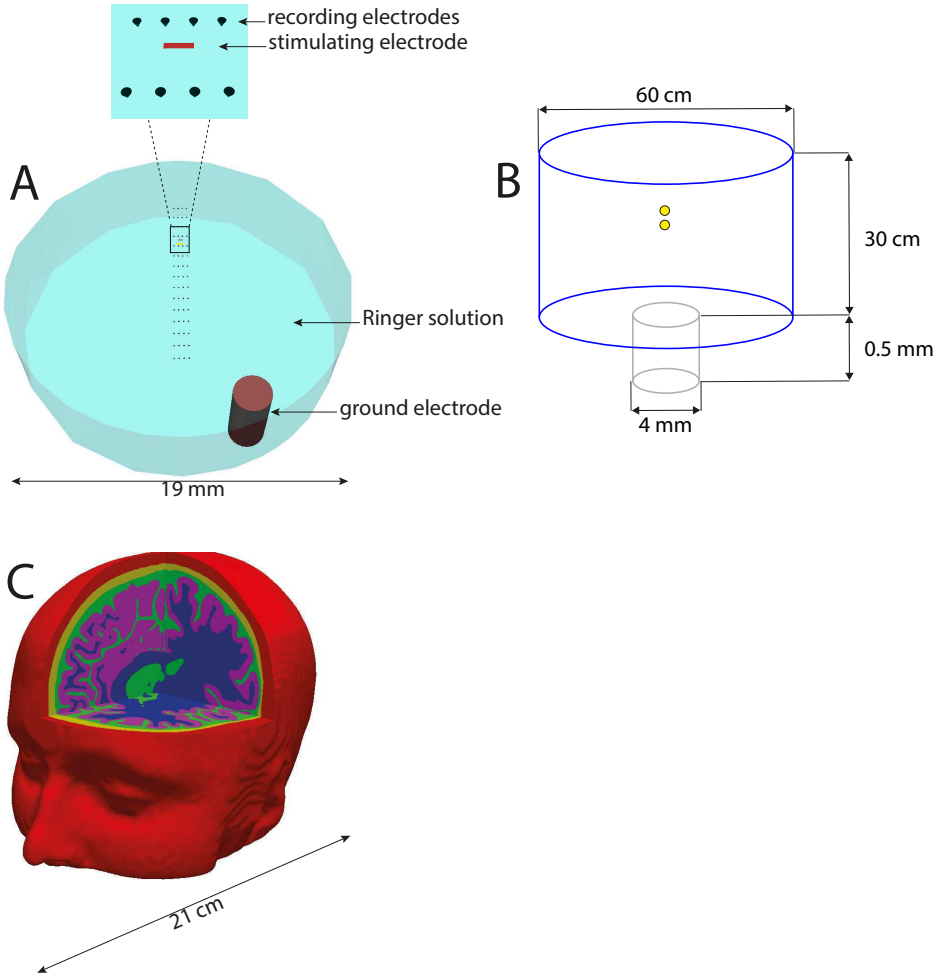

Fig. 3.1: Geometrical models M1-M3. A) Bottom view of an experimental MEA set-up [97] cylinder filled with Ringer's solution (in blue). In the bottom right corner of the cylinder, the external cylindrical ground electrode (in purple) is positioned. On the cylinder bottom surface 60 distributed (in a 4 by 15 rectangular grid) conical recording electrodes (in black) and one square stimulating electrode (in red) are placed. The top panel displays a close-up containing 8 recording sites and the stimulating electrode. B) 3D schematic representation (not to scale) of the semi-infinite cylinder with a perpendicular bipole. C) Realistic head model [185], with scalp (red), skull (yellow), CSF (green), grey (purple) and white matter (blue) compartments.

of the cylinder, with 60 conical recording electrodes (base diameter: 80 μm, height: 80 μm). The stimulating electrode was modeled as a rectangular surface (width: 60 μm, length: 250 μm) on the same MEA (Fig. 3.1A, red rectangle in the close-up top panel). An external cylindrical ground electrode (diameter: 2 mm, height: 4.3 mm) was represented by a cavity in the Ringer's solution subdomain (Fig. 3.1A, purple cylinder positioned in the lower right region). We used the mesh that was generated by [97] using FEMLAB 3.1a (COMSOL AB, Stockholm, Sweden), which consisted of 63,214 tetrahedra.

With this MEA set-up (M1), we replicated the simulation performed by [97], comparing modeled electric potentials to experimentally recorded potentials. In addition to [97], the range of the nodal potential values on each recording electrode surface was computed. The whole domain was uniformly filled with Ringer's solution ($\sigma_{\text{Ringer}} = 1.65$ S/m), where the purely resistive version of Poisson's equation was solved, i.e. Eq.(3.1), with the homogeneous Neumann BC (3.2). The stimulating and ground metal voltages (φ_{metal_k} in (3.3)) were set to 754.4 mV and 0 mV, respectively. As reported in [97], surface conductance (y_k in (3.3)) was 338 S/m^2 for the stimulating electrode and 975 S/m^2 for the ground electrode. The experimental data, provided by [97], and our simulated data were compared using a regression analysis.

Electrode shunting

In the second study we investigated the shunting effect of the electrode. We used a geometry (M2, Fig. 3.1B) that is composed of two cylinders: a first cylinder (C1) (height and radius: 30 cm) representing the volume conductor and, a second cylinder (C2) (diameter: 4 mm, height: 0.5 mm) placed at the center of the bottom surface of C1, representing the electrode. The surface area of electrodes is thus 12 mm^2, which is comparable with *Resume II, Medtronic*, ECoG electrodes [194]. C1 is a good representation of a semi-infinite halfspace, i.e., volume conductor with homogeneous Neumann BC at the lower surface and homogeneous Dirichlet BC elsewhere. The mesh was generated with gmsh [57] and contained approximately $17 \cdot 10^6$ tetrahedra, with the tetrahedron inradius ranging between 3 μm and 0.4 cm, being more refined close to the electrode.

The boundary value problem in the semi-infinite halfspace (M2) was governed by Eq. (3.1) with insulating BCs on the bottom Eq. (3.2) of cylinder C1. Homogeneous Dirichlet BCs were applied to the sides and top of C1. In this study we considered three different configurations (for a schematic overview, see Fig. 3.3) for the electrode C2:

a) insulating BCs (3.2) at the interface between C1 and C2;
b) explicit metal subdomain with insulating BCs (3.2) on the outer facets;
c) surface conductance (3.3) at the internal boundary between the tissue and metal region, i.e., between C1 and C2, and the metal subdomain with insulating BCs (3.2) on the outer facets.

Conductivities of the tissue (C1) and metal were 0.3 S/m and 10^7 S/m, respectively. Three surface conductances representing the interface were used. A parallel combination of a pseudo-capacitance and charge transfer resistance yielded interface impedances of 372, 46 and 5.6 Ω at 100, 1000, and 10000 Hz, respectively [29]. As a source model, a perpendicular and parallel oriented bipole source (i.e., a dipole approximated by two monopoles with a magnitude of 1 μA separated by 0.5 mm, with a dipole moment of $5{\cdot}10^{-10}$ Am) was positioned 1 mm above the center of the electrode surface.

In addition, we reported the proportion between the simulated electrode potentials of electrode configuration (a) and the other configurations, (b) and (c), for the perpendicular bipole. The electrode potentials of electrode configuration (a) were calculated using either the point-electrode approximation or the disc-electrode approximation. The point electrode approximation is the simplest and most commonly used electrode approximation [171, 207], where the electrode potential is described as the value assumed at the midpoint of the electrode, disregarding both its size and interface impedance. In the disc-electrode approximation, the average potential on the electrode surface is calculated. The reported proportion between these two electrode potentials for configuration (a) and the other electrode configurations, (b) and (c), indicates by which factor the recorded potential differs if a more complete electrode model is used.

Electrode implementations a) and b) were calculated several times with a bipole source positioned at increasing distances from the electrode. Furthermore, potentials at horizontal cross sections at increasing distance

from the electrode surface were calculated with electrode implementations a) and b) using one bipole at 1 mm distance from the electrode.

Finally, the Root Mean Squared Errors (RMSE):

$$\mathrm{RMSE} = \sqrt{\frac{\sum_{i=1}^{N}(\phi_i - \psi_i)^2}{N}}, \tag{3.5}$$

and the Relative Differences (RD):

$$\mathrm{RD} = \frac{1}{N}\sum_{i=1}^{N}\frac{|\phi_i - \psi_i|}{\max|\psi_i|}, \tag{3.6}$$

where ϕ_i is the numerical solution at location i, ψ_i the analytical solution and N the number of locations, were calculated in a 1 cm cube centered around the electrode position, using electrode implementation a), to compare the analytical [92] and numerical solutions. When the comparison between the solutions of two models is calculated, the RMSE will be called the Root Mean Squared Difference (RMSD).

Realistic head model

In the third study, as a proof of principle, we used a realistic head model (M3, Fig. 3.1C) with scalp, skull, cerebrospinal fluid (CSF), grey and white matter compartments (available in SimNIBS, [185]). Two cylindrical electrode surfaces (≈12 mm^2, 1 cm distance between centers) were manually added using Blender [17] and all head surfaces were subsequently tessellated using TetGen [179]. This resulted in approximately $4.8{\cdot}10^6$ tetrahedra, where the inradius of all tetrahedra was below 0.5 mm. The tetrahedra were comparable to or smaller than the semi-infinite halfspace tetrahedra in M2, being more refined close to the electrode.

The boundary value problem (3.1) with homogeneous Neumann BCs (3.2) on the outer surface was solved in the realistic head model (M3). Tissue properties were resistive with conductivities of the grey and white matter [108], CSF [54], skull [162] and scalp [160] being 0.28, 0.25, 1.59, $3.5{\cdot}10^{-3}$ and 0.17 S/m, respectively. Two electrode models were considered, one perfectly insulating and one consisting of metal with insulating BCs. A bipole radially oriented with regard to the average normal of the surface of

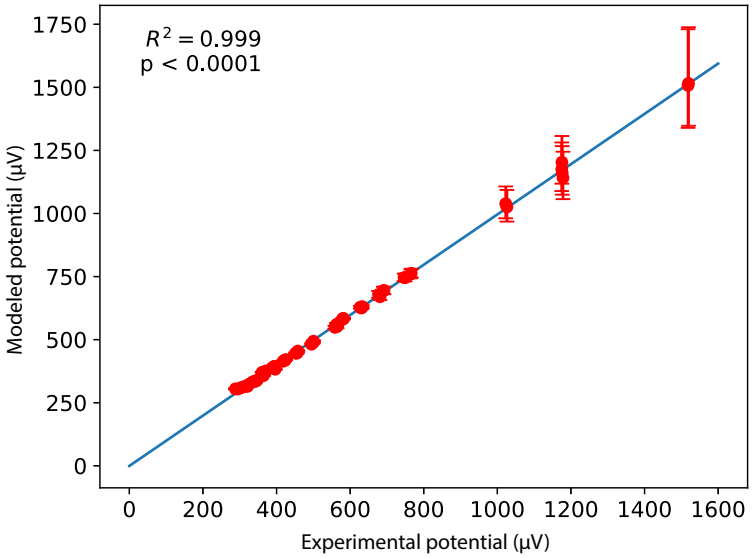

Fig. 3.2: Replication of the validation study in [97]. The red points correspond to the modeled and experimental values. A linear regression (blue line) with $R^2 = 0.999$ and p value < 0.0001 is shown. Furthermore, the total range of nodal potential values on the surface of each electrode is depicted by the red error bars.

one of the electrodes was positioned at a 2 mm distance from the electrode. To make our results specific, we have chosen a bipole consisting of two monopoles of 1 μA separated by 1 mm (i.e., a dipole moment of 10^{-9} Am). As results directly scale with bipole size the calculated values can be easily adapted to the particular situation at hand by scaling.

The difference between the potentials given the two electrode models was computed for tetrahedra in the grey matter within distance of 20 mm from the electrode surface. Box plots of these differences were binned into a range of 1 mm distance from the electrode. The root mean square (RMS) of the potentials was also calculated in bins to show the effect of the electrode relative to the magnitude of the potential.

3.3 Results

Study 1: Validation with in-vitro data

The results of the simulation of this monopolar stimulation experiment [97] are visualized in Fig. 3.2. The electrical potential in this stimulation set-up was recorded at 60 electrodes and compared to experimental recorded values. Using Robin BCs (3.3), as reported by [97], results in an excellent fit between experimental and modeled potentials (Fig. 3.2, $R^2 = 0.999$, $p < 0.0001$).

In addition to [97], we displayed error bars in Fig. 3.2 to indicate the range of the nodal potential values on each recording electrode surface. The recording electrodes closest to the stimulating electrode (i.e., with the highest potential) show the largest range of values along its surface. These results motivated us to further investigate effects of more complete recording electrode models.

Study 2: Electrode shunting

The focus of Study 2 was on the effect of the three different electrode configurations, i.e., (a), (b) and (c), and of the point- versus disc-electrode approximation on the electric potential computed with FEMfuns in a purely resistive medium (M2) according to equation (3.1).

We analyzed and compared the potentials on the midline along the surface of the electrode (in green, Fig. 3.3, left panels) of the geometrical model (M2), see Fig. 3.1B.

Table 2: Ratio between recorded electrode potentials of different electrode models with as the source distribution a perpendicular bipole. The values represent the ratio between the recorded potentials of the insulating electrode model (a) with a disc- and point-electrode approximation (rows) and the more complete electrode models (columns).

	Interface 372 Ω (c)	Interface 46 Ω (c)	Interface 5.6 Ω (c)	Metal (b)
Disc-electrode	1.06	1.2	1.29	1.33
Point-electrode	3	3.4	3.67	3.77

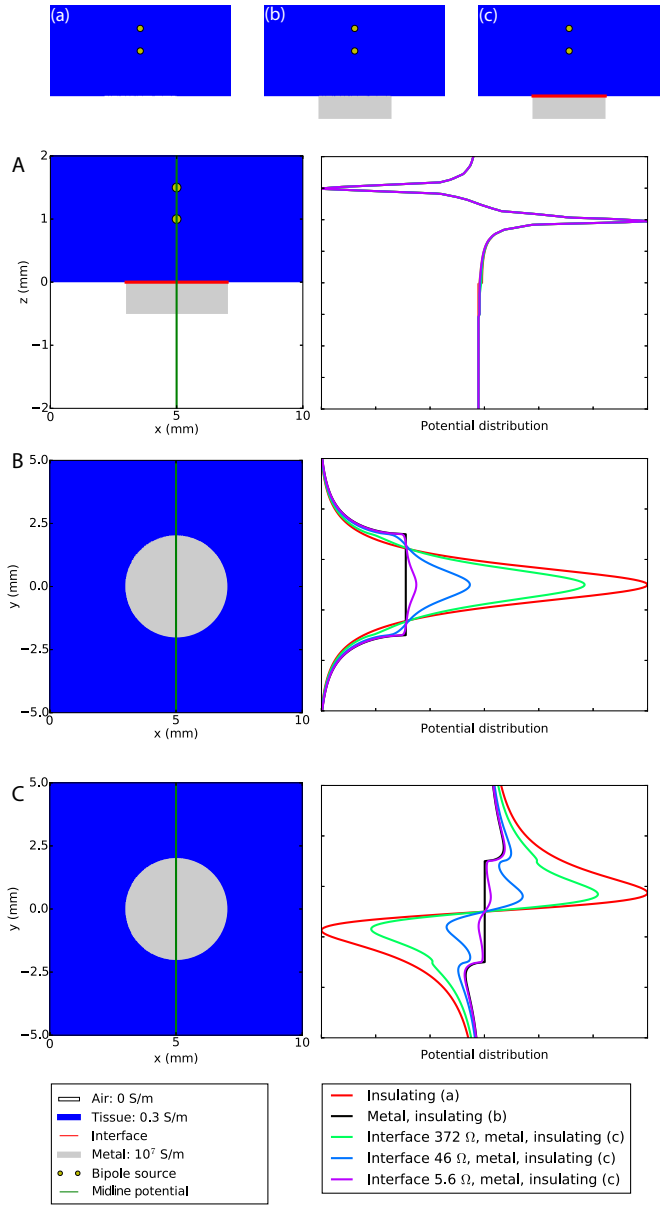

Fig. 3.3: Vertical (A) and horizontal (B, C) cross sections of potential distributions in a semi-infinite cylinder, with in the top panel an overview of the different electrode configurations indicated in the legend (a-c). For a complete overview and description of the domain, see Fig. 3.1B. The potential on the midline along the surface of the electrode is plotted from top to bottom describing: a) only tissue (blue) with no electrode (i.e. insulating BCs), b) tissue (blue) and explicit electrode (grey) domain (insulating BCs at the boundary of the electrode), c) similar to b) but including a thin-layer approximation of the interface ((red), Robin BC with conductivities indicated in the legend). Note the different scaling on the x-axis of the vertical and horizontal cross section. A and B are potential distributions due to a perpendicular bipole, C is the potential when using a parallel bipole at a distance of 1 mm from the electrode surface. Since the magnitude of the potential scales linearly with the magnitude of the bipole, we are interested in the distribution of the potential and not the magnitude, therefore the axis labels are omitted here.

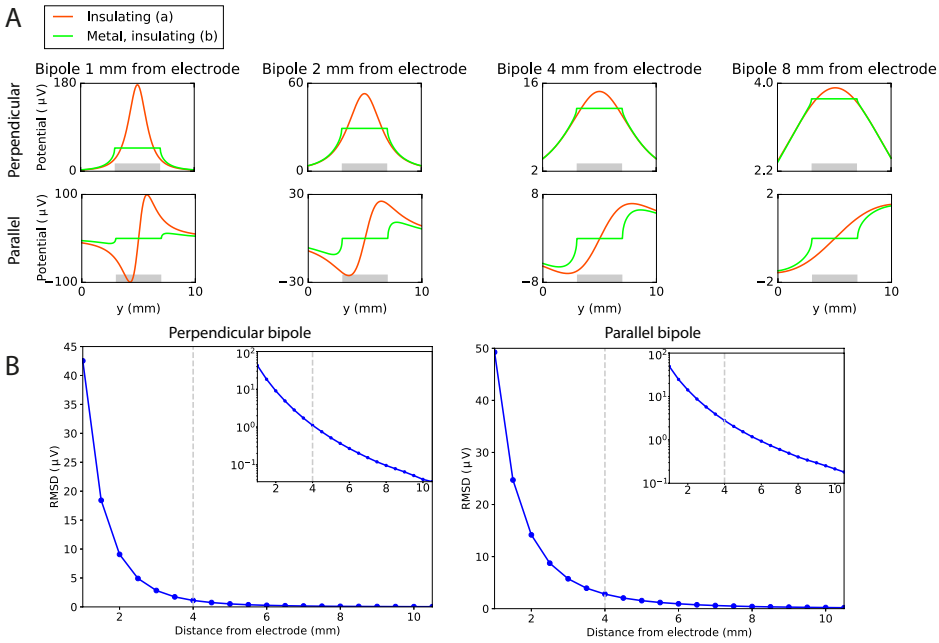

Fig. 3.4: A) Horizontal cross-section of a semi-infinite cylinder displaying the potentials on the midline along the surface of the electrode (in green, Fig. 3.3, left panels) with varying bipole positions (perpendicular bipole in the top panels and parallel bipole in bottom panels). The potential distribution at the metal electrode is shown in green, the potential distribution at the insulating electrode is shown in orange. On the x-axis the electrode is shown as a grey bar. The y-scales of the panels are different. B) Root mean squared differences (RMSD) between the potentials of the two electrode configurations on the midline along the surface of the electrode are shown at increasing distances. The grey dashed line indicates the diameter of the electrode. In the top right corner of the plots, the RMSD is displayed on a logarithmic y-axis.

The results are displayed in Fig. 3.3, where, on the one hand, in the vertical cross section (Fig. 3.3A), we notice that the potential distributions of the five electrode implementations are overlapping in the tissue (the main cylinder, C1). On the other hand, the difference between the insulating (a) and more elaborate electrode implementations (b)-(c) in the horizontal cross section is remarkable. While the insulating electrode implementation (a) leads to a parabolic potential distribution peaking at the center of the cylinder C1 (see Fig. 3.3B perpendicular bipole, Fig. 3.3C parallel bipole), the potential distributions computed with (b) have a constant value within the electrode. As the interface impedance increases, the shape of the potential distribution returns from constant value (b) to the parabolic one in the point electrode model (a). Indeed, with higher impedances, the Robin BC (Eq. (3.3)) reduces to a homogeneous Neumann BC (3.2). Note that the potential magnitude is omitted in Fig. 3.3, since the magnitude of the potential scales linearly with the magnitude of the bipole. Only the potential distribution along the electrode surface is of interest here.

Regarding the point- versus disc-electrode approximation, we inspected the effects of the electrode model on the recorded potential for the perpendicular bipole of Fig. 3.3B. The proportions between the point- and disc-electrode approximation of the insulating electrode (a) and the more complete (configuration (b) and (c)) are reported in Table 2. Since the bipole is centered exactly at the midpoint of the electrode, the point-electrode approximation overestimates the recorded potential by at least factor 3. The disc-electrode approximation is less sensitive to the position of the source, which reduces the effect of the electrode model on the recorded potential by at most 33% (factor 1.33).

The influence of the electrode on the forward solution The difference between an insulating and a metal electrode in relation to its distance to the source was examined. In Fig. 3.4A, the potentials on the midline along the surface of the electrode (in green, Fig. 3.3, left panels) are depicted for four source-electrode distances for a perpendicular and a parallel bipole. Potential values are displayed for a single-point electrode (configuration (a), Fig. 3.4 in orange) and for an explicit representation of the electrode (configuration (b), Fig. 3.4 in green). The RMSD (Eq. (3.5))

between the potentials using electrode configuration (a) and (b) was calculated for source distances between 0 and 10.5 mm from the electrode (Fig. 3.4B). As sources are positioned increasingly further, the voltage becomes more homogeneous in both electrode implementations. Thus, the difference between (a)-(b) is smaller for sources at a distance further than the diameter of the electrode (dashed vertical line in Fig. 3.4B).

From Figure 3.4B, we can indeed see that the RMSD curves decrease almost exponentially for increasing distances (top right insets display the RMSD values on a logarithmic y-axis). The largest RMSD values can be observed for bipole distances within the diameter of the electrode, i.e., 4 mm, for both perpendicular and parallel bipoles (Fig. 3.4B left and right, respectively). From RMSDs of 42.5 μV and 49.2 μV for a bipole at 1 mm from the surface of the electrode, we observe RMSD values of 1.1 μV and 2.7 μV for a bipole at 4 mm from the electrode surface, for the perpendicular and parallel bipoles, respectively. The pace with which the RMSD decreases with the distance of the source depends on the conductivity of the medium, in addition, the magnitude of the potentials scales with the magnitude of the bipole. Therefore, it is essential to consider the magnitude of the RMSD (Fig. 3.4B) with respect to the magnitude of the potentials themselves (Fig. 3.4A).

In addition, the potentials at a horizontal cross section at increasing distances from the electrode surface using one source location was examined using the insulating (a) and metal electrode (b) implementations (Fig. 3.5). The potentials on the midline along the surface of the electrode are depicted at four distances from the electrode for a perpendicular and parallel bipole (Fig. 3.5A). As the distance from the electrode surface increases, the difference between the two implementations decreases. In the bottom panel (3.5B), the RMSD (Eq. (3.5)) between the insulating (a) and metal electrode (b) implementations is illustrated, showing that only close (i.e., at distances of the radius of the electrode) to the electrode, there is an effect in the potential of the tissue underneath the electrode.

Specifically, from RMSD values of 42.5 μV and 49.2 μV on the electrode surface, to RMSD values of 2.9 μV and 6.6 μV at 2 mm away from the electrode, with a drop of 39.6 and 42.6, for perpendicular and parallel bipoles, respectively. The pace at which the RMSD decreases with the distance from the electrode is dependent on the conductivity of the medium

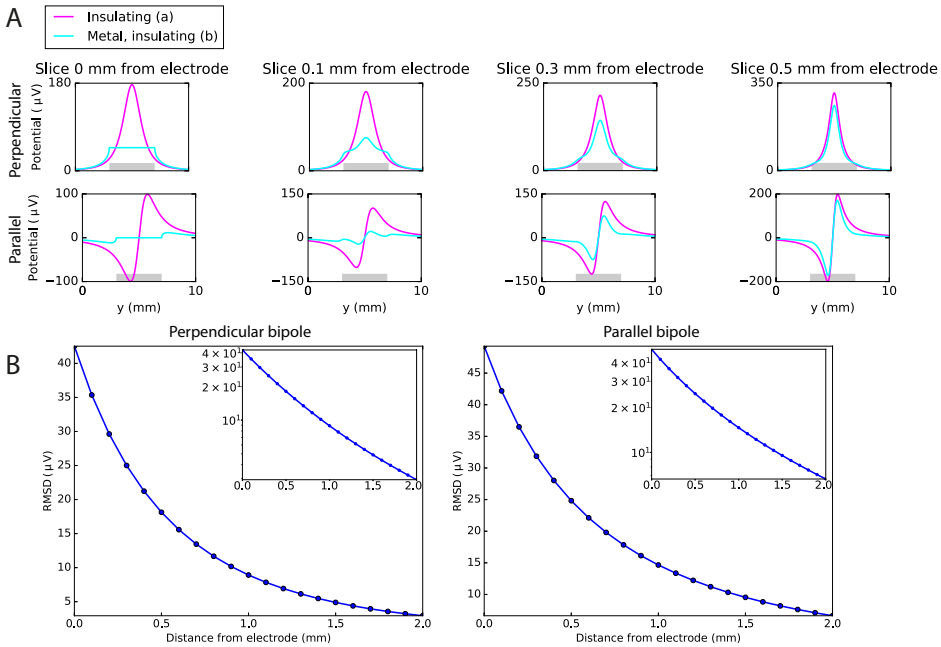

Fig. 3.5: A) Horizontal cross-section of a semi-infinite cylinder displaying potentials on the midline along the surface of the electrode at increasing distances from the electrode surface with a perpendicular (top panels) and parallel (bottom panels) bipole. The bipole is located 1 mm above the electrode. The potential distribution at the metal electrode is shown in blue, the potential distribution at the insulating electrode is shown in pink. On the x-axis the electrode is shown as a grey bar. The y-scales of the panels are different. B) Root mean squared differences (RMSD) between the potentials of the two electrode configurations on the midline along the surface of the electrode are shown as the distance from the electrode increases. In the top right corner of the plots, the RMSD is displayed on a logarithmic y-axis.

and the magnitude of the potentials scales with the magnitude of the bipole. Therefore it is essential to consider the magnitude of the RMSD (Fig. 3.5B) with respect to the magnitude of the potentials themselves (Fig. 3.5A).

The numerical accuracy was checked by calculating the RMSE (Eq. (3.5)) and RD (Eq. (3.6)) for the insulating electrode implementation, since there was an analytical solution available [92]. The RMSE was 0.007 and 0.009, and the RD was $3.6 \cdot 10^{-7}$ and $2.7 \cdot 10^{-7}$ for the perpendicular and parallel bipole, respectively.

Study 3: Realistic head model

As a proof of principle, in the last study, we simulated the effect of electrodes in a realistic head model with resistive material properties (3.1). A radial bipole was positioned at 2 mm below the surface of one of the electrodes. The resulting potential distribution is shown in Fig. 3.6A-C. Insulating electrodes (Fig. 3.6A) lead to an inhomogeneous potential distribution along the surface of the electrode. In contrast, electrodes consisting of a highly conductive metal have a homogeneous potential distribution over the surface of the electrode (Fig. 3.6B). This is comparable to the findings in Fig. 3.4, except that the radial bipole here is not centered on the middle of the electrode. The difference between the simulated results for the insulating and the ones for the metal electrode is between -7 μV and 80 μV (clipped to 7 μV in Fig. 3.6C). Note that the difference is non-zero not only under the surface of the electrode, but also in the nearby gyri (Fig. 3.6C). This is depicted in more detail in Fig. 3.6D. The difference between the two solutions is shown in the box plots as a function of binned distance from the electrode. The root mean square of the actual potentials of both solutions is also plotted for reference. The difference between the two electrode configurations at distances up to 3 mm from the electrode is large, with an RD (Eq. (3.6)) of the binned RMS values of 0.4. As the distance to the electrode increases, the differences become smaller (RD is 0.08 at 5-6 mm).

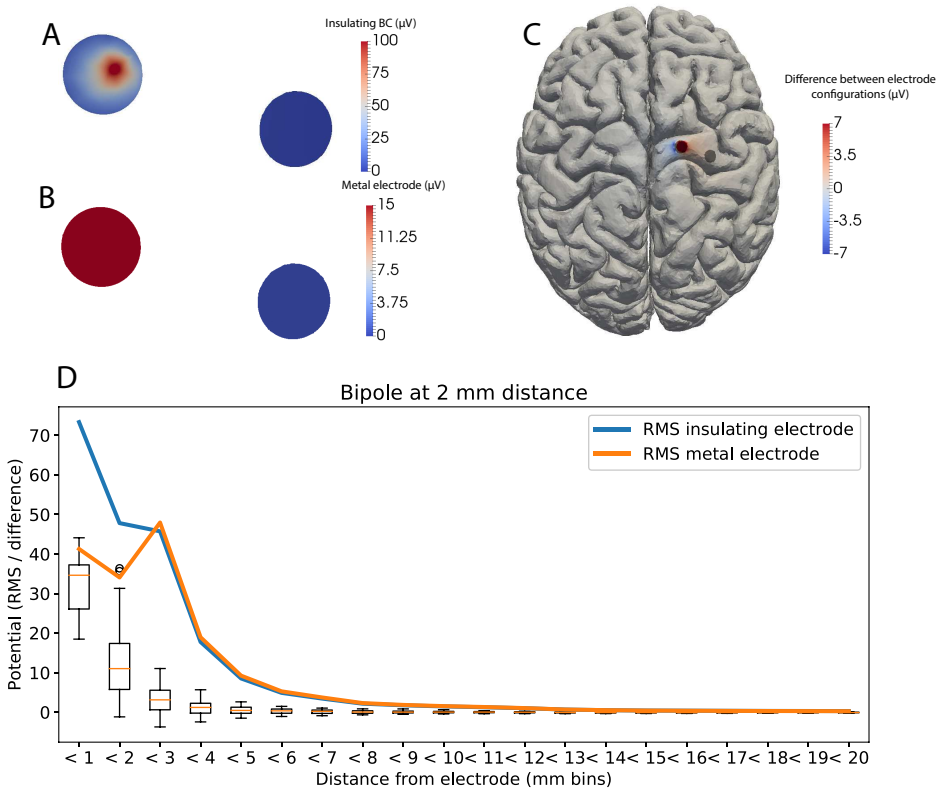

Fig. 3.6: In the top left panels (A,B), the potentials over the surface of electrodes in a realistic head model are displayed, with insulating BCs (3.2) (A) and explicit metal with insulating BCs (B) given by a radial bipole at 2 mm distance below the left electrode. The difference between the potential with and without the metal electrodes is displayed on the grey matter surface (C), and the two electrodes on the central gyrus are overlayed in transparant black. (D) The root mean square of the potentials of all cells at a distance from the electrode are displayed for both electrode implementations with a bipole at 2 mm distance below one of the electrodes. Box plots of the difference between the two solutions at the same distances from the electrode are also shown.

3.4 Discussion

The purpose of this study was to determine whether the presence of ECoG electrodes has a significant influence on the electric potentials on the electrode surface and underlying tissue. Three studies with three different geometrical models were performed using the open-source forward modeling implementation in FEMfuns.

In Study 1, we replicated a stimulation study [97] and in addition illustrated that the potential distribution along the surface of MEA conical electrodes close to the source is inhomogeneous (Fig 3.2). Applying a surface conductance via Robin BCs (3.3) to the recording electrodes did not affect the fit of the model with the experimental data. Thus, the investigators of study [97] used homogeneous Neumann BCs and disregarded an effect of the interface impedance. However, depending on the the magnitude of the surface impedance and the electrode size, the potential distribution under the electrode could be altered.

The effect of the electrode on the potential distribution was further examined in Study 2 using a semi-infinite halfspace and several electrode implementations. The shunting effect of the electrode alters the potential. A low interface impedance and the high metal conductivity ensure an approximately homogeneous potential distribution under the electrode. When the interface impedance goes to infinity the potential distribution over the electrode surface becomes inhomogeneous and varies with distance from the source. This is clear from equation (3.3), where a high surface impedance y_k reduces (3.3) to a homogeneous Neumann BC (3.2).

A number of EEG modeling studies ([143, 158]) conclude that assuming a surface instead of a point is necessary when the electrode surface impedance is very low or the electrodes are large compared to the head. Ref. [158] reports that a more extensive electrode model can improve EEG forward model accuracy. However, this will be mostly prominent in neonatal EEG, where the electrode diameter is large relative to the head. Few studies have considered the effect of recording electrodes close to the source (e.g., ECoG, MEA) [136].

We show that large electrodes relatively close to the source (i.e., distances equal or smaller than the size of the electrode itself) require a surface rather than a point electrode modeling approach (Fig. 3.4). This result is comparable to previous findings, which conclude that an insulat-

ing point electrode is only sufficiently accurate within 4 times the electrode radius [136]. The set-ups that were used here represent commonly used ECoG grids [194], where the electrodes are cylinders with a diameter of 4 mm. Considering that the average thickness of grey matter is around 3 mm [199], the distance from the source to ECoG electrodes is in many cases smaller than the diameter of the electrode and therefore it is necessary to model the electrode explicitly.

Thus, when simulating large electrodes near the source, choosing the appropriate electrode model is essential. In Table 2, we show that using a point-electrode approximation largly overestimates the recorded potentials, as compared to any of the more elaborate electrode models. The difference between the disc-electrode approximation and the elaborate electrode models is less pronounced. Therefore the disc-electrode approximation could be considered as a minimally required electrode model when recording close to the source; especially because of its straightforward implementation. A more complete electrode model should be considered if the electrode interface impedance is low to prevent an overestimation of the recorded potential by up to 33%.

In general, we have to consider that no clear consensus has been established yet on exactly how local the signal recorded by ECoG grids is [98, 42]. However, due to the decrease of the potential with distance, the majority of the signal will represent mainly local sources.

To better understand the electrode effect, one should consider that the value recorded by an electrode can be described as the integral over its surface (3.4), or more completely with Robin BCs (3.3) [29, 134, 158]. Thus, the potential given by larger electrodes is the average over an increasingly inhomogeneous potential distribution, resulting in a loss in spatial resolution. When recording close to the source, the potential distribution over the electrode surface is likely to be more inhomogeneous. In contrast, when recording a faraway source, the potential distribution over the electrode surface will be homogeneous.

When including an amplifier input impedance to the electrode model (results not shown), values around 10 MΩ are already sufficiently high, so that there is no difference from the case with a perfectly insulating (infinite impedance) amplifier [135] considered in our calculations.

The shunting effects that cause the potential averaging over the electrode surface only affect the tissue in its proximity (Fig. 3.5). When recording close to the source with a low contact impedance, the potential distribution under the electrode is affected up to the radius of the electrode. Depending on the electrode size and the area that needs to be recorded from, it is thus important to ensure a sufficiently high surface impedance, so that current flow in the underlying external cortical layers is not affected.

We should note that comparing electrode configuration (a) and (b) depict a worst case scenario. Depending on the size of the surface impedance, electrode effects could be less pronounced. However, the surface impedance of the electrodes is not generally measured, and also can require extensive simulations [97]. An optimal surface impedance for a specific electrode setup should thus be computed in order to assure that one can record without affecting the underlying tissue, and also in order to keep the impedance as small as possible to increase the signal-to-noise ratio [110].

As a proof of principle (Study 3), the difference between point electrode and metal electrode recorded potentials generated by a bipole in a realistic head model is visualized on a realistically shaped cortex (Fig. 3.6). The difference between the two electrode types relative to the RMS of the potentials is small for sources at a location further away (a distance of the diameter of the electrode). However, when the source is placed closer the electrode effect becomes more pronounced in the nearby tissue. The potential distribution on the electrode surfaces (Fig. 3.6 A,B) demonstrates the need for a disc-electrode approximation. The recorded potentials using a point-electrode approximation are highly dependent on the position of the electrode midpoint.

Using a more complete electrode model can be important in determining the ideal spatial resolution of electrode grids recording close to the source. Adopting more elaborate source models could also assist in determining optimal grid design for these electrodes. Furthermore, both study 2 and 3 suggest that using the inhomogeneous potential distribution over the electrode surface using a point electrode could lead to significant errors in applications such as source reconstruction. Thus including a more complete electrode model could be necessary to improve source localization errors.

Including an explicit region for the electrode in the volume conductor can also shed light on the effect of a non-bending electrode with respect to the curvature of the brain, which affects the distance between the source and the electrode. With recent advances in high-density ECoG grids, the shunting effects of the electrodes might be aggravated, if, for example, the combined contact surface of the high-density ECoG electrodes covers a relatively large area of the underlying tissue. Which is in accordance with findings in EEG simulation studies [157, 158]. In future work we plan to use the electrode models to create sensitivity maps and receiver operating characteristic for high-density ECoG grids.

3.5 Conclusion

In conclusion, if the distance between an electrode and the source is equal to or smaller than the size of the electrode itself, electrode effects should not be disregarded in simulation studies. In the examples that were presented, typical ECoG electrode sizes of 2 mm radius [194] were used, indicating that modeling studies for these types of grids require a more extensive electrode model. Furthermore, it was shown that with a low electrode contact impedance and nearby sources, the potential distribution of the tissue lying directly under the electrode is affected by the presence of the electrode.

Acknowledgment

This work is part of the perspective programme NeuroCIMT with project number 14906, which is financed by the Dutch Research Council (NWO).

4 Separability of finger somatotopic activity in sensorimotor cortex using high-density ECoG

M Vermaas, TF Oostendorp, R Oostenveld, NF Ramsey, PHE Tiesinga, and MC Piastra
Under revision.

Abstract

Brain-Computer Interfaces (BCIs) controlled by electrocorticography (ECoG) are currently being explored to restore and replace communication in severely paralyzed people. To date, implantable BCIs have mainly focused on the sensorimotor cortex, resulting in a stable albeit slow control by the patients. The performance could be improved by considering more discrete classes of movement to steer the BCI. A promising candidate could be to decode individual finger movements and hand gestures to exploit (attempted) sign language. This requires a deeper understanding of the spatial resolution of the ECoG grid because it depends on activity in smaller regions of the cortex.

Here, we investigated whether simulated somatotopic activity of individual fingers in M1 and S1 can be separated from each other when recording with a high-density ECoG grid. We performed our simulations with FEMfuns, a volume conduction modeling software toolbox based on the finite element method. A realistic head model and ECoG grid was used to construct lead field matrices (LFMs) for somatotopic source patterns representing the fingers in M1 and S1 based on recent fMRI data. Singular value decomposition is used to describe how separable the LFMs of fingers are.

We find high separability values of the somatotopic activity of individual fingers in sensorimotor cortex if the ECoG grid has sufficient coverage of the hand-selective region. Furthermore, due to low signal magnitude of deep sources, minimal separability is found between deep and superficial sources.

In conclusion, we show that sources representing finger activity close to the electrodes and with sufficient grid coverage are separable when using a high-density grid. This approach can be used to estimate the spatial resolution of the recording equipment.

Keywords: Brain-computer interface, Finite element method, ECoG, Singular Value Decomposition, Source separability, Somatotopy, Electrode properties, Forward problem

4.1 Introduction

The development of clinical brain-computer interface (BCI) solutions to restore and replace motor function or communication in severely paralyzed people, has surged in the last decades [15, 38, 194]. Most BCIs are centered around the sensorimotor cortex, because of its direct relation with (attempted or imagined) movement. The sensorimotor cortex consists of the primary motor (M1) and primary sensory (S1) cortex. Both are organized in a predictable order (the somatotopic homunculus), where specific areas control different body parts [149].

In a recent BCI study [194], the somatotopic organization of the sensorimotor cortex was exploited. The BCI-implanted patient accurately controlled a computer typing program by attempting hand grasping movements. This attempted movement was decoded online from electrocorticography (ECoG) signals, where electric potentials are recorded directly from the cortical surface. The BCI proved to be sufficiently reliable for unsupervised home use, albeit with a low typing speed (two letters per minute), which should conceptually be extendable by employing more degrees-of-freedom (i.e., discrete classes of movement).

In particular, the representation of fingers [173, 89] and hand gestures [33, 21, 19] are promising candidates to improve BCIs since they are amenable to decoding from sensorimotor cortex, as shown with Magnetic Resonance Imaging (MRI) [173, 89] or high-density (HD) ECoG [18]. However, using the neuronal activity during finger movements and hand gestures to control a BCI system requires a sufficiently high spatial resolution of the ECoG grid [18, 173]. Since the representation of the different fingers along M1 and S1 covers a cortical surface area of approximately 1 cm^2 [122, 180], standard clinical grid electrodes (1 cm pitch) that are used for long-term implanted BCIs [194, 181] would fail to capture neuronal activity at this spatial scale.

A modeling approach can investigate optimal spacing or placement of electrodes [181, 208] and the sensitivity of the recording electrodes to deep or superficial sources [59]. These studies are centered around volume conduction models to solve the forward problem, i.e., compute the electric potential in the brain given by a known source. Using volume conduction models to find the optimal electrode spacing depends on the source that a researcher wants to distinguish. For example, recording fo-

cal sources would require an electrode grid with many contact points at a close spacing [181]. Rather, it would be valuable to study the limitations of what a particular electrode grid, available to the experimentalist, can record (i.e., is a particular activity pattern of interest distinguishable) and if there is an optimal electrode spacing tailor made for the demands of the experimentalist.

In the present study, we use volume conduction models to quantify the separability of realistic somatotopic activity of individual fingers in M1 and S1 when recording with a HD ECoG grid. Based on literature, the sensorimotor hand area can be decoded using a HD ECoG grid [18, 173]. We assess how separable neuronal activation in individual finger regions is, using the singular value decomposition of the modeled recorded grid potentials (i.e., the lead field matrices, LFM) [81, 193]. The separability measure gives an estimation of whether areas of neural activity can be decoded from a particular recording electrode grid.

Furthermore, the spatial spread (i.e., the cortical tissue that contributes to the recorded signals) of ECoG remains a topic of discussion [98, 113, 42]. Here, we consider the relation between the depth of the sources and the separability of the activity.

Additionally, we address the influence of ECoG electrode properties on the LFM when recording with an ECoG grid on top of the sensorimotor cortex. In [196, 42, 136], it was indeed found that in some cases more detailed electrodes need to be included in ECoG modeling simulations.

4.2 Materials and methods

Anatomical data acquisition

One patient with intractable epilepsy was intracranially implanted with a HD ECoG grid in order to localize the epileptic focus. The HD grid had 64 electrodes with 1 mm exposed surface diameter and 4 mm center-to-center distance (PMT Corporation, Chanhassen, USA). A T1-weighted structural preoperative MRI scan was acquired on a 3T scanner (Philips Achieva, Best, the Netherlands), with an isotropic voxel size of 1 mm. Additionally, a post-operative high-resolution Computed Tomography (CT) scan was acquired to locate the electrodes (Philips Tomoscan SR7000), with voxel sizes of 0.49 mm $\times$ 0.49 mm $\times$ 0.7 mm.

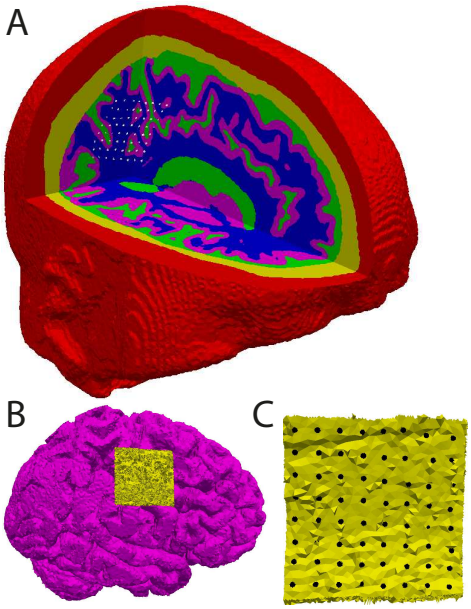

Fig. 4.1: A) Head model with scalp (red), skull (yellow), CSF (green), grey (purple) and white matter (blue) compartments and electrode contact surfaces (white). B) Grey matter with the electrode grid position (yellow). C) The ECoG grid with 8 × 8 electrode contact surfaces (black).

Head model

The final ECoG grid electrode coordinates were calculated using the ALICE procedure [20].

The grey and white matter compartments of the head model were segmented using FreeSurfer (`https://surfer.nmr.mgh.harvard.edu/`). The skull compartment was created by thresholding the CT [140]. Finally, Fieldtrip [144] was used to create the scalp and CSF compartments, and Seg3d [35] was utilized for manual corrections.

After the masks of the five compartments were assembled, a volumetric tetrahedral mesh was created in iso2mesh [48]. The mesh was refined near the electrode coordinates using the Finite Element Method for use-

ful neuroscience simulations [195] (FEMfuns[3]) resulting in ∼6.9 million tetrahedra. The ECoG grid was defined as a layer representing the silicon sheet and 64 surfaces representing the contacts, with an average electrode surface of 0.8 mm^2 (the actual electrode surface was 0.785 mm^2).

Source model

Two source configurations were created (Fig.4.2 1&2), with 10 patches per configuration representing the five digits in M1 and S1. The sources in configuration 1 are partially covered by the electrode grid, while source configuration 2 is positioned directly under the grid. The positions of the patches in source configuration 2 are based on somatotopic maps estimated in [173]. Neuronal sources of each digit were described as synchronously active patches of bipole sources, i.e., dipoles approximated by two monopoles that are separated by 1 mm [12]. The magnitude of all bipoles combined in each patch was normalized to a total of 1 μA. This magnitude was chosen to ensure that the resulting simulated ECoG signals reflect realistic data (i.e., an experimental hand gesture task showed root mean square (RMS) values in the high frequency band of HD-ECoG recordings between 1.5 μV and 4 μV). The distance of the patches along the gyrus representing the somatotopic map, from thumb (d1) to pinky (d5), spans $\sim$ 17 mm, which is in accordance with the literature [122, 170].

Bipole coordinates were calculated by taking vertices on the grey matter surface that were identified as M1 and S1 based on visual inspection (i.e., pre- and post-central gyrus and the central sulcus) and are visualized in Fig.4.2. Each vertex coordinate was projected 1.5 mm into the brain along the normal of the grey matter surface. The monopoles representing the sink and source of the bipoles were oriented radially with respect to the nearest grey matter surface facet. Only bipoles that were located within the brain and at a distance of 0.5 mm from the grey matter surface were used in the calculations. This resulted in a total of 1597 and 1037 bipoles for all M1 and S1 patches in source configuration 1 and 2, respectively.

Additionally, each of the 10 patches of source configuration 2 were split in superficial and deep regions, i.e., at the gyrus or at the sulcus. The

[3] https://github.com/meronvermaas/FEMfuns

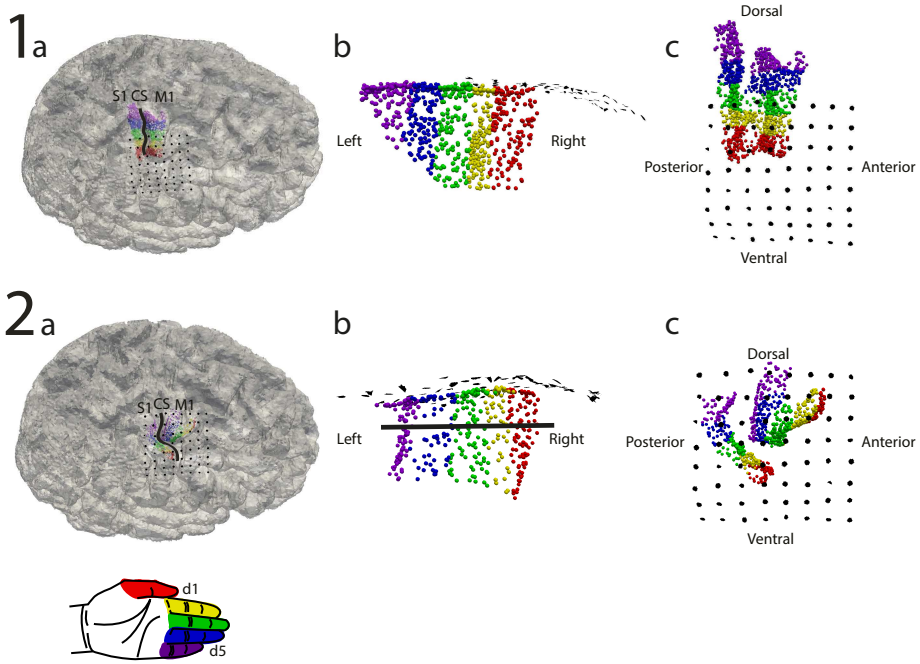

Fig. 4.2: a) Grey matter with the electrode contact surfaces (black) and the source patches in configuration 1 (top) and 2 (bottom). The central sulcus (CS, black line) separates M1 (anterior to the CS) and S1 (posterior to the CS). b) The source patches (each finger colored differently) curved along S1 are displayed in a coronal slice, M1 sources are not shown for clarity at this angle. In 2b a black line indicates the distinction between deep and superficial patch activity. c) A horizontal view with respect to the grid, showing the position of the finger patches under the grid. The electrode contact surfaces are shown in black. The color coding of the digits is displayed in the bottom.

average distance of the bipoles in the superficial and deep patches to any electrode is 2.7 mm and 8.1 mm, respectively.

Electrode model

We previously showed that when the distance between an electrode and the source is equal to or smaller than the size of the electrode, electrode effects cannot be disregarded [196]. To determine which electrode model is required in this particular geometry, we considered four electrode configurations:

a) point-electrode approximation, without an insulating layer;
b) disc-electrode approximation, with an insulating layer;
c) metal electrode, without an insulating layer;
d) metal electrode, with an insulating layer.

In electrode model (a) the potential at the midpoint of each electrode was computed, assuming skull where the electrodes were positioned. In electrode model (b) a perfectly insulating layer ($\sigma = 0$ S/m) was included, representing the silicon sheet, and the electrode potentials were evaluated as the average over the electrode surface. Electrode model (c) had a metal electrode with a surface conductance of 10^5 S/m^2 [97, 195, 196]. The insulating layer representing the silicon sheet was not included. Finally, electrode model (d) is the same as (c), but also includes the insulating layer. The point-electrode approximation with a silicon grid and the disc-electrode approximation without a silicon grid have been omitted here.

FEM simulations

The ECoG forward problem was solved by applying a Lagrangian FEM [200] to simulate the electric potential generated in the volume conductor by a source representing finger activity. The FEM simulations were performed using the open-source forward modeling implementation in FEMfuns [195], which is built upon the open-source software FEniCS [3, 117].

The boundary value problem was solved with homogeneous Neumann boundary conditions (BCs) on the outer surface of the head model. Tissue properties were resistive with conductivities, σ, of the grey and white matter [108], CSF [54], skull [162] and scalp [160] being 0.28, 0.25, 1.59, $3.5{\cdot}10^{-3}$ and 0.17 S/m, respectively. The surface conductance of the electrode contacts was applied using a Robin BC [97, 195].

The LFM (channels $\times$ patches, i.e., 64 $\times$ 10) was assembled for each electrode model and for each source configuration, and a common average

reference was applied. The difference between the LFMs of the electrode models was visually inspected to determine the effect of the ECoG grid on the simulated potentials.

Separability of recorded activity

If the maximum potential of the LFM of a finger patch was above noise level (1 μV, taken from RMS values in the high frequency band of HD-ECoG recordings during rest), this patch was further analyzed on the separability it has from other sources. The LFM of pairs of patches ($\boldsymbol{A}$, with size 2×64) above noise level was decomposed using singular value decomposition (SVD) into a product of 3 matrices:

$$\boldsymbol{A} = \boldsymbol{U}\boldsymbol{\Sigma}\boldsymbol{V}^T \tag{4.1}$$

where $\boldsymbol{U}$ and $\boldsymbol{V}$ are orthonormal matrices and $\boldsymbol{\Sigma}$ is a diagonal matrix. The diagonal entries of $\boldsymbol{\Sigma}$, i.e., the singular values ($\sigma_1 > \sigma_2$), are arranged in decreasing order. The separability index (SI), i.e., the ratio between the singular values, was computed for each pairwise SVD:

$$SI = \frac{\sigma_2}{\sigma_1} \tag{4.2}$$

as a measure for how separable the pair of patches is. The magnitude of a singular value is indicative of its importance in explaining the data. More precisely, the square of a singular value is proportional to the variance explained by it.

A SI close to one indicates that both the first and second component of the SVD contain a large amount of signal information; thus the two patches are separable. If the SI is close to zero, the first component is sufficient to describe the signal information of both patches, indicating they are not separable.

4.3 Results

Electrode model simulations

The LFMs cooresponding to the four electrode model simulations (a-d) are visualized in Fig.4.3 for a single exemplary source patch, representing M1 thumb activity (Fig.4.3E). The LFM during the activation of the

patch, when using the different electrode models (a-d), is displayed with a 2D Delaunay triangulation (Fig.4.3A-D). A dipolar distribution can be observed and related to the dipoles along the gyrus (for a clear view of the source positions, see the red sources in Fig.4.2B).

The potential distributions on the electrode grid are similar regardless the electrode model (a-d) that is used in the simulation. The average percent difference of all patches and electrodes (i.e., the 64×10 LFM) between the least extensive electrode model (a) and the most extensive electrode model (d) is 0.23%, with a standard deviation of 3.2%.

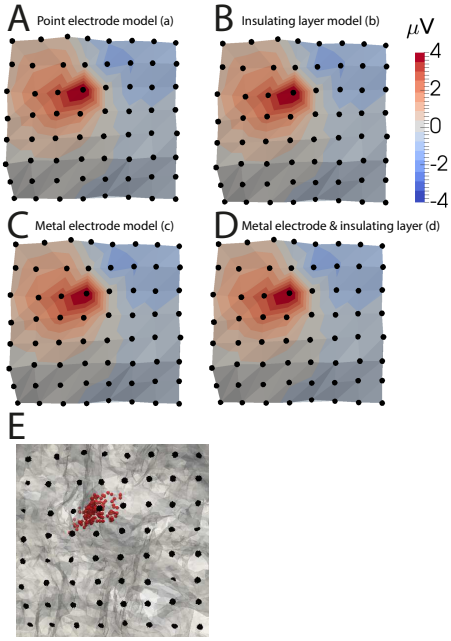

Fig. 4.3: A-D) The constructed 2D Delaunay triangulation from the LFM of one patch in M1 using the four different electrode model (a-d). The electrode positions are displayed in black. E) Position of the source patch (red) in M1 and the electrode positions (black).

Digit separability in M1 and S1

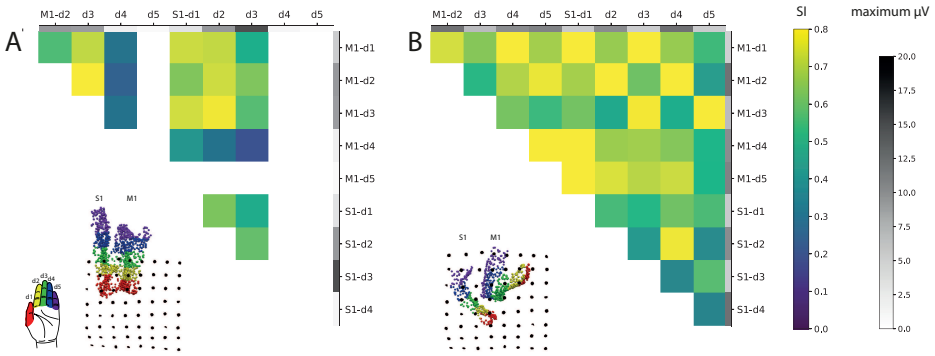

Fig. 4.4: SVD of the LFMs of pairs of the 5 patches corresponding with thumb (d1) to pinky (d5) for M1 and S1 in source configuration 1 (A) and source configuration 2 (B). The SI (Eq.4.2) was computed for patches above noise level. The maximum potential of the LFM for each source patch is displayed in gray along the x and y-axis. The position of the source patches and color coding of the digits is shown in the bottom left corners of A) and B).

A pairwise SVD for all patch combinations was computed and the SI (Eq.4.2) was visualized (Fig.4.4) for patches that are above noise level. The maximum LFM potential is displayed around the edges in gray, where a darker hue in combination with a high SI indicates the sources are both measurable and recordable.

In source configuration 1 (Fig.4.4A), the SIs of patches representing M1, digit 1-4, and S1, digit 1-3, are visible, since only their LFMs are above noise level. The SI of digits in S1 with other digits in S1 is lower than the SIs of source pairs including M1 digits. Furthermore, the SI of M1-d4 is lower compared with the other SIs, which is related to the smaller maximum potential in this source patch compared with the other patches.

Source configuration 2 (Fig.4.4B) shows an improvement in terms of patches that are above noise level, with almost all digits visible in the SI matrix. Furthermore, the SIs are high, with many equal to or bigger than

0.7 (green and yellow). The checkerboard pattern observed for SI pairs of M1 d1-d3 with the other digits is related to the maximum potentials that alternate between larger and smaller magnitudes.

Deep and superficial source depth separability

A distinction between deep and superficial (Fig. 4.2, black division line in 2b) was considered only in source configuration 2, since the signal magnitude of all source patches was higher. However, the signal magnitude of the deep sources of both M1 and S1 was close to or below noise level for all digits. Thus, rather than inspecting the SIs, the maximum recorded potentials are displayed (Fig. 4.5). In addition, the spatial resolution of the electrode grid was decreased (4 electrodes, comparable to a clinical grid [194]) and increased (maximum of 1215 electrodes) by adding nodal points on the grid surface.

The maximum potential of the LFM of deep sources of M1 (gray) and S1 (yellow) is close to the noise threshold (red line) (Fig. 4.5A). Increasing the spatial density of the electrodes has no effect on the magnitude of the simulated potentials of deep sources.

The maximum potentials of the superficial sources are above the noise threshold (Fig. 4.5B). Different from the deep sources, increasing the spatial density of the electrodes for the superficial sources does affect the maximum potential in most cases (Fig. 4.5B). The number of electrodes at which the maximum LFM potential converges is different for each patch, but around 200 contact points for most source patches. However, the effect of increasing the electrode spacing on the SI is limited, with mean values of 0.35, 0.59 and 0.65 for 4, 64 and 204 electrodes, respectively. Increasing the number of electrodes further did not increase the mean SI.

4.4 Discussion

In this study we have shown the separability of the somatotopic activity of individual fingers in sensorimotor cortex using a HD ECoG grid.

Grid coverage is crucial for finger separability. If the sources representing the fingers in M1 and S1 were covered by the ECoG grid (Fig.4.4), the recorded potentials were above noise threshold showing high SIs (Eq.4.2). Only sources underneath the grid were separable, with source configura-

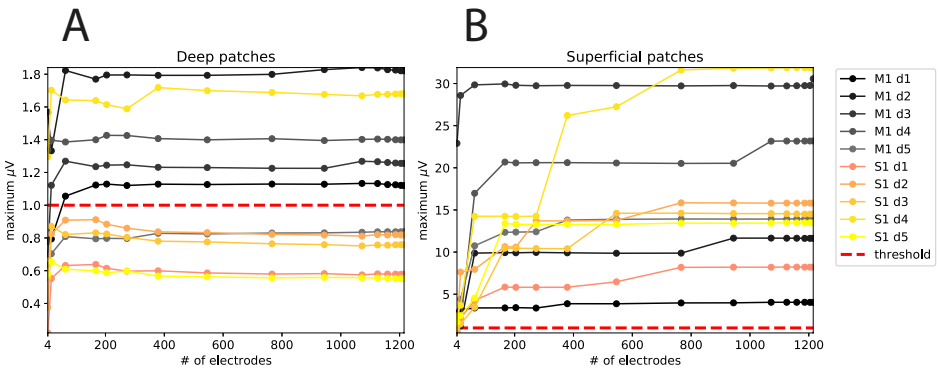

Fig. 4.5: A) The maximum potential at the LFM of the deep sources of digits in M1 (gray) and S1 (yellow) and the noise threshold (red) plotted against number of electrodes. B) The maximum potential at the LFM of superficial sources for all digits plotted against number of electrodes.

tion 1 (partial grid coverage) showing a limited amount of separable fingers (Fig.4.4A) and source configuration 2 (full grid coverage) allowing for all fingers to be separated (Fig.4.4B). Our findings are in line with previous studies which show that grid coverage is essential in source localization [81] or when decoding hand gestures [19] using ECoG recordings.

Deep sources are not separable. We found minimal separability of deep sources (in the central sulcus, faraway from the electrode grid) from superficial sources (at the pre- and post central gyrus, close to the electrode grid). Recently, the spatial spread of ECoG was shown to be fairly local (distances of 3 mm) [42]. Indeed, the superficial sources clearly dominate the signal (Fig.4.5), while sources in the sulcus describe only a minor portion of the recorded signal that is often below noise threshold, because of the large distance between the source and the electrodes.

Increasing the number of electrodes did not result in an increased maximum signal at any electrode for deep sources (Fig.4.5A). This implies that adding more electrodes at a closer spacing does not increase the distance between the deep sources and the electrodes. An increased number of electrodes did improve the maximum signal at any electrode for the superficial sources (Fig.4.5B). The maximum signal converges once an electrode is added directly above (i.e., is as close as possible) the source patch. Us-

ing only four electrodes with a larger spacing, comparable to clinical grid electrodes [194], resulted in a large decrease in both the number of source patches above noise threshold and the SIs. Increasing the number of electrodes beyond 64 only slightly improved the separability of the underlying sources.

Surprisingly, the spacing of the 64 electrode grid was 4 mm, while the optimal spacing for ECoG electrodes has been estimated to be around 1.4 mm [50, 181]. Assuming this electrode spacing for the ECoG grid used in this study would result in 400 contact points. However, this number of electrodes is not distinctly optimal in our simulations (i.e., the spacing where the magnitude of the recorded signal or the SI converges). The difference between these results can partially be attributed to the distributed source model that was used here, while the authors in [181] assume a single dipole. Furthermore, we consider the separability of sources recorded at the channels, while [181] determine the optimal grid spacing based on the attenuation of the signal. Thus, our approach estimates if a particular electrode spacing is sufficient to distinguish a particular source (distribution) of interest.

A valuable future step would involve relating the SI, as an estimation of which fingers can be decoded, to experimental ECoG data during a finger flexion-extension task [173]. In addition, there is limited research addressing to what extent ECoG can be used to localize the underlying sources [81, 193]. The approach presented in this study could be used to optimize the constraints in the source localization algorithm. A limitation of this study concerns the uncertainty in the noise thresholding for each source patch. Both the noise threshold and the simulated recorded potentials are simplified representations of realistic data. However, the noise level and source magnitude can be adjusted based on the brain region of interest. Additionally, by inspecting both the SI and the maximum LFM potential (Fig.4.4, outer gray bars), areas that are more and less likely to be separated can be estimated. A further limitation concerns that the results were obtained assuming homogeneous, isotropic tissue conductivity, which can largely affect the recorded potentials.

In addition, we showed that the effect of ECoG electrode properties on the recorded signal was small (Fig.4.3). This is in accordance with our previous findings [196]. There, we showed that ECoG electrode properties

are expected to affect the recorded potential if the distance between an electrode and the source is equal to or smaller than the size of the electrode itself. Indeed, in our model, the sources are positioned 1.5 mm under the gray matter surface and their distance to the electrode grid generally is larger than the diameter of the electrodes (1 mm).

4.5 Conclusion

In conclusion, this study shows that sources representing finger activity in sensorimotor cortex are separable when using a HD ECoG grid. In order to ensure recorded signals that are above noise level, it is essential that the grid fully covers the sources of interest. Furthermore, deep sources generally produce signals below noise level on an ECoG grid, irrespective of the spatial resolution of the grid. Finally, the presented separability measure can be used to estimate what the effective spatial resolution of the recording grid is, while taking into account the neural source distribution.

Acknowledgment

This work is part of the perspective programme NeuroCIMT with project number 14906, which is financed by the Dutch Research Council (NWO).

5 General discussion

5.1 Main summary

Electric activity generated by neuronal processes in the brain can be recorded, for example at the surface of the brain (electrocorticography, ECoG). Using ECoG, neuronal activity at several millimeters from the recording contact can be picked up. However, there is no consensus yet on the precise size of the region contributing to the recorded signal [115, 13, 119, 42].

The main goal of the research described in this thesis is to better understand and advance the electrophysiological recording efficiency and selectivity in terms of electrode properties and their spatial configuration, in particular in ECoG.

ECoG is used clinically for seizure localization in epilepsy patients. Furthermore, ECoG signals can be used in a brain-computer interface (BCI), where the activity in the central nervous system is utilized to control a neuroprosthetic device (e.g., a prosthetic limb or a computer program). The temporal stability of mesoscopic ECoG grids has been invoked to argue that it is the preferred recording technique for BCIs, as compared to microscopic and macroscopic scale measurements [194, 31], this view has not been widely established or rigorously validated. Furthermore, prior efforts to understand and improve the recording quality of mesoscopic measurements via a computational approach are sparse [181]. Here we will summarize and discuss the results of the studies we performed, as well as describe prospects and desirable future steps.

We first developed new suite of modeling tools, which were used to further investigate how to perform volume conduction simulations that take the presence of electrodes and the frequency components of the signal into account, in particular in the case of ECoG. Modeling approaches have been used predominantly to investigate and develop microscopic and macroscopic electrode designs [165, 141, 169, 86]. In our first study (**chapter 2**), we presented the first open-source, easy-to-use and flexible pipeline (named "Finite Element Method for useful neuroscience simulations", FEMfuns), allowing for the simulation of multiple material compartments in volume conductor models. We created FEM scripts which allow neuro-

scientists to use resistive, capacitive and dispersive tissue properties and different types of electrodes [195].

We investigated the frequency dependency of the Poisson equation, which includes non-linear effects, and we did not find major effects for recording electrodes. It is known from literature that at low driving potentials the electrode-electrolyte interface impedance is generally linear. For high driving potentials (often during stimulation) nonlinear characteristics may emerge [175, 164, 49, 29]. Thus, we did not find major nonlinear effects for recording electrodes with small sources representing brain activity. However, when larger electrodes are used, interface effects due to the recording electrode can be observed [143, 158].

Although other open-source toolboxes for solving forward problems with FEM are available [144, 204, 138, 142], neither the frequency dependent properties of biological tissue nor the electric properties of the electrodes are incorporated in these packages. In addition, the `Python` code of our pipeline can be easily adjusted and extended.

The main limitation of the pipeline concerns mesh generation, which currently needs to be done in external software such as FSL [93] or gmsh [57]. Furthermore, currently only tetrahedral mesh elements can be used since FEniCS [3], the general FEM toolbox around which FEMfuns is centered, only supports these. These shortcomings will be addressed in the future steps (Section 5.2).

Next, in **chapter 3**, the FEMfuns pipeline was used to investigate the influence of the presence of electrodes on the potential distribution on the electrode surface and in the underlying tissue. Few studies have considered the effect of the electrode [143, 136, 158] and only EEG and microelectrodes were considered.

Therefore, we investigated ECoG grids and showed that large electrodes relatively close to the source (i.e. distances equal or smaller than the size of the electrode itself) need to be modeled by a surface rather than a point electrode modeling approach. This indicates that especially simulations of clinical ECoG grids with common sizes of 2 mm radius would benefit from using a more extensive electrode model.

Furthermore, we showed that, with a low electrode contact impedance and nearby neural activity, the potential distribution of the tissue lying directly under the electrode is affected by the presence of the electrode

(up to the radius of the electrode). Therefore, it is important to ensure a sufficiently high electrode surface impedance, so that current flow in the underlying cortical layers is not affected.

The electrode surface impedance is generally not measured, because this is a challenge in itself [174, 97]. By choosing a very low contact impedance in our simulations, the worst case scenario was depicted. For any electrode set-up it may be useful to estimate an optimal surface impedance such that recordings can be performed without affecting the underlying tissue, while keeping the impedance as small as possible to increase the signal-to-noise ratio [110].

As discussed in the introduction (1.2), choosing the desired recording electrode type for long-term BCI systems requires careful consideration. By knowing the limitations of the available recording electrodes, experimentalists at medical centers could improve the BCI system. In the final study (**chapter 4**), we utilized the FEMfuns pipeline to estimate the effective spatial resolution of ECoG grids (i.e., whether particular electrical potentials are distinguishable by the grid). Specifically, a quantification was made of the separability of realistic somatotopic activity of individual fingers in sensorimotor cortex when recording with an HD ECoG grid implanted in an epileptic patient at the Utrecht Medical Center.

We showed that superficial sources representing finger activity in sensorimotor cortex are separable when using an HD ECoG grid that fully covers the sources of interest. Furthermore, deep sources generally produce signals below noise level on an ECoG grid, irrespective of the spatial resolution of the grid. In contrast, for superficial sources, decreasing the electrode spacing improves the separability. Finally, the separability measure we used can be used more generally to estimate the effective spatial resolution of any recording grid, while taking into account a neural source distribution of interest. This approach could be adapted for model-based optimization to design more efficient electrode grids.

A limiting factor in this approach is the uncertainty in choosing realistic noise values and a source distribution that represents a certain behavior (e.g., a hand grasping movement [194]). However, since we adjusted the noise level and source magnitude according to a realistic ballpark estimate, it gives an approximation of those areas that are more and less likely to be

separated by the electrode grid. Possible improvements in creating realistic noise levels and source distributions will be discussed in section 5.2.

5.2 Future research

This thesis aims to increase our understanding of electrophysiological recording electrodes in order to improve their efficiency in neuroprosthetics applications. A simulation of the recorded grid potentials due to the spatiotemporal electrical activity patterns generated by neural activity can inform a neuroscientist how to, for example, optimize grid design for electric stimulation mapping in epileptic patients or BCI systems in locked-in patients, including the exploration of alternative electrode properties.

Creating an easy-to-use approach for neuroscientists to perform simulations and determine the optimal recording grid for a particular neural signal still is an unfulfilled opportunity for further advancement. To achieve accurate models it is necessary to simulate the non-homogeneous and anisotropic tissue properties, the electrode properties and the neural activity.

The pipeline presented in **chapter 2** allows for these types of simulations. It was applied to study recording and stimulating electrodes (**chapter 3**), and for estimations of the selectivity of a grid (**chapter 4**). However, several manual steps are still required, decreasing the practicality of the pipeline for non-expert users. Integrating the FEMfuns source code in a versatile and widely used toolbox, such as FieldTrip [144] or Brainstorm [184], would drastically improve its usability as well as reach the part of the scientific community that could benefit from the pipeline the most.

Since mesh generation is not included in FEMfuns (several manual steps and external software packages are needed), integrating FEMfuns in an established toolbox (with meshing routines already present) would simplify the use of the pipeline. Furthermore, the data analysis and source reconstruction algorithms present in, e.g., the FieldTrip toolbox can be combined with the forward solutions generated in our FEMfuns pipeline. Indeed, FEMfuns will be implemented in FieldTrip as part of the "IntoTheBrain" project, which we recently started.

Another possible improvement of FEMfuns involves automatic generation of electrode grid models in the mesh. Generally electrodes are not

explicitly included in the mesh, but represented by a point. Automated segmentation, placement and tesselation of an electrode grid could be developed based on a recent publication [88]. The authors in [88] created scripts that allow the user to automatically position EEG or intracranial electrodes with various shapes in a mesh, or by simply providing the electrode coordinates. Building upon this, routines for positioning stereo EEG, ECoG and other types of (depth) electrodes could be developed in FEMfuns.

In **chapter 3** we investigated the effects of recording electrodes on the forward solution. However, we did not rigorously investigate the same for stimulating electrodes. While these electrodes have been considered in the literature to some degree [23, 29, 97, 65, 86], a full overview of which types of stimulating electrodes require which electrode model has not been published yet to our knowledge.

The results and electrode model approach introduced in **chapter 3** could additionally be employed to design and optimize the electrode contact impedance for parameters such as the signal-to-noise ratio. The effective contact impedance may for example be related to different electrode shapes such as a disc, a pad or a ring. With FEMfuns, electrodes with a variety of sizes, shapes and materials (each influencing the contact impedance and SNR) can be simulated to study their effects in neural recording and stimulation set-ups.

As already discussed in section 5, the electrode impedance generally is not measured, since it is challenging of its own accord [174, 97]. Rather than an extensive experimental assessment of the electrode impedance [111, 172], a modeling approach can be employed. FEMfuns could be extended to allow for an optimization procedure that estimates the electrode impedance by combining simulations with a limited amount of experimental data (e.g., comparable to the approach in [97]).

The pipeline presented in **chapter 2** includes the possibility of using capacitive properties of the tissue and the electrode interface [195]. A test-case with recording and stimulating microelectrodes was presented, however, we did not further explore the effect of frequency on the current density distributions. These types of electrode effects have mainly been considered in stimulation studies [165, 24, 29, 65], because in most

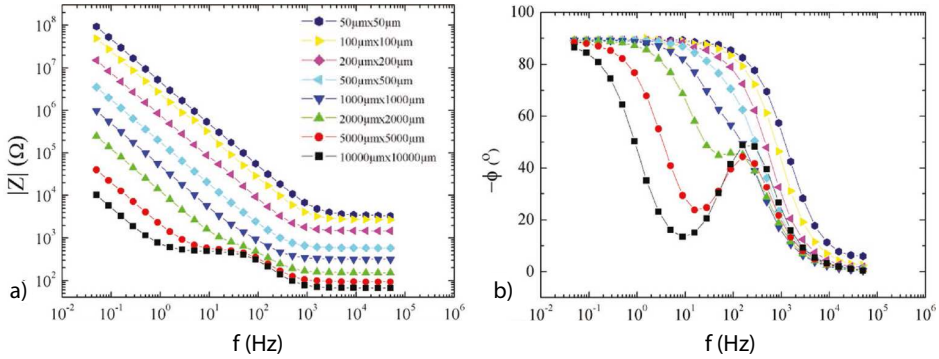

Fig. 5.1: Bode magnitude (| Z |) and phase (ϕ) spectra (a and b, respectively) of gold electrodes with various sizes placed on top of a layer of tissue. The electrodes with a larger surface area (i.e., a smaller impedance) show a plateau in the magnitude plot (a), and a peak in the phase plot (b) due to the capacitive tissue layer. Reprinted from [105].

cases resistive currents are dominant in the recording electrode interface impedance.

However, a recent study shows the importance of the ratio between the impedance of tissue and electrode (Fig. 5.1) to achieve efficient recording sensitivity [105]. In Fig. 5.1a, due to the R-C circuit of the electrode a resistive behavior can be observed at high frequencies and a capacitive region at low frequencies (for electrodes smaller than 2 mm x 2 mm). For these electrode sizes a simple scaling is sufficient to find the magnitude of the impedance. However, for larger electrodes, the presence of a capacitive tissue membrane becomes apparent from both phase and impedance values (10^2-10^3 Hz). These effects are mostly related to the ratio between the tissue and electrode impedance [105]. Thus, extending the findings in **chapter 3** to include capacitive electrode and tissue properties would be a useful addition to the current literature.

In **chapter 4** we compared the optimal electrode spacing used in our distributed source model with the single dipole model in [181]. While a separability measure allows the user to estimate the effective resolution of the grid, this estimation is highly dependent on the activity pattern that

is used. Thus these modeling approaches require careful consideration in choosing the sources and their dynamics.

Deciding the amount of detail required in a source model, in relation to the electrode properties, is not trivial. Generally single current dipoles are sufficient source approximations to produce accurate simulations of recorded EEG and MEG signals [133]. Some studies consider more complex electric sources by using simulated neuron geometry and network activity to describe MEG and EEG activity patterns (e.g., [178, 133]). However, these types of sources typically are not adequate for smaller electrodes recording closer to the electrical source, such as ECoG [133].

FEMfuns can be used to better understand the neural origin of ECoG signals by studying the contributions of neuronal sources modeled at different spatial resolutions on the recorded potentials. Specifically, it can be used to give an estimation of the resolution at which sources can be distinguished depending on the electrode properties (the contact surface and impedance). Subsequently this would indicate what type of sources are suited for a particular recording grid in future simulation studies.

Many tools to simulate the electrical patterns of neural activity more accurately are widely available (e.g., NEURON [82], BRIAN [62], NEST [46], LFPy [70]). For example, NEURON can be used to create a multicompartment model of the laminar neocortical architecture to simulate the sources of human MEG signals [178].

Additionally, the calculated dynamic activity of neurons can be used in a forward modeling scheme and can be used to estimate when the capacitive part of the tissue impedance becomes dominant in the simulation (Fig. 5.1). This type of approach has been applied in a volume conduction study with a detailed thalamocortical source model to calculate the potentials recorded by microelectrodes [136]. Computational models of brain circuitry are widely accessible and can be efficiently retrieved (e.g., `https://senselab.med.yale.edu/modeldb/` or `https://www.opensourcebrain.org/`) and used as the building block for more detailed volume conduction simulations.

In a hybrid modeling scheme, detailed multicompartment neuronal models could be used to calculate the electrical sources used in FEMfuns. The findings in **chapter 4** could be extended and single current dipoles, distributed dipoles and a realistic laminar neocortical neuron as

a source model could be compared. Furthermore, we could calculate the separability of sources in the different layers of the gray matter and estimate whether, and with which electrode spacing, these laminar sources can be decoded. Recent findings indeed suggest the anisotropic properties across cortical depth can be relevant in the design of intracortical neuroprostheses [189].

To validate the modeling approaches, the simulation results need to be matched with experimental data. This is a complex problem that can be tackled with a wide variety of approaches (e.g., [40, 95, 64]). Validation of volume conduction models can, for example, be tackled by using both stimulating electrodes and recording electrodes in an experimental set-up (e.g., [97]). The electric potentials at the stimulating and recording electrode are known and can be compared with the simulated recorded potentials. Using this approach, inferences can be made about, for example, the spatial extent of the electrical signals, the tissue conductivity and the electrode impedance.

Furthermore, as an extension of **chapter 4**, the simulated separability of fingers could be related to experimental ECoG recordings during a finger flexion-extension task. The accuracy of the separability measure would be computed using different types of electrodes and tissue properties, as well as a variable number of compartments in the volume conductor. Next, the accuracy of the decoded ECoG recordings during the finger movements can be related to the simulated separability measures. This assists in describing what the least complex model with sufficient precision is.

The validation and testing of forward solutions can also be approached using source localization methods, whose accuracy is influenced by the accuracy of the forward solutions. While many advancements are done to reconstruct sources from EEG and MEG data, ECoG signals are generally rather studied at a sensor level. A source localization is not attempted because of the limited coverage of the grid and the electrodes being close to the neuronal sources [190].

Many source reconstruction methods and algorithms have been described, but, in both EEG and ECoG, tuning the multitude of necessary parameters and deciding the optimal algorithm is not straightforward [129]. Especially source localization of ECoG recordings is not well established, and has primarily focused on epileptic seizure activity [53, 210, 34].

Currently, only a handful of studies have considered the advantages and limitations of source reconstruction methods of ECoG recordings [146, 81, 187]. However, many factors still require further research, such as the types of sources (e.g., distributed vs localized), ECoG noise levels and regularization parameters.

Finally, as a continuation of the separability measure (**chapter 4**), forward solutions generated using FEMfuns can be applied to perform source reconstruction on ECoG recordings during a finger flexion-extension task. We anticipate that the reconstructed sources of each finger would allow us to construct a somatotopic map. These results can be compared with the hand somatotopic map generated using fMRI [173], serving as a ground truth.

This thesis shows that FEMFuns is a useful tool in modeling and interpreting ECoG signals and can be used for calculated electrode design and efficient ECoG recordings. Furthermore, it can be applied to other research questions as well. We have recently started the IntoTheBrain project that aims to make this tool easily available for researchers whose research involves recording bio-electric signals.

Bibliography

[1] Dayo O Adewole, Mijail D Serruya, James P Harris, Justin C Burrell, Dmitriy Petrov, H Isaac Chen, John A Wolf, and D Kacy Cullen. The evolution of neuroprosthetic interfaces. *Critical Reviews in Biomedical Engineering*, 44(1-2), 2016.

[2] Gabriella Airenti. The place of development in the history of Psychology and Cognitive Science. *Frontiers in psychology*, 10:895, 2019.

[3] Martin Alnæs, Jan Blechta, Johan Hake, August Johansson, Benjamin Kehlet, Anders Logg, Chris Richardson, Johannes Ring, Marie E Rognes, and Garth N Wells. The FEniCS project version 1.5. *Archive of Numerical Software*, 3(100):9–23, 2015.

[4] Saber Amdouni, Patrick Hild, Vanessa Lleras, Maher Moakher, and Yves Renard. A stabilized Lagrange multiplier method for the enriched finite-element approximation of contact problems of cracked elastic bodies. *ESAIM: Mathematical Modelling and Numerical Analysis*, 46(4):813–839, 2012.

[5] Marios Antonakakis, Sophie Schrader, Ümit Aydin, Asad Khan, Joachim Gross, Michalis Zervakis, Stefan Rampp, and Carsten H Wolters. Inter-subject variability of skull conductivity and thickness in calibrated realistic head models. *Neuroimage*, 223:117353, 2020.

[6] Tonio Ball, Markus Kern, Isabella Mutschler, Ad Aertsen, and Andreas Schulze-Bonhage. Signal quality of simultaneously recorded invasive and non-invasive EEG. *Neuroimage*, 46(3):708–716, 2009.

[7] Martin Bauer, Sampsa Pursiainen, Johannes Vorwerk, Harald Köstler, and Carsten H Wolters. Comparison study for Whitney (Raviart–Thomas)-type source models in finite-element-method-based EEG forward modeling. *IEEE Transactions on Biomedical Engineering*, 62(11):2648–2656, 2015.

[8] Mark Bear, Barry Connors, and Michael A Paradiso. *Neuroscience: Exploring the brain*. Jones & Bartlett Learning, LLC, 2001.

[9] John Bechhoefer. Kramers–Kronig, Bode, and the meaning of zero. *American Journal of Physics*, 79(10):1053–1059, 2011.

[10] Claude Bédard and Alain Destexhe. Is the Extracellular Impedance High and Non-resistive in Cerebral Cortex?, 2017.

[11] Claude Bédard and Alain Destexhe. Kramers-Kronig relations and the properties of conductivity and permittivity in heterogeneous media. *arXiv preprint arXiv:1801.00461*, 2018.

[12] John M Bekkers. Pyramidal neurons. *Current biology*, 21(24):R975, 2011.

[13] P. Berens, G.A. Keliris, A.S. Ecker, N.K. Logothetis, and A.S. Tolias. Comparing the feature selectivity of the gamma-band of the local field potential and the underlying spiking activity in primate visual cortex. *Frontiers in systems neuroscience*, 2, 2008.

[14] Hans Berger. Über das elektroenkephalogramm des menschen. *Archiv für psychiatrie und nervenkrankheiten*, 87(1):527–570, 1929.

[15] Niels Birbaumer, Nimr Ghanayim, Thilo Hinterberger, Iver Iversen, Boris Kotchoubey, Andrea Kübler, Juri Perelmouter, Edward Taub, and Herta Flor. A spelling device for the paralysed. *Nature*, 398(6725):297–298, 1999.

[16] Timothy Blakely, Kai J Miller, Rajesh PN Rao, Mark D Holmes, and Jeffrey G Ojemann. Localization and classification of phonemes using high spatial resolution electrocorticography (ECoG) grids. In *2008 30th Annual International Conference of the IEEE Engineering in Medicine and Biology Society*, pages 4964–4967. IEEE, 2008.

[17] Blender Online Community. *Blender - a 3D modelling and rendering package*. Blender Foundation, Blender Institute, Amsterdam, 2016.

[18] Mariana P Branco, Lisanne M de Boer, Nick F Ramsey, and Mariska J Vansteensel. Encoding of kinetic and kinematic movement parameters in the sensorimotor cortex: A Brain-Computer Interface perspective. *European Journal of Neuroscience*, 50(5):2755–2772, 2019.

[19] Mariana P Branco, Zachary V Freudenburg, Erik J Aarnoutse, Martin G Bleichner, Mariska J Vansteensel, and Nick F Ramsey. Decoding hand gestures from primary somatosensory cortex using high-density ECoG. *NeuroImage*, 147:130–142, 2017.

[20] Mariana P Branco, Anna Gaglianese, Daniel R Glen, Dora Hermes, Ziad S Saad, Natalia Petridou, and Nick F Ramsey. ALICE: A tool for automatic localization of intra-cranial electrodes for clinical

and high-density grids. *Journal of neuroscience methods*, 301:43–51, 2018.

[21] Mark LCM Bruurmijn, Isabelle PL Pereboom, Mariska J Vansteensel, Mathijs AH Raemaekers, and Nick F Ramsey. Preservation of hand movement representation in the sensorimotor areas of amputees. *Brain*, 140(12):3166–3178, 2017.

[22] Alessio Paolo Buccino, Miroslav Kuchta, Karoline Horgmo Jæger, Torbjørn Vefferstad Ness, Pierre Berthet, Kent-Andre Mardal, Gert Cauwenberghs, and Aslak Tveito. How does the presence of neural probes affect extracellular potentials? *Journal of neural engineering*, 16(2):026030, 2019.

[23] Christopher R Butson, Scott E Cooper, Jaimie M Henderson, and Cameron C McIntyre. Patient-specific analysis of the volume of tissue activated during deep brain stimulation. *Neuroimage*, 34(2):661–670, 2007.

[24] Christopher R Butson and Cameron C McIntyre. Tissue and electrode capacitance reduce neural activation volumes during deep brain stimulation. *Clinical neurophysiology*, 116(10):2490–2500, 2005.

[25] György Buzsáki. Large-scale recording of neuronal ensembles. *Nature neuroscience*, 7(5):446–451, 2004.

[26] György Buzsáki, Costas A Anastassiou, and Christof Koch. The origin of extracellular fields and currents - EEG, ECoG, LFP and spikes. *Nature Reviews Neuroscience*, 13(6):407–420, 2012.

[27] Ramon Cajal. Histologie du systeme nerveux de l'homme et des vertebras. *Paris: Maloine*, 2, 1904.

[28] Luis A Camuñas-Mesa and Rodrigo Quian Quiroga. A detailed and fast model of extracellular recordings. *Neural computation*, 25(5):1191–1212, 2013.

[29] Donald R Cantrell, Samsoon Inayat, Allen Taflove, Rodney S Ruoff, and John B Troy. Incorporation of the electrode–electrolyte interface into finite-element models of metal microelectrodes. *Journal of neural engineering*, 5(1):54, 2007.

[30] Richard Caton. Electrical currents of the brain. *The Journal of Nervous and Mental Disease*, 2(4):610, 1875.

[31] Zenas C Chao, Yasuo Nagasaka, and Naotaka Fujii. Long-term asynchronous decoding of arm motion using electrocorticographic signals in monkeys. *Frontiers in neuroengineering*, 3, 2010.

[32] John K Chapin, Karen A Moxon, Ronald S Markowitz, and Miguel AL Nicolelis. Real-time control of a robot arm using simultaneously recorded neurons in the motor cortex. *Nature neuroscience*, 2(7):664–670, 1999.

[33] Cynthia A Chestek, Vikash Gilja, Christine H Blabe, Brett L Foster, Krishna V Shenoy, Josef Parvizi, and Jaimie M Henderson. Hand posture classification using electrocorticography signals in the gamma band over human sensorimotor brain areas. *Journal of neural engineering*, 10(2):026002, 2013.

[34] Jae-Hyun Cho, Seung Bong Hong, Young-Jin Jung, Hoon-Chul Kang, Heung Dong Kim, Minah Suh, Ki-Young Jung, and Chang-Hwan Im. Evaluation of algorithms for intracranial EEG (iEEG) source imaging of extended sources: feasibility of using iEEG source imaging for localizing epileptogenic zones in secondary generalized epilepsy. *Brain topography*, 24(2):91–104, 2011.

[35] CIBC, 2016. Seg3D: Volumetric Image Segmentation and Visualization. Scientific Computing and Imaging Institute (SCI), Download from: http://www.seg3d.org.

[36] Guillem Collell and Jordi Fauquet. Brain activity and cognition: a connection from thermodynamics and information theory. *Frontiers in psychology*, 6:818, 2015.

[37] Nathan E Crone, Diana L Miglioretti, Barry Gordon, and Ronald P Lesser. Functional mapping of human sensorimotor cortex with electrocorticographic spectral analysis. II. Event-related synchronization in the gamma band. *Brain*, 121(12):2301–2315, 1998.

[38] Janis J Daly and Jonathan R Wolpaw. Brain–computer interfaces in neurological rehabilitation. *The Lancet Neurology*, 7(11):1032–1043, 2008.

[39] JC De Munck, Maria J Peters, et al. A fast method to compute the potential in the multisphere model. *IEEE Trans. Biomed. Eng*, 40(11):1166–1174, 1993.

[40] Shaul Druckmann, Yoav Banitt, Albert A Gidon, Felix Schürmann, Henry Markram, and Idan Segev. A novel multiple objective op-

timization framework for constraining conductance-based neuron models by experimental data. *Frontiers in neuroscience*, 1:1, 2007.

[41] Jiangang Du, Timothy J Blanche, Reid R Harrison, Henry A Lester, and Sotiris C Masmanidis. Multiplexed, high density electrophysiology with nanofabricated neural probes. *PLoS One*, 6(10):e26204, 2011.

[42] Agrita Dubey and Supratim Ray. Cortical Electrocorticogram (ECoG) is a local signal. *Journal of Neuroscience*, 39(22):4299–4311, 2019.

[43] JC Eccles. Interpretation of action potentials evoked in the cerebral cortex. *Electroencephalography and clinical neurophysiology*, 3(4):449–464, 1951.

[44] Gaute T Einevoll, Christoph Kayser, Nikos K Logothetis, and Stefano Panzeri. Modelling and analysis of local field potentials for studying the function of cortical circuits. *Nature Reviews Neuroscience*, 14(11):770–785, 2013.

[45] Christian Engwer, Johannes Vorwerk, Jakob Ludewig, and Carsten H Wolters. A discontinuous Galerkin method to solve the EEG forward problem using the subtraction approach. *SIAM Journal on Scientific Computing*, 39(1):B138–B164, 2017.

[46] Jochen M Eppler, Moritz Helias, Eilif Muller, Markus Diesmann, and Marc-Oliver Gewaltig. PyNEST: a convenient interface to the NEST simulator. *Frontiers in neuroinformatics*, 2:12, 2009.

[47] Noelle Marie D Espiritu, Senrong Ainsley C Chen, Tiffany Ann C Blasa, Francisco Emmanuel T Munsayac, Rebecca P Arenos, Renann G Baldovino, Nilo T Bugtai, and Homer S Co. Bci-controlled smart wheelchair for amyotrophic lateral sclerosis patients. In *2019 7th International Conference on Robot Intelligence Technology and Applications (RiTA)*, pages 258–263. IEEE, 2019.

[48] Qianqian Fang and David A Boas. Tetrahedral mesh generation from volumetric binary and grayscale images. In *2009 IEEE International Symposium on Biomedical Imaging: From Nano to Macro*, pages 1142–1145. Ieee, 2009.

[49] Wendy Franks, Iwan Schenker, Patrik Schmutz, and Andreas Hierlemann. Impedance characterization and modeling of electrodes for biomedical applications. *IEEE Transactions on Biomedical Engineering*, 52(7):1295–1302, 2005.

[50] Walter J Freeman, Linda J Rogers, Mark D Holmes, and Daniel L Silbergeld. Spatial spectral analysis of human electrocorticograms including the alpha and gamma bands. *Journal of neuroscience methods*, 95(2):111–121, 2000.

[51] Karl J Friston. Functional and effective connectivity in neuroimaging: a synthesis. *Human brain mapping*, 2(1-2):56–78, 1994.

[52] Eberhard Fuchs and Gabriele Flügge. Adult neuroplasticity: more than 40 years of research. *Neural plasticity*, 2014, 2014.

[53] Manfred Fuchs, Michael Wagner, and Joern Kastner. Development of volume conductor and source models to localize epileptic foci. *Journal of Clinical Neurophysiology*, 24(2):101–119, 2007.

[54] C Gabriel, A Peyman, and EH Grant. Electrical conductivity of tissue at frequencies below 1 MHz. *Physics in medicine and biology*, 54(16):4863, 2009.

[55] Sami Gabriel, RW Lau, and Camelia Gabriel. The dielectric properties of biological tissues: III. Parametric models for the dielectric spectrum of tissues. *Physics in medicine and biology*, 41(11):2271, 1996.

[56] Charles R Gerfen, Michael N Economo, and Jayaram Chandrashekar. Long distance projections of cortical pyramidal neurons. *Journal of neuroscience research*, 96(9):1467–1475, 2018.

[57] C Geuzaine and JF Remacle. GMSH: A three-dimensional finite element mesh generator with built-in pre-and post-processing facilities, Version 2.2. 4, 2008.

[58] J Willard Gibbs. Fourier's series. *Nature*, 59(1522):200, 1898.

[59] Daniel M Goldenholz, Seppo P Ahlfors, Matti S Hämäläinen, Dahlia Sharon, Mamiko Ishitobi, Lucia M Vaina, and Steven M Stufflebeam. Mapping the signal-to-noise-ratios of cortical sources in magnetoencephalography and electroencephalography. *Human brain mapping*, 30(4):1077–1086, 2009.

[60] Jean-Marie Gomes, Claude Bédard, Silvana Valtcheva, Matthew Nelson, Vitalia Khokhlova, Pierre Pouget, Laurent Venance, Thierry Bal, and Alain Destexhe. Intracellular impedance measurements reveal non-ohmic properties of the extracellular medium around neurons. *Biophysical journal*, 110(1):234–246, 2016.

[61] E Gongadze, S Petersen, U Beck, and U Van Rienen. Classical Models of the Interface between an Electrode and an Electrolyte. In *COMSOL conference*, pages 14–16, 2009.

[62] Dan FM Goodman and Romain Brette. Brian: a simulator for spiking neural networks in python. *Frontiers in neuroinformatics*, 2:5, 2008.

[63] Takakuni Goto, Rieko Hatanaka, Takeshi Ogawa, Akira Sumiyoshi, Jorge Riera, and Ryuta Kawashima. An evaluation of the conductivity profile in the somatosensory barrel cortex of Wistar rats. *Journal of neurophysiology*, 104(6):3388–3412, 2010.

[64] Nathan W Gouwens, Jim Berg, David Feng, Staci A Sorensen, Hongkui Zeng, Michael J Hawrylycz, Christof Koch, and Anton Arkhipov. Systematic generation of biophysically detailed models for diverse cortical neuron types. *Nature communications*, 9(1):1–13, 2018.

[65] Peadar F Grant and Madeleine M Lowery. Effect of dispersive conductivity and permittivity in volume conductor models of deep brain stimulation. *IEEE Transactions on Biomedical Engineering*, 57(10):2386–2393, 2010.

[66] Sergey L Gratiy, Geir Halnes, Daniel Denman, Michael J Hawrylycz, Christof Koch, Gaute T Einevoll, and Costas A Anastassiou. From Maxwell's equations to the theory of current-source density analysis. *European Journal of Neuroscience*, 45(8):1013–1023, 2017.

[67] C. Guger, H. Ramoser, and G. Pfurtscheller. Real-time EEG analysis with subject-specific spatial patterns for a brain-computer interface (BCI). *IEEE Transactions on Rehabilitation Engineering*, 8(4):447–456, 2000.

[68] Daniel Güllmar, Jens Haueisen, and Jürgen R Reichenbach. Influence of anisotropic electrical conductivity in white matter tissue on the EEG/MEG forward and inverse solution. A high-resolution whole head simulation study. *Neuroimage*, 51(1):145–163, 2010.

[69] Ramesh M Gulrajani. *Bioelectricity and biomagnetism*. J. Wiley, 1998.

[70] Espen Hagen, Solveig Næss, Torbjørn V Ness, and Gaute T Einevoll. Multimodal modeling of neural network activity: computing LFP, ECoG, EEG, and MEG signals with LFPy 2.0. *Frontiers in neuroinformatics*, 12:92, 2018.

[71] Hans Hallez, Bart Vanrumste, Roberta Grech, Joseph Muscat, Wim De Clercq, Anneleen Vergult, Yves D'Asseler, Kenneth P Camilleri, Simon G Fabri, Sabine Van Huffel, et al. Review on solving the forward problem in EEG source analysis. *Journal of neuroengineering and rehabilitation*, 4(1):1–29, 2007.

[72] Matti S Hämäläinen. Magnetoencephalography: a tool for functional brain imaging. *Brain topography*, 5(2):95–102, 1992.

[73] Jiawei Han, Hongjie Jiang, and Junming Zhu. Neurorestoration: Advances in human brain-computer interface using microelectrode arrays. *Journal of Neurorestoratology*, 8(1):32–39, 2020.

[74] Peter Hansbo. Beyond the elements of finite elements: General principles for solid and fluid mechanics applications. *Lecture Notes, Chalmers University of Technology, Sweden*, 2006.

[75] Peter Hansbo, Carlo Lovadina, Ilaria Perugia, and Giancarlo Sangalli. A Lagrange multiplier method for the finite element solution of elliptic interface problems using non-matching meshes. *Numerische Mathematik*, 100(1):91–115, 2005.

[76] Kenneth D Harris, Rodrigo Quian Quiroga, Jeremy Freeman, and Spencer L Smith. Improving data quality in neuronal population recordings. *Nature neuroscience*, 19(9):1165–1174, 2016.

[77] Reid R Harrison and Cameron Charles. A low-power low-noise CMOS amplifier for neural recording applications. *IEEE Journal of solid-state circuits*, 38(6):958–965, 2003.

[78] Matthias Heim, Lionel Rousseau, Stéphane Reculusa, Veronika Urbanova, Claire Mazzocco, Sébastien Joucla, Laurent Bouffier, Karel Vytras, Philip Bartlett, Alexander Kuhn, et al. Combined macro-/mesoporous microelectrode arrays for low-noise extracellular recording of neural networks. *Journal of neurophysiology*, 108(6):1793–1803, 2012.

[79] H von Helmholtz. Ueber einige Gesetze der Verteilung elektrischer Ströme in körperlichen Leitern, mit Anwendung auf die thierisch-elektrischen Versuche (Schluss.). *Annalen der Physik*, 165(7):353–377, 1853.

[80] H Von Helmholtz. Studien über electrische Grenzschichten. *Annalen der Physik*, 243(7):337–382, 1879.

[81] Rikkert Hindriks, Cristiano Micheli, Conrado A Bosman, Robert Oostenveld, C Lewis, Dante Mantini, Pascal Fries, and Gustavo

Deco. Source-reconstruction of the sensorimotor network from resting-state macaque electrocorticography. *NeuroImage*, 181:347–358, 2018.

[82] Michael L Hines and Nicholas T Carnevale. The NEURON simulation environment. *Neural computation*, 9(6):1179–1209, 1997.

[83] Mojgan Hodaie, Richard A Wennberg, Jonathan O Dostrovsky, and Andres M Lozano. Chronic anterior thalamus stimulation for intractable epilepsy. *Epilepsia*, 43(6):603–608, 2002.

[84] Guosong Hong and Charles M Lieber. Novel electrode technologies for neural recordings. *Nature Reviews Neuroscience*, 20(6):330–345, 2019.

[85] Kenneth W Horch and Gurpreet S Dhillon. *Neuroprosthetics: theory and practice*. World Scientific, 2004.

[86] B Howell and WM Grill. Design of electrodes for stimulation and recording. In *Implantable neuroprostheses for restoring function*, pages 59–93. Woodhead Publishing Series in Biomaterials, 2015.

[87] Ben Yu-Kuang Hu. Solving boundary-value electrostatics problems using Greens reciprocity theorem. *American Journal of Physics*, 69(12):1280–1282, 2001.

[88] Yu Huang, Abhishek Datta, Marom Bikson, and Lucas C Parra. Realistic volumetric-approach to simulate transcranial electric stimulationROASTa fully automated open-source pipeline. *Journal of neural engineering*, 16(5):056006, 2019.

[89] Laurentius Huber, Emily S Finn, Daniel A Handwerker, Marlene Bönstrup, Daniel R Glen, Sriranga Kashyap, Dimo Ivanov, Natalia Petridou, Sean Marrett, Jozien Goense, et al. Sub-millimeter fMRI reveals multiple topographical digit representations that form action maps in human motor cortex. *Neuroimage*, 208:116463, 2020.

[90] Michael P Hughes, Karla Bustamante, Danny J Banks, and David J Ewins. Effects of electrode size on the performance of neural recording microelectrodes. In *1st Annual International IEEE-EMBS Special Topic Conference on Microtechnologies in Medicine and Biology. Proceedings (Cat. No. 00EX451)*, pages 220–223. IEEE, 2000.

[91] J David Irwin and Robert M Nelms. *Basic engineering circuit analysis*, volume 900. John Wiley & Sons, 2010.

[92] John David Jackson. *Classical electrodynamics*. John Wiley & Sons, 2007.

[93] Mark Jenkinson, Christian F Beckmann, Timothy EJ Behrens, Mark W Woolrich, and Stephen M Smith. Fsl. *Neuroimage*, 62(2):782–790, 2012.

[94] John Bertrand Johnson. Thermal agitation of electricity in conductors. *Physical review*, 32(1):97, 1928.

[95] Renaud Jolivet, Arnd Roth, Felix Schürmann, Wulfram Gerstner, and Walter Senn. Special issue on quantitative neuron modeling. *Biological cybernetics*, 99(ARTICLE):237–239, 2008.

[96] Mehdi Jorfi, John L Skousen, Christoph Weder, and Jeffrey R Capadona. Progress towards biocompatible intracortical microelectrodes for neural interfacing applications. *Journal of neural engineering*, 12(1):011001, 2014.

[97] Sébastien Joucla and Blaise Yvert. Improved focalization of electrical microstimulation using microelectrode arrays: a modeling study. *PloS one*, 4(3):e4828, 2009.

[98] Y. Kajikawa and C.E. Schroeder. How local is the local field potential? *Neuron*, 72(5):847–858, 2011.

[99] Eric R Kandel, James H Schwartz, Thomas M Jessell, Department of Biochemistry, Molecular Biophysics Thomas Jessell, Steven Siegelbaum, and AJ Hudspeth. *Principles of neural science*, volume 4. McGraw-hill New York, 2000.

[100] Emily S Kappenman and Steven J Luck. The effects of electrode impedance on data quality and statistical significance in ERP recordings. *Psychophysiology*, 47(5):888–904, 2010.

[101] S. Katzner, I. Nauhaus, A. Benucci, V. Bonin, D.L. Ringach, and M. Carandini. Local origin of field potentials in visual cortex. *Neuron*, 61(1):35–41, 2009.

[102] Raeyoung Kim, Sunghoon Joo, Hyunjun Jung, Nari Hong, and Yoonkey Nam. Recent trends in microelectrode array technology for in vitro neural interface platform. *Biomedical Engineering Letters*, 4(2):129–141, 2014.

[103] Daryl R Kipke, Rio J Vetter, Justin C Williams, and Jamille F Hetke. Silicon-substrate intracortical microelectrode arrays for long-term recording of neuronal spike activity in cerebral cortex. *IEEE transactions on neural systems and rehabilitation engineering*, 11(2):151–155, 2003.

[104] Christof Koch and Idan Segev. The role of single neurons in information processing. *nature neuroscience*, 3:1171–1177, 2000.

[105] Dimitrios A Koutsouras, Leona V Lingstedt, Katharina Lieberth, Jonas Reinholz, Volker Mailänder, Paul WM Blom, and Paschalis Gkoupidenis. Probing the Impedance of a Biological Tissue with PEDOT: PSS-Coated Metal Electrodes: Effect of Electrode Size on Sensing Efficiency. *Advanced healthcare materials*, 8(23):1901215, 2019.

[106] Hans Petter Langtangen and Kent-Andre Mardal. Introduction to Numerical Methods for Variational Problems, 2016.

[107] Mats G Larson and Fredrik Bengzon. *The finite element method: theory, implementation, and applications*, volume 10. Springer Science & Business Media, 2013.

[108] Juha Latikka, Timo Kuurne, and Hannu Eskola. Conductivity of living intracranial tissues. *Physics in medicine and biology*, 46(6):1611, 2001.

[109] Seung-Bo Lee, Hyun-Ji Kim, Hakseung Kim, Ji-Hoon Jeong, Seong-Whan Lee, and Dong-Joo Kim. Comparative analysis of features extracted from EEG spatial, spectral and temporal domains for binary and multiclass motor imagery classification. *Information Sciences*, 502:190–200, 2019.

[110] Scott F Lempka, Matthew D Johnson, Michael A Moffitt, Kevin J Otto, Daryl R Kipke, and Cameron C McIntyre. Theoretical analysis of intracortical microelectrode recordings. *Journal of neural engineering*, 8(4):045006, 2011.

[111] Scott F Lempka, Svjetlana Miocinovic, Matthew D Johnson, Jerrold L Vitek, and Cameron C McIntyre. In vivo impedance spectroscopy of deep brain stimulation electrodes. *Journal of neural engineering*, 6(4):046001, 2009.

[112] P Sanz Leon, SA Knock, MM Woodman, L Domide, J Mersmann, AR McIntosh, and V Jirsa. The Virtual Brain: a simulator of primate brain network dynamics. Front. *Neuroinformatics*, 7, 2013.

[113] Szymon Leski, Henrik Lindén, Tom Tetzlaff, Klas H Pettersen, and Gaute T Einevoll. Frequency dependence of signal power and spatial reach of the local field potential. *PLoS computational biology*, 9(7):e1003137, 2013.

[114] Eric C Leuthardt, Gerwin Schalk, Jonathan R Wolpaw, Jeffrey G Ojemann, and Daniel W Moran. A brain–computer interface using electrocorticographic signals in humans. *Journal of neural engineering*, 1(2):63, 2004.

[115] Henrik Lindén, Tom Tetzlaff, Tobias C Potjans, Klas H Pettersen, Sonja Grün, Markus Diesmann, and Gaute T Einevoll. Modeling the spatial reach of the LFP. *Neuron*, 72(5):859–872, 2011.

[116] Anders Logg, Kent-Andre Mardal, and Garth Wells. *Automated solution of differential equations by the finite element method: The FEniCS book*, volume 84. Springer Science & Business Media, 2012.

[117] Anders Logg and Garth N Wells. DOLFIN: Automated finite element computing. *ACM Transactions on Mathematical Software (TOMS)*, 37(2):20, 2010.

[118] N.K. Logothetis, C. Kayser, and A. Oeltermann. In vivo measurement of cortical impedance spectrum in monkeys: implications for signal propagation. *Neuron*, 55(5):809–823, 2007.

[119] N.K. Logothetis, J. Pauls, M. Augath, T. Trinath, A. Oeltermann, et al. Neurophysiological investigation of the basis of the fMRI signal. *Nature*, 412(6843):150–157, 2001.

[120] Miguel Angel Lopez-Gordo, Daniel Sanchez-Morillo, and F Pelayo Valle. Dry EEG electrodes. *Sensors*, 14(7):12847–12870, 2014.

[121] Digby D Macdonald and Mirna Urquidi-Macdonald. Kramers-Kronig Transformation of Constant Phase Impedances. *Journal of The Electrochemical Society*, 137(2):515–517, 1990.

[122] Joseph A Maldjian, Allan Gottschalk, Rita S Patel, John A Detre, and David C Alsop. The sensory somatotopic map of the human hand demonstrated at 4 Tesla. *Neuroimage*, 10(1):55–62, 1999.

[123] Jaakko Malmivuo and Robert Plonsey. *Bioelectromagnetism: principles and applications of bioelectric and biomagnetic fields*. Oxford University Press, USA, 1995.

[124] Gildas Marin, Christophe Guerin, Sylvain Baillet, Line Garnero, and Gérard Meunier. Influence of skull anisotropy for the forward and inverse problem in EEG: simulation studies using FEM on realistic head models. *Human brain mapping*, 6(4):250–269, 1998.

[125] Edwin M Maynard, Craig T Nordhausen, and Richard A Normann. The Utah intracortical electrode array: a recording structure for po-

tential brain-computer interfaces. *Electroencephalography and clinical neurophysiology*, 102(3):228–239, 1997.

[126] Hannah McCann, Giampaolo Pisano, and Leandro Beltrachini. Variation in reported human head tissue electrical conductivity values. *Brain topography*, 32(5):825–858, 2019.

[127] Daniel R Merrill, Marom Bikson, and John GR Jefferys. Electrical stimulation of excitable tissue: design of efficacious and safe protocols. *Journal of neuroscience methods*, 141(2):171–198, 2005.

[128] Stéphanie Miceli, Torbjørn V Ness, Gaute T Einevoll, and Dirk Schubert. Impedance spectrum in cortical tissue: Implications for propagation of LFP signals on the microscopic level. *eNeuro*, 4(1), 2017.

[129] Ezequiel Mikulan, Simone Russo, Sara Parmigiani, Simone Sarasso, Flavia Maria Zauli, Annalisa Rubino, Pietro Avanzini, Anna Cattani, Alberto Sorrentino, Steve Gibbs, et al. Simultaneous human intracerebral stimulation and HD-EEG, ground-truth for source localization methods. *Scientific data*, 7(1):1–8, 2020.

[130] U. Mitzdorf. Current source-density method and application in cat cerebral cortex: investigation of evoked potentials and EEG phenomena. *Physiological reviews*, 65(1):37–100, 1985.

[131] Céline Moulin, Alain Glière, Daniel Barbier, Sebastien Joucla, Blaise Yvert, Pascal Mailley, and Régis Guillemaud. A new 3-D finite-element model based on thin-film approximation for microelectrode array recording of extracellular action potential. *IEEE Transactions on Biomedical Engineering*, 55(2):683–692, 2008.

[132] Solveig Naess, Chaitanya Chintaluri, Torbjorn Baeko Ness, Anders M Dale, Gaute Tomas Einevoll, and Daniel K Wojcik. Four-Sphere Head Model For EEG Signals Revisited. *bioRxiv*, page 124875, 2017.

[133] Solveig Næss, Geir Halnes, Espen Hagen, Donald J Hagler Jr, Anders M Dale, Gaute T Einevoll, and Torbjørn V Ness. Biophysically detailed forward modeling of the neural origin of EEG and MEG signals. *NeuroImage*, 225:117467, 2021.

[134] Matthew J Nelson and Pierre Pouget. Do electrode properties create a problem in interpreting local field potential recordings?, 2010.

[135] Matthew J Nelson, Pierre Pouget, Erik A Nilsen, Craig D Patten, and Jeffrey D Schall. Review of signal distortion through metal

microelectrode recording circuits and filters. *Journal of neuroscience methods*, 169(1):141–157, 2008.

[136] Torbjørn V Ness, Chaitanya Chintaluri, Jan Potworowski, Szymon Łeski, Helena Głkabska, Daniel K Wójcik, and Gaute T Einevoll. Modelling and analysis of electrical potentials recorded in microelectrode arrays (MEAs). *Neuroinformatics*, 13(4):403–426, 2015.

[137] Michael R Neuman. Biopotential amplifiers. *Medical instrumentation: application and design*, pages 292–296, 1998.

[138] Samuel A Neymotin, Dylan S Daniels, Blake Caldwell, Robert A McDougal, Nicholas T Carnevale, Mainak Jas, Christopher I Moore, Michael L Hines, Matti Hämäläinen, and Stephanie R Jones. Human Neocortical Neurosolver (HNN): A new software tool for interpreting the cellular and network origin of human MEG/EEG data. *bioRxiv*, page 740597, 2019.

[139] Ernst Niedermeyer and FH Lopes da Silva. *Electroencephalography: basic principles, clinical applications, and related fields*. Lippincott Williams & Wilkins, 2005.

[140] Jesper D Nielsen, Kristoffer H Madsen, Oula Puonti, Hartwig R Siebner, Christian Bauer, Camilla Gøbel Madsen, Guilherme B Saturnino, and Axel Thielscher. Automatic skull segmentation from MR images for realistic volume conductor models of the head: Assessment of the state-of-the-art. *Neuroimage*, 174:587–598, 2018.

[141] Paul L Nunez. *Electric fields of the brain: the neurophysics of EEG*. Oxford University Press, 2006.

[142] Andreas Nüßing, Maria Carla Piastra, Sophie Schrader, Tuuli Miinalainen, Heinrich Brinck, Carsten H Wolters, and Christian Engwer. duneuro-A software toolbox for forward modeling in neuroscience. *arXiv preprint arXiv:1901.02874*, 2019.

[143] Jorma O Ollikainen, Marko Vauhkonen, Pasi A Karjalainen, and Jari P Kaipio. Effects of electrode properties on EEG measurements and a related inverse problem. *Medical engineering & physics*, 22(8):535–545, 2000.

[144] Robert Oostenveld, Pascal Fries, Eric Maris, and Jan-Mathijs Schoffelen. FieldTrip: open source software for advanced analysis of MEG, EEG, and invasive electrophysiological data. *Computational intelligence and neuroscience*, 2011:1, 2011.

[145] Alexander Opitz, Mirko Windhoff, Robin M Heidemann, Robert Turner, and Axel Thielscher. How the brain tissue shapes the electric field induced by transcranial magnetic stimulation. *Neuroimage*, 58(3):849–859, 2011.

[146] A. Pascarella, C. Todaro, M. Clerc, T. Serre, and M. Piana. Source modeling of ElectroCorticoGraphy (ECoG) data: Stability analysis and spatial filtering. *Journal of Neuroscience Methods*, 263:134 – 144, 2016.

[147] Kunal S Patel, Brandon Goldenberg, and Theodore H Schwartz. Betadine irrigation and post-craniotomy wound infection. *Clinical neurology and neurosurgery*, 118:49–52, 2014.

[148] Elmar GM Pels, Erik J Aarnoutse, Sacha Leinders, Zac V Freudenburg, Mariana P Branco, Benny H van der Vijgh, Tom J Snijders, Timothy Denison, Mariska J Vansteensel, and Nick F Ramsey. Stability of a chronic implanted brain-computer interface in late-stage amyotrophic lateral sclerosis. *Clinical Neurophysiology*, 130(10):1798–1803, 2019.

[149] Wilder Penfield and Edwin Boldrey. Somatic motor and sensory representation in the cerebral cortex of man as studied by electrical stimulation. *Brain*, 60(4):389–443, 1937.

[150] Klas H Pettersen, Espen Hagen, and Gaute T Einevoll. Estimation of population firing rates and current source densities from laminar electrode recordings. *Journal of computational neuroscience*, 24(3):291–313, 2008.

[151] Maria Carla Piastra, Andreas Nüßing, Johannes Vorwerk, Harald Bornfleth, Robert Oostenveld, Christian Engwer, and Carsten H Wolters. The discontinuous galerkin finite element method for solving the MEG and the combined MEG/EEG forward problem. *Frontiers in neuroscience*, 12:30, 2018.

[152] Robert Plonsey. Reciprocity applied to volume conductors and the ECG. *IEEE Transactions on Bio-medical Electronics*, 10(1):9–12, 1963.

[153] Robert Plonsey and Dennis B Heppner. Considerations of quasi-stationarity in electrophysiological systems. *Bulletin of mathematical Biology*, 29(4):657–664, 1967.

[154] Clive Poole and Izzat Darwazeh. *Microwave active circuit analysis and design*. Academic Press, 2015.

[155] Kelsey A Potter, Joel S Simon, Bharath Velagapudi, and Jeffrey R Capadona. Reduction of autofluorescence at the microelectrode–cortical tissue interface improves antibody detection. *Journal of neuroscience methods*, 203(1):96–105, 2012.

[156] VV Pravdich-Neminsky. Ein Versuch der Registrierung der elektrischen Gehirnerscheinungen. *Zbl Physiol*, 27:951–960, 1913.

[157] S Pursiainen, F Lucka, and CH Wolters. Complete electrode model in EEG: relationship and differences to the point electrode model. *Physics in Medicine & Biology*, 57(4):999, 2012.

[158] Sampsa Pursiainen, Seok Lew, and Carsten Hermann Wolters. Forward and inverse effects of the complete electrode model in neonatal EEG. *Journal of neurophysiology*, 117(3):876–884, 2017.

[159] Qinwan Rabbani, Griffin Milsap, and Nathan E Crone. The potential for a speech brain–computer interface using chronic electrocorticography. *Neurotherapeutics*, 16(1):144–165, 2019.

[160] Valerica Raicu, Nobuko Kitagawa, and Akihiko Irimajiri. A quantitative approach to the dielectric properties of the skin. *Physics in medicine and biology*, 45(2):L1, 2000.

[161] NF Ramsey, EJ Aarnoutse, and MJ Vansteensel. Brain Implants for Substituting Lost Motor Function: State of the Art and Potential Impact on the Lives of Motor-Impaired Seniors. *Gerontology*, 60(4):366–372, 2014.

[162] GN Reddy and Subrata Saha. Electrical and dielectric properties of wet bone as a function of frequency. *IEEE transactions on biomedical engineering*, (3):296–303, 1984.

[163] Aya Rezeika, Mihaly Benda, Piotr Stawicki, Felix Gembler, Abdul Saboor, and Ivan Volosyak. Brain–computer interface spellers: A review. *Brain sciences*, 8(4):57, 2018.

[164] A Richardot and ET McAdams. Harmonic analysis of low-frequency bioelectrode behavior. *IEEE transactions on medical imaging*, 21(6):604–612, 2002.

[165] David A Robinson. The electrical properties of metal microelectrodes. *Proceedings of the IEEE*, 56(6):1065–1071, 1968.

[166] Cyrille Rossant, Shabnam N Kadir, Dan FM Goodman, John Schulman, Maximilian LD Hunter, Aman B Saleem, Andres Grosmark, Mariano Belluscio, George H Denfield, Alexander S Ecker, et al.

Spike sorting for large, dense electrode arrays. *Nature neuroscience*, 19(4):634–641, 2016.

[167] Stanley Rush and Daniel A Driscoll. EEG electrode sensitivity-an application of reciprocity. *IEEE transactions on biomedical engineering*, (1):15–22, 1969.

[168] Seward B Rutkove. Introduction to volume conduction. In *The clinical neurophysiology primer*, pages 43–53. Springer, 2007.

[169] Isabel Delgado Ruz and Simon R Schultz. Localising and classifying neurons from high density MEA recordings. *Journal of neuroscience methods*, 233:115–128, 2014.

[170] Rosa M Sanchez Panchuelo, Julien Besle, Denis Schluppeck, Miles Humberstone, and Susan Francis. Somatotopy in the human somatosensory system. *Frontiers in human neuroscience*, 12:235, 2018.

[171] Jukka Sarvas. Basic mathematical and electromagnetic concepts of the biomagnetic inverse problem. *Physics in Medicine & Biology*, 32(1):11, 1987.

[172] David Satzer, David Lanctin, Lynn E Eberly, and Aviva Abosch. Variation in deep brain stimulation electrode impedance over years following electrode implantation. *Stereotactic and functional neurosurgery*, 92(2):94–102, 2014.

[173] Wouter Schellekens, Natalia Petridou, and Nick F Ramsey. Detailed somatotopy in primary motor and somatosensory cortex revealed by Gaussian population receptive fields. *Neuroimage*, 179:337–347, 2018.

[174] Herman P Schwan and Clifford D Ferris. Four-electrode null techniques for impedance measurement with high resolution. *Review of scientific instruments*, 39(4):481–485, 1968.

[175] HP Schwan. Linear and nonlinear electrode polarization and biological materials. *Annals of biomedical engineering*, 20(3):269–288, 1992.

[176] Andrew B Schwartz, X Tracy Cui, Douglas J Weber, and Daniel W Moran. Brain-controlled interfaces: movement restoration with neural prosthetics. *Neuron*, 52(1):205–220, 2006.

[177] Jorge Sepulcre, Hesheng Liu, Tanveer Talukdar, Iñigo Martincorena, BT Thomas Yeo, and Randy L Buckner. The organization of local and distant functional connectivity in the human brain. *PLoS computational biology*, 6(6):e1000808, 2010.

[178] Maxwell A Sherman, Shane Lee, Robert Law, Saskia Haegens, Catherine A Thorn, Matti S Hämäläinen, Christopher I Moore, and Stephanie R Jones. Neural mechanisms of transient neocortical beta rhythms: Converging evidence from humans, computational modeling, monkeys, and mice. *Proceedings of the National Academy of Sciences*, 113(33):E4885–E4894, 2016.

[179] Hang Si. TetGen: A quality tetrahedral mesh generator and three-dimensional delaunay triangulator. *Weierstrass Institute for Applied Analysis and Stochastic, Berlin, Germany*, 2006.

[180] Jeroen CW Siero, Dora Hermes, Hans Hoogduin, Peter R Luijten, Nick F Ramsey, and Natalia Petridou. BOLD matches neuronal activity at the mm scale: A combined 7 T fMRI and ECoG study in human sensorimotor cortex. *Neuroimage*, 101:177–184, 2014.

[181] Marc W Slutzky, Luke R Jordan, Todd Krieg, Ming Chen, David J Mogul, and Lee E Miller. Optimal spacing of surface electrode arrays for brain–machine interface applications. *Journal of neural engineering*, 7(2):026004, 2010.

[182] Andre Snellings, David J Anderson, and J Wayne Aldridge. Use of multichannel recording electrodes and independent component analysis for target localization in deep brain structures. In *First International IEEE EMBS Conference on Neural Engineering, 2003. Conference Proceedings.*, pages 305–308. IEEE, 2003.

[183] R. Srinivasan, W.R. Winter, and P.L. Nunez. Source analysis of EEG oscillations using high-resolution EEG and MEG. *Progress in brain research*, 159:29–42, 2006.

[184] François Tadel, Sylvain Baillet, John C Mosher, Dimitrios Pantazis, and Richard M Leahy. Brainstorm: a user-friendly application for MEG/EEG analysis. *Computational intelligence and neuroscience*, 2011, 2011.

[185] Axel Thielscher, Andre Antunes, and Guilherme B Saturnino. Field modeling for transcranial magnetic stimulation: A useful tool to understand the physiological effects of TMS? In *Engineering in Medicine and Biology Society (EMBC), 2015 37th Annual International Conference of the IEEE*, pages 222–225. IEEE, 2015.

[186] Haruo Toda, Takafumi Suzuki, Hirohito Sawahata, Kei Majima, Yukiyasu Kamitani, and Isao Hasegawa. Simultaneous recording of ECoG and intracortical neuronal activity using a flexible multi-

channel electrode-mesh in visual cortex. *Neuroimage*, 54(1):203–212, 2011.

[187] Chiara Todaro, Laura Marzetti, Pedro A Valdés Sosa, Pedro A Valdés-Hernandez, and Vittorio Pizzella. Mapping brain activity with electrocorticography: resolution properties and robustness of inverse solutions. *Brain topography*, 32(4):583–598, 2019.

[188] Brian Tracey and Michael Williams. Computationally efficient bioelectric field modeling and effects of frequency-dependent tissue capacitance. *Journal of neural engineering*, 8(3):036017, 2011.

[189] Morgan E Urdaneta, Nicolas G Kunigk, Francisco Delgado, Shelley Fried, and Kevin J Otto. Layer-specific parameters of intracortical microstimulation of the somatosensory cortex. *Journal of Neural Engineering*, 2021.

[190] Roemer van der Meij, Michael Kahana, and Eric Maris. Phase–amplitude coupling in human electrocorticography is spatially distributed and phase diverse. *Journal of Neuroscience*, 32(1):111–123, 2012.

[191] MJC Van Gemert. A note on the ColeCole dielectric permittivity equation in connnection with causality. *Chemical Physics Letters*, 14(5):606–608, 1972.

[192] RL Van Meirhaeghe, EC Dutoit, Felix Cardon, and WP Gomes. On the application of the Kramers-Kronig relations to problems concerning the frequency dependence of electrode impedance. *Electrochimica Acta*, 21(1):39–43, 1976.

[193] Bart Vanrumste, Richard D Jones, and Philip J Bones. Detection of focal epileptiform activity in the EEG: an SVD and dipole model approach. In *Proceedings of the Second Joint 24th Annual Conference and the Annual Fall Meeting of the Biomedical Engineering Society][Engineering in Medicine and Biology*, volume 3, pages 2031–2032. IEEE, 2002.

[194] Mariska J Vansteensel, Elmar GM Pels, Martin G Bleichner, Mariana P Branco, Timothy Denison, Zachary V Freudenburg, Peter Gosselaar, Sacha Leinders, Thomas H Ottens, Max A Van Den Boom, et al. Fully implanted brain–computer interface in a locked-in patient with ALS. *New England Journal of Medicine*, 375(21):2060–2066, 2016.

[195] M Vermaas, MC Piastra, TF Oostendorp, NF Ramsey, and PHE Tiesinga. FEMfuns: A Volume Conduction Modeling Pipeline that Includes Resistive, Capacitive or Dispersive Tissue and Electrodes. *Neuroinformatics*, 2020.

[196] M Vermaas, MC Piastra, TF Oostendorp, NF Ramsey, and PHE Tiesinga. When to include ECoG electrode properties in volume conduction models. *Journal of Neural Engineering*, 17(5):056031, 2020.

[197] Vijay Viswam, Jelena Dragas, Amir Shadmani, Yihui Chen, Alexander Stettler, Jan Müller, and Andreas Hierlemann. 22.8 Multifunctional microelectrode array system featuring 59,760 electrodes, 2048 electrophysiology channels, impedance and neurotransmitter measurement units. In *2016 IEEE International Solid-State Circuits Conference (ISSCC)*, pages 394–396. IEEE, 2016.

[198] Vijay Viswam, Marie Engelene J Obien, Felix Franke, Urs Frey, and Andreas Hierlemann. Optimal electrode size for multi-scale extracellular-potential recording from neuronal assemblies. *Frontiers in neuroscience*, 13:385, 2019.

[199] Constantin Von Economo. *The cytoarchitectonics of the human cerebral cortex*. H. Milford Oxford University Press, 1929.

[200] Johannes Vorwerk, Robert Oostenveld, Maria Carla Piastra, Lilla Magyari, and Carsten H Wolters. The FieldTrip-SimBio pipeline for EEG forward solutions. *Biomedical engineering online*, 17(1):37, 2018.

[201] Tim Wagner, Uri Eden, Jarrett Rushmore, Christopher J Russo, Laura Dipietro, Felipe Fregni, Stephen Simon, Stephen Rotman, Naomi B Pitskel, Ciro Ramos-Estebanez, et al. Impact of brain tissue filtering on neurostimulation fields: a modeling study. *Neuroimage*, 85:1048–1057, 2014.

[202] Matthew P Ward, Pooja Rajdev, Casey Ellison, and Pedro P Irazoqui. Toward a comparison of microelectrodes for acute and chronic recordings. *Brain research*, 1282:183–200, 2009.

[203] Ahuva Weltman, James Yoo, and Ellis Meng. Flexible, penetrating brain probes enabled by advances in polymer microfabrication. *Micromachines*, 7(10):180, 2016.

[204] Mirko Windhoff, Alexander Opitz, and Axel Thielscher. Electric field calculations in brain stimulation based on finite elements: an

optimized processing pipeline for the generation and usage of accurate individual head models. *Human brain mapping*, 34(4):923–935, 2013.

[205] Jonathan R Wolpaw. Brain–computer interfaces. In *Handbook of Clinical Neurology*, volume 110, pages 67–74. Elsevier, 2013.

[206] Jonathan R Wolpaw, José del R Millán, and Nick F Ramsey. Brain-computer interfaces: Definitions and principles. In *Handbook of Clinical Neurology*, volume 168, pages 15–23. Elsevier, 2020.

[207] Carsten Wolters and Jan C de Munck. Volume conduction. *Scholarpedia*, 2(3):1738, 2007.

[208] YiZi Xiao, Edgar Peña, and Matthew D Johnson. Theoretical optimization of stimulation strategies for a directionally segmented deep brain stimulation electrode array. *IEEE Transactions on Biomedical Engineering*, 63(2):359–371, 2015.

[209] Günther Zeck, Florian Jetter, Lakshmi Channappa, Gabriel Bertotti, and Roland Thewes. Electrical imaging: investigating cellular function at high resolution. *Advanced Biosystems*, 1(11):1700107, 2017.

[210] Yingchun Zhang, Wim van Drongelen, Michael Kohrman, and Bin He. Three-dimensional brain current source reconstruction from intra-cranial ECoG recordings. *NeuroImage*, 42(2):683–695, 2008.

[211] Julius Zimmermann and Ursula van Rienen. Ambiguity in the interpretation of the low-frequency dielectric properties of biological tissues. *Bioelectrochemistry*, 140:107773, 2021.

6 Research Data Management

This thesis research has been carried out under the institute research data management policy of the Donders Instutute for Brain, Cognition and Behavior (as of 25.2.2020, https://www.ru.nl/publish/library/397/rdmpolicy_di_20190110.pdf).

This research followed the applicable laws and ethical guidelines. Research Data Management was performed according to the FAIR principles. The information below details how this was achieved.

Ethical Approval

The thesis is based on simulation results and realistic data was taken from open-source libraries and previously collected anatomical patient data at University Medical Center Utrecht. The latter data-set contained personal data as defined in the General Data Protection Regulation (EU) 2016/679. The ECoG data collected at the University Medical Center Utrecht were acquired following signing informed consent in accordance with the Dutch Medical Research Act and the Declaration of Helsinki (2016). The individual subjects were not identifiable in the data shared with publications. Further, subjects were informed about and gave written consent for the future use of their anonymized data for publication and sharing with other researchers and the public prior to starting the data collection.

Findability and Accessibility

The table below details where the data and research documentation for each chapter can be found on the Donders Repository (DR) and/or Github. All data archived as a Data Sharing Collection remain available for at least 10 years after termination of the studies.

Chapter	Data Sharing Collection
2, 3, 4	https://doi.org/10.34973/yfh0-6c23 / https://github.com/meronvermaas/FEMfuns

Interoperability & Reusability

All data collections have been structured in a standardized way that is described in accompanying text files. The documentation includes specifications on:

a) Data pre-processing

b) Saved results
c) Accompanying codes for reproducing of the results
d) Source code for full pipeline
e) Conda environment to ensure correct version numbers for the software used

7 Publications

- Vermaas M, Piastra MC, Oostendorp TF, Ramsey NF, Tiesinga PHE. FEMfuns: A Volume Conduction Modeling Pipeline that Includes Resistive, Capacitive or Dispersive Tissue and Electrodes. Neuroinformatics. 2020 Oct;18(4):569-580. doi: 10.1007/s12021-020-09458-8.

- Vermaas M, Piastra MC, Oostendorp TF, Ramsey NF, Tiesinga PHE. When to include ECoG electrode properties in volume conduction models. J Neural Eng. 2020 Oct 15;17(5):056031. doi: 10.1088/1741-2552/abb11d.

Under revision M Vermaas, TF Oostendorp, R Oostenveld, NF Ramsey, PHE Tiesinga, and MC Piastra. Separability of finger somatotopic activity in sensorimotor cortex using high-density ECoG. Neuroimage